

Aus der Berlin Ultrahigh Field Facility (B.U.F.F.) am
Max-Delbrück Centrum (MDC) für Molekulare Medizin in der Helmholtz
Gemeinschaft, Berlin-Buch

DISSERTATION

Development of Fluorine-19 and Proton Magnetic Resonance
Imaging and its Application in Neuroinflammation

Entwicklung von Fluor-19 und Protonen-
Magnetresonanztomographie und ihre Anwendung bei
Neuroentzündung

zur Erlangung des akademischen Grades
Doctor of Philosophy (Ph.D.)

vorgelegt der Medizinischen Fakultät
Charité – Universitätsmedizin Berlin

von

Paula Ramos Delgado
aus Zamora, Spanien

Datum der Promotion: 25th June 2023

Table of contents

List of abbreviations	5
List of figures and tables	7
Synopsis.....	9
Zusammenfassung.....	11
1. Introduction.....	13
2. Methods.....	18
2.1. Magnetic resonance hardware	18
2.2. $^{19}\text{F}/^1\text{H}$ imaging setup	19
2.3. Test phantom, animal preparation and pre-clinical MR experiments.....	21
2.3.1. B_1 inhomogeneity correction in ^1H transceiver surface RF probes... 21	
2.3.2. B_1 inhomogeneity correction at low SNR using ^{19}F transceiver surface RF coils.....	22
2.3.3. Development of registration methods for longitudinal EAE studies..	24
2.4. ^{19}F -MRI data pre-processing.....	24
2.5. B_1 field characterization in transceive surface RF probes	25
2.5.1. Double angle method: theory and method extension.....	25
2.5.2. Sample preparation and experiments	26
2.6. Rapid Acquisition with Relaxation Enhancement (RARE).....	27
2.6.1. Basic principles	27
2.6.2. Empirical RARE signal intensity model	28
2.6.3. Simulated RARE signal intensity model.....	29
2.7. B_1 inhomogeneity correction techniques	29
2.7.1. Sensitivity B_1 correction method	29
2.7.2. Model-based B_1 correction method.....	30
2.7.3. Hybrid B_1 correction method	31
2.8. B_1 correction method validation and uncertainty calculation	32
2.8.1. Central profile plots	32
2.8.2. Image homogeneity assessment	32
2.8.3. T_1 contrast and quantification performance.....	32

2.8.4. Monte Carlo SNR simulations for uncertainty calculation	34
2.9. Development of registration methods for longitudinal EAE studies	37
3. Results	39
3.1. B ₁ inhomogeneity correction in ¹ H transceiver surface RF probes to enable signal quantification.....	39
3.1.1. B ₁ field characterization	39
3.1.2. Empirical RARE signal intensity model.....	40
3.1.3. B ₁ correction method validation	41
3.2. B ₁ inhomogeneity correction at low SNR: first quantitative <i>in vivo</i> ¹⁹ F-MRI of mouse brain inflammation using a transceiver surface RF probe.....	48
3.2.1. B ₁ field characterization and simulated RARE signal intensity model	49
3.2.2. T ₁ relaxation time estimation.....	50
3.2.3. Monte Carlo SNR simulations to estimate the ¹⁹ F concentration uncertainty	50
3.2.4. B ₁ correction method validation	52
3.2.5. Proportionality of hybrid and sensitivity methods for a “perfect” EPG-simulated RARE SI model	60
3.3. Development of registration methods for longitudinal EAE studies: validation and applications	62
3.3.1. Registration methods implementation and validation.....	63
3.3.2. GBCA-lesion burden quantification as a measure of inflammation in EAE using T ₁ mapping methods	64
4. Discussion	66
4.1. B ₁ inhomogeneity correction in ¹ H transceiver surface RF probes.....	66
4.1.1. Limitations and future directions	69
4.2. B ₁ inhomogeneity correction at low SNR using ¹⁹ F transceiver surface RF probes.....	70
4.2.1. Limitations and future directions	72
4.3. Development of registration methods for longitudinal EAE studies	74
4.3.1. Limitations and future directions	74
References	76
Statutory Declaration.....	88
Declaration of own contribution	90

Publication 1	90
Publication 2	91
Publication 3	92
Curriculum Vitae.....	151
List of publications.....	155
Peer-reviewed publications	155
Peer-reviewed conference abstracts and presentations	156
Acknowledgements	160

List of abbreviations

^1H	Proton / hydrogen
^{19}F	Fluorine-19
ANTs	A dvanced N ormalization T ools
ANTx	A tlas N ormalization T oolbox using E lastix
B_0	Static magnetic field
B_1	Radiofrequency field
B_1^+	Radiofrequency excitation field
B_1^-	Radiofrequency reception field
BBB	B lood- b rain b arrier
CNS	C entral n ervous s ystem
CRP	Transceive surface c ryogenically-cooled R F p robe
EAE	E xperimental a utoimmune e ncephalomyelitis
ESP	E cho s pacing
ETL	E cho t rain l ength
FA	F lip a ngle
FOV	F ield o f v iew
GBCA	G adolinium- b ased c ontrast a gent
ID	I nnner d iameter
MAPE	M ean a bsolute p ercentage e rror
MIJ	M ATLAB I mage J software module
MR	M agnetic r esonance
MRI	M agnetic r esonance i maging
MRS	M agnetic r esonance s pectroscopy
MS	M ultiple s clerosis
NA	N umber of a verages

NEX	Number of excitations
NP	Nanoparticle
PIU	Percentage integral uniformity
RARE	Rapid acquisition with relaxation enhancement
RAREVTR	RARE with variable TR
RF	Radiofrequency
ROI	Region of interest
RRMS	Relapsing-remitting multiple sclerosis
RT	Room-temperature
SI	Signal intensity
SNR	Signal-to-noise ratio
T	Tesla
T_1	Longitudinal (spin-lattice) relaxation time
T_{1w}	T_1 -weighted
T_2	Transversal (spin-spin) relaxation time
T_2^*	Effective transversal (spin-spin) relaxation time
TA	Total acquisition time
TE	Echo time
TE_{eff}	Effective echo time
tp_i	i-th timepoint
TR	Repetition time
UHF	Ultrahigh field

List of figures and tables

Figure 1. Anatomical and ^{19}F imaging setup designed for a single-tuned ^{19}F -CRP.....	20
Figure 2. RARE sequence diagram for an ETL=5 with centric Cartesian phase encoding.....	27
Figure 3. Workflows of (A) <i>sensitivity correction</i> and (B) <i>hybrid B_1 correction</i> .	30
Figure 4. Workflow of <i>model-based B_1 correction</i>	31
Figure 5. Illustrations of validation methods.....	33
Figure 6. Monte Carlo SNR simulation and uncertainty map estimation workflow	36
Figure 7. Multi-step 3D intra-subject registration workflow	38
Figure 8. Sensitivity maps and transmission fields of the two transceive (TxRx) surface RF coils used for testing and validation	40
Figure 9. Signal intensity models for RARE with and without flipback	41
Figure 10. B_1 correction for CRP images of a uniform phantom, an <i>ex vivo</i> phantom and a living mouse.....	42
Figure 11. Normalized signal intensity profiles perpendicular to the RF coil surface and percentage image uniformities (PIU)	43
Figure 12. Assessment of quantification and contrast accuracy for RARE without flipback.....	45
Figure 13. Assessment of quantification and contrast accuracy for RARE with active flipback.....	46
Figure 14. B_1 field maps of the quadrature ^{19}F cryogenically-cooled transceive surface RF probe (^{19}F -CRP) and SI model used.....	49

Figure 15. Exemplary spectra used for T_1 calculation	50
Figure 16. SNR simulation results corresponding to a <i>model-based</i> correction for $T_1=1869$ ms.....	51
Figure 17. Uniform phantom validation.....	53
Figure 18. <i>Ex vivo</i> phantom (score=2.0) in axial orientation	55
Figure 19. <i>Ex vivo</i> phantom (score=2.0) in sagittal orientation	56
Figure 20. <i>In vivo</i> EAE mouse 1 (score=2.5) in axial orientation	57
Figure 21. <i>In vivo</i> EAE mouse 1 (score=2.5) in sagittal orientation	58
Figure 22. <i>In vivo</i> EAE mouse 2 (score=1.5) in axial orientation	59
Figure 23. <i>In vivo</i> EAE mouse 2 (score=1.5) in sagittal orientation	60
Figure 24. Registration of post-contrast T_1W -images and maps	63
Figure 25. ROI validation	64
Figure 26. Gadolinium-enhancing lesions can be used as an objective quantitative measure of inflammation in EAE.....	65

Synopsis

The experimental autoimmune encephalomyelitis (EAE) is used to study multiple sclerosis (MS) pathology and develop novel technologies to quantify inflammation over time. Magnetic resonance imaging (MRI) with gadolinium-based contrast agents (GBCAs) is the state-of-the-art method to assess inflammation in MS patients and its animal model.

Fluorine (^{19}F)-MRI is one novel technology to quantify inflammatory immune cells *in vivo* using ^{19}F -nanoparticles. T_1 mapping of contrast-enhancing images is another method that could be implemented to quantify inflammatory lesions. Transient macroscopic changes in the EAE brain confound quantification and necessitate registration methods to spatially align images in longitudinal studies.

For ^{19}F -MRI, an additional challenge is the low signal-to-noise ratio (SNR) due to low number of ^{19}F -labeled immune cells *in vivo*. Transceive surface radiofrequency (RF) probes and SNR-efficient imaging techniques such as RARE (Rapid Acquisition with Relaxation Enhancement) are combined to increase sensitivity in ^{19}F -MRI. However, the strong spatially-varying RF field (B_1 inhomogeneity) of transceive surface RF probes further hampers quantification. Retrospective B_1 correction methods typically use signal intensity equations, unavailable for complex acquisition methods like RARE.

The main goal of this work is to investigate novel B_1 correction and registration methods to enable the study of inflammatory diseases using ^1H - and ^{19}F -MRI following GBCA and ^{19}F -nanoparticle administration, respectively. For correcting B_1 inhomogeneities in ^1H - and ^{19}F -MR transceive surface RF probes, a model-based method was developed using empirical measurements and simulations, and then validated and compared with a sensitivity method and a hybrid of both. For ^{19}F -MRI, a workflow to measure anatomical images *in vivo* and a method to compute ^{19}F -concentration uncertainty after correction using Monte Carlo simulations were developed. To overcome the challenges of EAE brain macroscopic changes, a pipeline for registering images throughout longitudinal studies was developed.

The proposed B_1 correction methods demonstrated dramatic improvements in signal quantification and T_1 contrast on images of test phantoms and mouse brains, allowing quantitative measurement with transceive surface RF probes. For low-SNR scenarios, the model-based method yielded reliable ^{19}F -quantifications when compared to volume resonators. Uncertainty after correction depended linearly on the SNR ($\leq 10\%$ with $\text{SNR} \geq 10.1$, $\leq 25\%$ when $\text{SNR} \geq 4.25$). The implemented registration approach provided successful image alignment despite substantial morphological changes in the EAE brain over time. Consequently, T_1 mapping was shown to objectively quantify gadolinium lesion burden as a measure of inflammatory activity in EAE.

The ^1H - and ^{19}F -MRI methods proposed here are highly relevant for quantitative MR of neuroinflammatory diseases, enabling future (pre)clinical investigations.

Zusammenfassung

Die experimentelle Autoimmun-Enzephalomyelitis (EAE) wird zur Untersuchung Multipler Sklerose (MS) und zur Entwicklung neuer Technologien zur Entzündungsquantifizierung eingesetzt. Magnetresonanztomographie (MRT) mit Gadolinium-haltigen Kontrastmitteln (GBCAs) ist die modernste Methode zur Beurteilung von Entzündungen bei MS-Patienten und im Tiermodell.

Fluor (^{19}F)-MRT unter Verwendung von ^{19}F -Nanopartikeln ist eine neue Technologie zur Quantifizierung entzündlicher Immunzellen *in vivo*. T_1 -Kartierung ist eine MRT-Methode, die zur Quantifizierung entzündlicher Läsionen eingesetzt werden könnte. Temporäremorphologische Veränderungen im EAE-Gehirn erschweren die Quantifizierung und erfordern Registrierungsmethoden, um MRT-Bilder in Längsschnittstudien räumlich abzugleichen.

Das niedrige Signal-Rausch-Verhältnis (SNR) ist aufgrund der geringen Anzahl ^{19}F -markierter Immunzellen *in vivo* eine zusätzliche Herausforderung der ^{19}F -MRT. Um deren Empfindlichkeit zu erhöhen, werden Sende-/Empfangsoberflächen-Hochfrequenzspulen (TX/RX-HF-Spule) und SNR-effiziente MRT-Techniken wie RARE (Rapid Acquisition with Relaxation Enhancement) kombiniert. Jedoch verhindert die starke räumliche Variation des HF-Feldes (B_1 -Inhomogenität) dieser Spulen die Signalquantifizierung. Retrospektive B_1 -Korrekturmethode verwenden in der Regel Signalintensitätsgleichungen, die für komplexe MRT-Techniken wie RARE nicht existieren.

Das Hauptziel dieser Arbeit ist die Untersuchung neuartiger B_1 -Korrektur- und Bildregistrierungsmethoden, um *in vivo* ^1H - und ^{19}F -MRT Studien von Entzündungsprozessen zu ermöglichen. Zur Korrektur von B_1 -Inhomogenitäten wurde eine modellbasierte Methode entwickelt. Diese verwendet empirische Messungen und Simulationen, wurde in Phantomexperimenten validiert und mit Referenzmethoden verglichen. Für ^{19}F -MRT wurden ein Protokoll zur Messung anatomischer Bilder *in vivo* und eine Methode zur Berechnung der ^{19}F -Konzentrationsunsicherheit nach Korrektur mittels Monte-Carlo-Simulationen

entwickelt. Um morphologische Veränderungen im EAE-Gehirn in longitudinalen Studien zu kompensieren, wurde zur Bildregistrierung eine Software-Bibliothek entwickelt.

Die B₁-Korrekturmethode zeigt in Testobjekten und Mäusehirnen drastische Verbesserungen der Signal- und T₁ Quantifizierung und ermöglicht so quantitative Messungen mit TX/RX-HF-Spulen. Die modellbasierte Methode liefert für geringe SNRs zuverlässige ¹⁹F-Quantifizierungen, deren Genauigkeit mit dem SNR korreliert. Die implementierte Registrierungsmethode ermöglichte einen erfolgreichen Abgleich von Bildserien trotz erheblicher morphologischer Veränderungen im EAE-Hirn. Folglich wurde gezeigt, dass MRT-basierte T₁-Kartierung die Gadolinium-Läsionslast als Maß entzündlicher Aktivität bei EAE objektiv quantifizieren kann.

Die hier untersuchten Methoden sind für quantitative ¹H- und ¹⁹F-MRT neuroinflammatorischer Erkrankungen sehr relevant und ermöglichen künftige (prä)klinische Untersuchungen.

1. Introduction

Magnetic resonance (MR) is a powerful and versatile non-invasive imaging modality that permits soft tissue contrast and is suitable for longitudinal studies due to the use of non-ionizing radiation. Anatomical MR images are based on the detection of signals coming from excited hydrogen (^1H) atoms within a static magnetic field B_0 . After a radiofrequency (RF) pulse is sent by the transmit RF coil, the magnetization vector is tilted by a certain flip angle (FA) spinning protons out of equilibrium. Immediately after the RF pulse is switched off, the ^1H atoms start precessing and realigning with B_0 and the released energy corresponds to the voltage induced in a receive RF coil. This energy constitutes the signal intensity (SI) of the MR image and is correlated with spatial locations using gradient RF coils. Ultimately, the signal strength depends mainly on the tissue properties—i.e. T_1 , T_2 , and T_2^* , also known as longitudinal, transversal and effective transversal MR relaxation times, respectively—and magnetic field strength, as well as the MR imaging parameters (echo time TE, repetition time TR, and FA, amongst others). Contrast agents such as gadolinium can be used to enhance the contrast and diagnostic properties of the MR image by modifying the MR relaxation times of the excited spins—i.e. by effectively shortening both T_1 and T_2 , with a dominant effect on T_1 in most cases.^{1,2} This characteristic is especially useful to detect inflammation or increased blood flow.

Multiple sclerosis (MS) is a chronic inflammatory disorder of the central nervous system (CNS). It involves the recruitment of immune cells from the periphery to the CNS via disruption of the blood-brain barrier (BBB), causing myelin destruction and neuronal damage and ultimately producing neurological impairment in humans.³⁻⁵ Preclinical studies on relapsing-remitting MS (RRMS), characterized by worsening phases (relapses) followed by partial or complete recovery phases (remissions), involve mainly a well-established mouse model called Experimental Autoimmune Encephalomyelitis (EAE).^{6,7} Because of the above-mentioned characteristics, magnetic resonance imaging (MRI) with gadolinium-based contrast agents (GBCAs) is the gold standard in the clinic to diagnose and monitor lesion activity in MS patients^{8,9} and animal studies.¹⁰⁻¹² Despite allowing the visualization of leaky BBB and white matter lesions, manual lesion delineation and quantification in the EAE mouse model is

challenging due to their diffuse nature with indistinct boundaries,¹¹ which makes the process highly subjective and prone to observer bias. Thus, there is a need for a robust and objective method of quantification. Moreover, GBCAs lack specificity and, recently, the increasing concern regarding their accumulation in the brain demands other diagnostic tools due to potential neurotoxicity.^{13,14} T_1 mapping techniques—and quantitative MRI in general—provide parametric maps that can help measuring biological changes caused by disease, and hence be used as sensitive imaging biomarkers.¹⁵

Another way to monitor and quantify inflammatory activity entails tracking immune cells *in vivo* by means of fluorine-19 (^{19}F) MRI using ^{19}F -loaded nanoparticles (NPs). Fluorinated compounds do not naturally exist in biological tissues—except in inorganic form, e.g. teeth and bones—, producing background-free images.¹⁶ The detected ^{19}F signal derived from exogenous ^{19}F compounds is thus proportional to the amount of ^{19}F nuclei, allowing *in vivo* quantification over time. Moreover, its gyromagnetic ratio ($\gamma/2\pi = 40.08 \text{ MHz} \cdot \text{T}^{-1}$) is close to that of ^1H ($\gamma/2\pi = 42.58 \text{ MHz} \cdot \text{T}^{-1}$), providing advantageous MR signal properties. These characteristics make ^{19}F -MRI a unique imaging modality with inherent selectivity and specificity.^{17,18}

However, the relatively low concentration of accumulated ^{19}F -loaded NPs *in vivo* results in a low signal-to-noise ratio (SNR), thereby limiting detection and challenging quantification. Therefore, to boost SNR while maintaining high spatial resolutions, long scan times are needed.¹⁹ As a result, SNR-efficient RF pulse sequences such as RARE (Rapid Acquisition with Relaxation Enhancement)²⁰ are preferred for low SNR scenarios.^{21,22} RARE is a fast spin-echo imaging technique essentially derived from the conventional spin-echo, in which the combination of two RF pulses (a 90° -excitation and a 180° -refocusing RF pulse) produces one echo per TR. In RARE, each 90° -excitation RF pulse is followed by a train of N 180° -refocusing RF pulses, generating N echoes per TR. The echo train length (ETL) parameter determines the number of echoes formed during each TR.

Moving to higher magnetic field strengths²³⁻²⁵ as well as the use of surface RF coils²⁶ are common approaches to improve SNR. In preclinical MRI, the market has seen a growing interest in cryogenically-cooled transceiver surface RF

probes (Cryoprobe[®], CRP). These provide further SNR gains—typically by a factor of up to 3-4 compared to conventional room-temperature RF coils—due to a reduction in thermal noise of the receiver circuitry (RF probe and preamplifier).^{27,28} Taking advantage such an SNR gain, one could increase spatial resolution or reduce scan time. Importantly, SNR gain could be employed to reduce detection limits, crucial for X-nuclei MRI.

Despite the SNR-boosting capabilities of the CRP technology, transceive surface RF probes exhibit a strong intrinsic variation in the excitation (B_1^+) field and RF coil sensitivity (B_1^-), usually referred to as B_1 inhomogeneity, whose effects are more evident at higher field strengths.^{29,30} As a result, both excitation flip angle (FA) and sensitivity are spatially dependent: their magnitude is greatest closest to the RF coil surface, and rapidly decreases further away. This reduces image homogeneity and severely hampers quantitative measurements and T_1 image contrast. B_1 correction methods aim to improve these limitations. However, while sensitivity can be easily corrected,³¹⁻³³ B_1^+ field inhomogeneity correction entails more challenges. Several measures can be taken during acquisition in order to partially mitigate B_1^+ inhomogeneities, from adiabatic pulses³⁴ through dielectric materials³⁵ to B_1^+ shimming.³⁶ Retrospective B_1^+ correction methods are, however, the most commonly applied to achieve signal uniformity due to their simplicity, since they do not typically require RF pulse programming or new RF coil designs. In a first step, the actual FAs are measured using FA mapping techniques^{37,38} and afterwards plugged into an analytical description linking the SI to the FA and relaxation parameters (SI equation) or numerical simulations³⁹⁻⁴¹ of the RF pulse sequence used. To date, gradient-echo⁴²⁻⁴⁴ and spin-echo imaging techniques^{45,46} have successfully benefited from this approach. However, RARE and derived fast spin-echo approaches lack an exact analytical SI equation that describes their complex spin-echo and stimulated-echo configuration.^{47,48} Equally, other multi-echo imaging techniques such as Ultrashort Echo Time (UTE)⁴⁹ or Echo-Planar Imaging (EPI),⁵⁰ also lack such an equation and cannot therefore be corrected with conventional retrospective B_1^+ correction methods. Therefore, there is a need for novel solutions when using more complex RF pulse sequences.

The author's approach in this context was to implement, apply and validate three B_1 correction methods using RARE imaging in combination with transceive surface RF probes.⁵¹ Due to the more challenging characteristics of the ^{19}F signal, these were first developed using ^1H -MRI and applied to test phantoms and mouse brains, *in vivo* and *ex vivo*. The goal was to increase image homogeneity and reduce errors to less than 10% for SI quantification and T_1 contrast. The starting point was a *sensitivity correction* method, commonly used to correct B_1 inhomogeneities. A *model-based method* was developed to meet the challenge that the unavailability of an exact analytical SI equation represents. The method uses a model of the SI of RARE as a function of FA and T_1 computed from actual MR measurements. Finally, a *hybrid correction* was implemented as a combination of the *model-based* and *sensitivity correction* approaches. All three correction methods substantially improved image homogeneity. Corrected images were suitable for signal quantification and T_1 contrast and showed comparable results between the three methods.

In a second step, these methods were applied to ^{19}F -MRI in order to quantify neuroinflammation *in vivo* using a ^{19}F -CRP.⁵² ^{19}F imaging adds an extra complexity to the application of the previously developed approaches, since:

(1) the sparse nature of the ^{19}F signal as well as the low SNR and the lack of an *a priori* known location are additional challenges for B_1 correction methods and for the reliability of signal quantification;

(2) the ^{19}F -CRP is single-tuned (i.e. it is tuned only to the ^{19}F frequency) due to its quadrature design,⁵³ although for X-nuclei—especially ^{19}F —the RF coil design should ideally allow ^1H imaging. This complicates the registration of ^{19}F images on anatomical images, overshadowing the SNR advantage (factor of $\sqrt{2}$) and the higher B_1 homogeneity of the quadrature configuration when compared to linear designs;⁵⁴

(3) the registration process—i.e. the process whereby two or more images are transformed into the same coordinate system to allow voxel-wise comparison—is challenged by pathologically-related macroscopic structural changes in the EAE brain^{55,56} which confound analysis during longitudinal studies, making registration a complex, non-trivial problem.

To solve these challenges, the author evaluated the previously proposed B_1 correction techniques for the low SNR conditions present in ^{19}F -MRI and introduced the use of (1) an approach to compute concentration uncertainty maps and SNR requirements using Monte Carlo simulations in order to evaluate the quality of the B_1 -corrected ^{19}F -signal quantification, and (2) an *in vivo* MRI workflow to facilitate localization of ^{19}F -MR images from the ^{19}F -CRP on anatomical images acquired from a ^1H volume resonator. Also, to apply a *model-based B_1 correction*, ^{19}F T_1 values from ^{19}F -labelled inflammatory cells were measured. Finally, to quantify changes associated to brain inflammation in longitudinal studies, (3) a robust registration method was implemented that enabled intra-subject registration even when macroscopic anatomical changes were present and allowed voxel-wise comparison needed for quantification. This registration process was applied to contrast-enhanced T_1 maps of EAE mice over time and evidence confirmed that this method can be used to robustly and objectively quantify gadolinium lesion burden.

These valuable methods are highly relevant to the study and monitoring of a broad range of diseases—here applied to neuroinflammation—and will open the way to future research using SNR-efficient transceive surface RF technology in combination with fast imaging techniques.

2. Methods

This part of the thesis contains and uses the methods published in:

- **Ramos Delgado P**, Kuehne A, Periquito J, Millward JM, Pohlmann A, Waiczies S, Niendorf T. *B₁ Inhomogeneity Correction of RARE MRI with Transceive Surface Radiofrequency Probes*. *Magnetic Resonance in Medicine*, 2020; 84(5):2684-2701. DOI: 10.1002/mrm.28307
- **Ramos Delgado P**, Kuehne A, Aravina M, Millward JM, Vazquez A, Starke L, Waiczies H, Pohlmann A, Niendorf T, Waiczies S. *B₁ Inhomogeneity Correction of RARE MRI at Low SNR: Quantitative In Vivo ¹⁹F-MRI of Mouse Neuroinflammation with a Cryogenically-cooled Transceive Surface Radiofrequency Probe*. *Magnetic Resonance in Medicine*, 2021; 87(4):1952-1970. DOI: 10.1002/mrm.29094
- Millward JM, **Ramos Delgado P**, Smorodchenko A, Boehmert L, Periquito J, Reimann HM, Prinz C, Els A, Scheel M, Bellmann-Strobl J, Waiczies H, Wuerfel J, Infante-Duarte C, Chien C, Kuchling J, Pohlmann A, Zipp F, Paul F, Niendorf T, Waiczies S. *Transient Enlargement of Brain Ventricles During Relapsing-Remitting Multiple Sclerosis and Experimental Autoimmune Encephalomyelitis*. *JCI Insight*, 2020; 5(21):e140040. DOI: 10.1172/jci.insight.140040

and contains text, statements, passages and figures from these publications.

2.1. Magnetic resonance hardware

All experiments were performed on a 9.4 T small animal MR scanner (BioSpec 94/20, Bruker BioSpin, Ettlingen, Germany) operating at 400 MHz (¹H) and 376 MHz (¹⁹F).

B₁ correction methods were applied to and validated on ¹H images acquired using transceive surface RF probes: a ¹H-CRP (Bruker BioSpin) with two elements operating in quadrature mode (inner diameter [ID]=20 mm) and a room-temperature surface RF coil (RT, Bruker BioSpin) consisting of a single loop (ID=20 mm). Reference images were acquired with volume resonators with approximately uniform excitation and reception fields. For this, a small in-house

built mouse head RF coil (ID=18.4 mm)⁵⁷ and a larger RF coil (ID=72 mm, Bruker BioSpin) tailored for rat body imaging were used.

¹⁹F-MRI experiments were conducted using a ¹⁹F-CRP (Bruker BioSpin) with two elements operating in quadrature mode (ID=20 mm).⁵⁸ Anatomical images were measured using the larger volume resonator and reference ¹⁹F images were acquired using the small mouse head RF coil.

The animal dataset utilized to develop the longitudinal intra-subject registration process was acquired using the small mouse head RF coil.

2.2. ¹⁹F/¹H imaging setup

As previously mentioned, the ¹⁹F-CRP is single-tuned to the ¹⁹F frequency and hence cannot produce co-localized anatomical and ¹⁹F-CRP images. To achieve this, an imaging setup including 3D-printed components was devised.

Animal bed modification. The standard animal bed uses a lever that elevates the bed, lifting the mouse head closer to the ¹⁹F-CRP. This feature hampers position reproducibility. To ensure spatial alignment of both ¹⁹F-CRP and anatomical images, a 3D-printed blocking component (Y-axis blocker) was designed to eliminate movement in the Y-axis (**Figure 1A**). Additionally, a new head holder was designed and 3D-printed to place the mouse head closer to the CRP surface (**Figure 1A**).

¹H-MRI setup. The 72-mm volume resonator was positioned around the centre tube holding the ¹⁹F-CRP. Anatomical images were acquired after a CRP replica (dummy)—inserted from the back of the scanner—was kept in place while the animal bed was inserted from the front.

¹⁹F-MRI setup. Both animal bed and dummy were removed and the ¹H-volume resonator was retracted towards the back of the scanner. The ¹⁹F-CRP was mounted as instructed by the vendor.

A ¹⁹F-NPs reference cap (24 mM NPs in 1 mL 0.75% agarose sealed with PARAFILM® (thickness=0.14 mm, Sigma-Aldrich, Saint Louis, MO, USA), dimensions (20×15) mm², thickness≈1.5 mm) was placed over the mouse head to perform ¹⁹F-CRP reference power adjustments and to acquire images for

quantification (**Figure 1B**). Afterwards, it was removed to acquire *in vivo* ^{19}F images (**Figure 1C-E**).

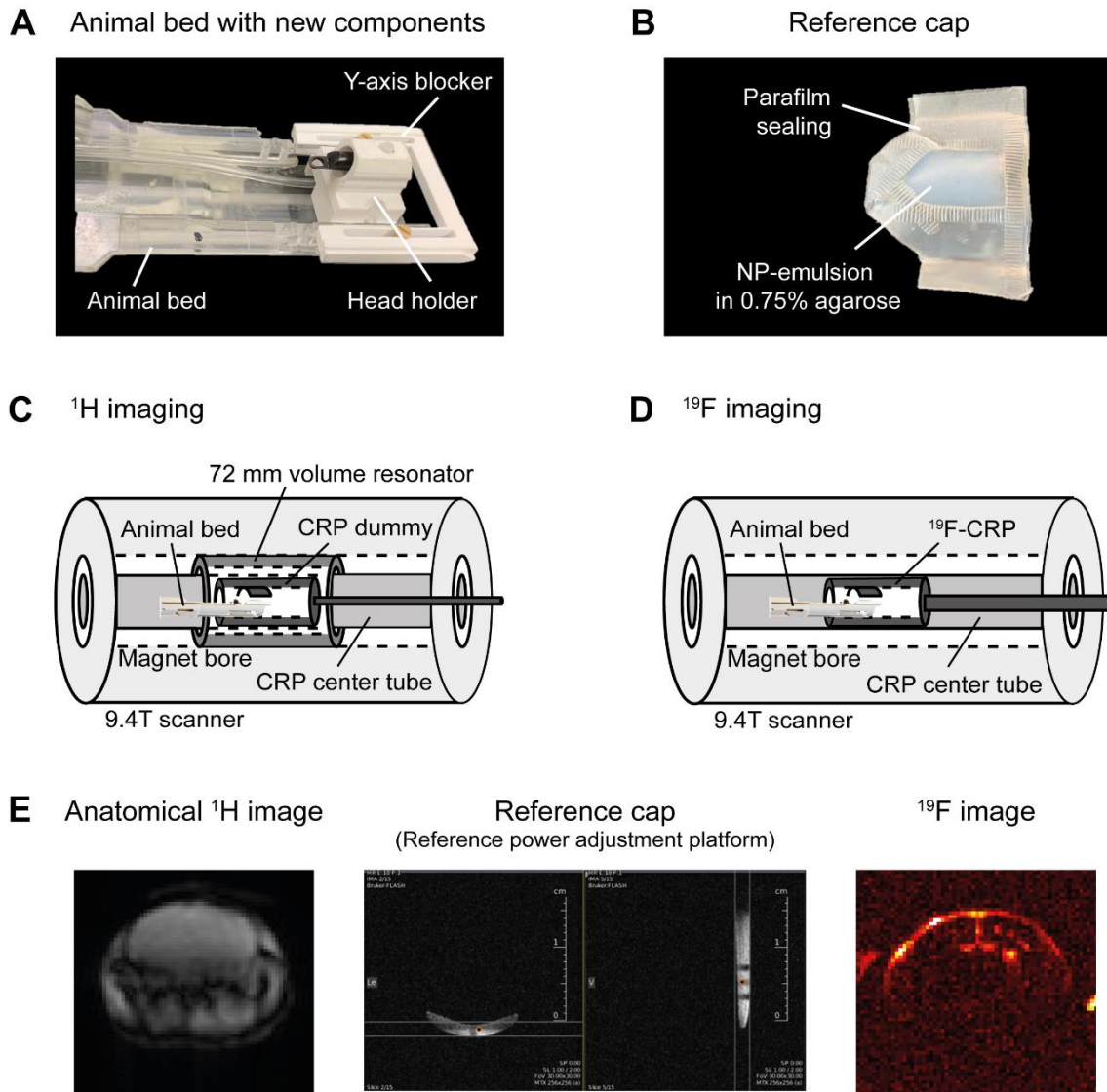


Figure 1. “Anatomical and ^{19}F imaging setup designed for a single-tuned ^{19}F -CRP. (A) Close view of the animal bed provided by the vendor with a custom-designed component that avoids mobility in the Y-axis (Y-axis blocker) and a new head holder to bring the animal’s head closer to the surface of the CRP. (B) Reference cap containing ^{19}F -loaded NPs to perform ^{19}F -CRP reference power adjustments and as reference for quantification. (C-D) $^1\text{H}/^{19}\text{F}$ imaging setups. (E) Exemplary *in vivo* images: anatomical images and slice planning are performed using a 72-mm volume resonator and a CRP dummy. Afterwards, reference power calibrations are carried out using the reference cap and ^{19}F images are acquired using the ^{19}F -CRP” (Ramos Delgado P, Kuehne A, Aravina M, et al. 2021)

2.3. Test phantom, animal preparation and pre-clinical MR experiments

All animal experiments were approved by the Animal Welfare Department of the LAGeSo State Office of Health and Social Affairs in Berlin and in accordance with international guidelines on reduction of discomfort (86/609/EEC). In all animals, respiration and temperature were monitored and kept constant during the examinations.

Reference power calibrations on ^1H transceiver surface probes were performed on 2-mm slices parallel and close to the probe surface. ^{19}F -CRP reference power calibrations were performed on 1-mm slices parallel and close to the probe surface using reference caps. All ^{19}F images were acquired as repetitions in axial and sagittal orientation. Noise scans (NEX=1 and reference power=0 W) were acquired after each ^{19}F RARE image for SNR map computation.

2.3.1. B_1 inhomogeneity correction in ^1H transceiver surface RF probes

Uniform phantom preparation. A uniform phantom consisting of a 15-mL tube (ID=14.6 mm, length=120 mm, wall thickness=0.8 mm; Fischer Scientific, Waltham, MA, USA) containing water doped with gadolinium (Magnevist® 0.5 mmol/mL; Bayer Vital, Leverkusen, Germany; $T_1 \approx 800$ ms) was prepared.

Animal preparation for *ex vivo* and *in vivo* methods. B_1 correction methods were validated *ex vivo* on the central nervous system of a SJL/J female mouse, perfused with a phosphate-buffered saline (Biochrom GmbH, Berlin, Germany), fixed in paraformaldehyde (PFA; Santa Cruz Biotechnology, Inc., Dallas, TX, US), and placed into a 15-mL tube filled with 4% PFA. *In vivo* experiments were carried out on a healthy SJL/J mouse anesthetized with 2.7% isoflurane (Abbott GmbH & Co., Wiesbaden, Germany) and stabilized with 1.6% during scanning.

MR experiments. RARE scans (TE/TR=2.49/1000 ms, echo train length (ETL)=8, receiver bandwidth (BW)=50 kHz, centric phase encoding, field of view (FOV)=(25×25) mm², matrix=128×128, 3 slices of 2 mm thickness, flipback) were acquired using the ^1H -CRP and the small mouse head volume resonator (reference). Acquisition time (TA)=1 hour for the uniform and *ex vivo* phantoms and TA=30 minutes for the *in vivo* mouse.

To assess T_1 contrast and quantification performance, four 50-mL cell culture flasks ((79.7×42.6×25) mm³, Fischer Scientific) filled with solutions of two different ¹H-atom concentrations: 100% water, 50% water and 50% deuterium oxide (Sigma-Aldrich, Saint Louis, MO, USA) were used. Gadolinium was added to the mixtures to achieve two different T_1 values (490 and 1525 ms). RARE scans (same parameters as above, with and without flipback) were acquired using the 50-mL cell culture flasks and the RT loop RF coil. Reference images were measured with the 72-mm volume resonator.

Corresponding T_1 maps for all samples were measured using RARE with variable TR (RAREVTR: TR ranging from 150 to 14500 ms, other parameters were kept the same).

2.3.2. B_1 inhomogeneity correction at low SNR using ¹⁹F transceiver surface RF coils

Uniform phantom preparation and MR measurements. A test uniform phantom consisting of a 15-mL tube containing 0.2 mM of 2,2,2-trifluoroethanol (Carl Roth GmbH & Co. KG, Karlsruhe, Germany) in water was used to assess B_1 correction performance in low SNR scenarios far from the probe surface. To achieve $T_1 \approx 1870$ ms (*in vivo* PFCE-NPs T_1 , *Results*), 0.006 mM gadolinium was used. A ¹⁹F-MR image of the test uniform phantom (RARE: TE/TR=4.62/1000 ms, ETL=32, FOV=(25×25) mm², matrix=96×96, 5 slices (gap/thickness=0.5/2 mm), BW=50 kHz, centric encoding with flipback, TA=3 seconds, axial orientation) was acquired with the ¹⁹F-CRP. A reference ¹⁹F image (RARE: same parameters, TA=1 hour) and a T_1 map (RARE with variable TR=250-10000 ms, ETL=2, linear phase encoding, other parameters same as RARE scan. TA=24 minutes) were acquired with the ¹H/¹⁹F mouse head volume resonator for comparison.

Induction of experimental autoimmune encephalomyelitis (EAE). EAE was induced in female SJL/J mice using 250 µg PLP₁₃₉₋₁₅₁ (Pepceuticals Ltd., Enderby, United Kingdom) and 800 µg mycobacterium tuberculosis H37Ra (Difco Laboratories, Thermo Fisher Scientific). Mice were also administered 200 ng of pertussis toxin (List Labs, Campbell, CA, USA) on day 0 and day 2. Animals were weighed and scored daily for disease signs using a 0-5 scale: 0, no disease; 1, tail weakness and righting reflex weakness; 2, paraparesis; 3,

paraplegia; 4, paraplegia with forelimb weakness or paralysis; and 5, moribund or dead. Intravenous injections of ^{19}F -NPs (10 μmol PFCE in 200 μL) were administered daily from day 5 following EAE induction until the experiment end.

Ex vivo phantom preparation. An EAE mouse was perfused, fixed and its central nervous system placed into a 15-mL tube filled with 4% PFA as described above.

MR methods in EAE mice. *In vivo* ^{19}F -NPs T_1 was calculated for *model-based corrections* in $n=3$ EAE mice using a combination of ketamine-xylazine (Ketamidor 100mg/mL, WDT, Garbsen, Germany; Rompun 2% 20mg/mL, Bayer AG; initial dose 400 μL , followed by 100-200 μL injections administered intraperitoneally every 45 min until the end of the MR examination) to avoid confounding ^{19}F signal. Due to the inherent ^{19}F characteristics (low SNR, signal sparsity, lack of an a priori known location), determining *in vivo* T_1 with T_1 mapping was unfeasible. MR spectroscopy techniques were applied using the $^1\text{H}/^{19}\text{F}$ volume resonator:

- Non-localized spectroscopy (block pulse, 10 TRs: 250-10000 ms, NA=64. TA=35 minutes) to compute T_1 values of the two reference caps (24 mM, 60 mM).
- Localized spectroscopy (PRESS) to compute T_1 values in the brain after ^{19}F -NP administration in *ex vivo* phantoms ($n=3$, 12 TRs: 250-15000 ms, NA=64. TA=32 minutes) and *in vivo* mice ($n=3$, 8 TRs: 412.5-13000 ms, NA=128. TA=1 hour and 8 minutes). A default B_0 field map was measured before each experiment, to optimize shim adjustment (MAPSHIM) computed on ^1H using a 3D cuboid shape fitting the mouse brain.

In vivo ^1H and ^{19}F images were acquired on another $n=3$ EAE mice from which $n=2$ animals are shown. These were anesthetized with isoflurane (2.0% initial dose, 0.5-1.0% maintenance). Slice planning and anatomical images (FLASH: TE/TR=3/120 ms, same FOV, matrix=256 \times 256, TA=30/15 minutes per orientation *ex vivo/in vivo*, respectively) were acquired with the 72mm-volume resonator.

^{19}F -MR images were acquired with the ^{19}F -CRP, with (RARE: same parameters, 15 min per orientation both *ex vivo* and *in vivo*) and without (RARE: same parameters, 6 h/45 min per orientation *ex vivo/in vivo*, respectively) reference cap. Reference images were acquired with the $^1\text{H}/^{19}\text{F}$ volume resonator in *ex vivo* phantoms: reference cap (^{19}F RARE: same parameters, 30 minutes per orientation), phantoms (^{19}F RARE: same parameters, TA=6 hours per orientation; ^1H FLASH: same parameters, TA=1 hour per orientation).

2.3.3. Development of registration methods for longitudinal EAE studies

The developed registration methods were applied to a longitudinal *in vivo* EAE dataset ($n=9$ mice, 1.0-1.5% isoflurane). After anatomical baseline images were acquired, gadolinium was infused via an intravenous cannula over 2 minutes. T_1 -weighted images (T_{1w} , MDEFT: TE/TR=3.89/15 ms, FA=20°, NA=2, slices/thickness=12/0.5 mm, spatial resolution=(75×75) μm^2 , TI=950 ms, coronal orientation, TA=2 minutes and 5 seconds) and T_1 maps pre- and post-contrast (RAREVTR: TE=11.53 ms, 6 TRs: 0.38-7 s, ETL=4, spatial resolution=(150×150) μm^2 , 11 slices of 0.5 mm thickness, TA=3 minutes and 25 seconds) were acquired. Slice positioning was kept constant throughout the study: axial slices were positioned parallel to the base of the brain; coronal slices were positioned perpendicular to axial slices, covering the brain from the olfactory bulb/frontal lobe fissure to the cervical spinal cord.¹¹ Mice were imaged at baseline, 2 days before immunization, and every 2-3 days after immunization, until day 64 after EAE induction.

2.4. ^{19}F -MRI data pre-processing

All post-processing was performed using customized software developed in MATLAB (The MathWorks Inc., Natick, MA, USA). All ^{19}F data followed the same pre-processing workflow:

1. Complex averaging over smaller subsets of the total number of repetitions to mimic different scan times followed by a sum-of-squares (SoS) combination of the two channels (^{19}F -CRP):
 - Uniform phantom: one subset of a 3-second acquisition.

- *Ex vivo* phantoms: four subsets corresponding to 15 minutes and 1-3-6 hours acquisitions. Same with $^1\text{H}/^{19}\text{F}$ volume resonator for comparison.
 - *In vivo* mice: three subsets corresponding to 15-30-45 minutes.
 - Reference caps: one subset corresponding to the total scan time.
2. Noise bias correction:^{59,60}
- ^{19}F -CRP: non-central χ distribution (lookup table for $n=2$ channels).
 - Volume resonator: Rician distribution (lookup table for $n=1$ channels).
3. Thresholding (SNR-cutoff=3.5) and removal of isolated groups of <3 connected pixels.

2.5. B_1 field characterization in transceive surface RF probes

2.5.1. Double angle method: theory and method extension

To correct for B_1 inhomogeneities, the transmit (B_1^+) and receive (B_1^-) fields of the transceive surface RF coils used were computed using the Double Angle Method B_1 mapping technique.⁶¹ This method typically uses the SI ratio of two gradient-echo images to determine the FA distribution (and consequently B_1^+):

$$FA(r) = \cos^{-1} \left(\left| \frac{SI_{2\alpha}}{2 \cdot SI_{\alpha}} \right| \right) \quad (1)$$

with $FA(r)$ being the FA distribution (i.e. FA map), and SI_{α} and $SI_{2\alpha}$ the SIs of the gradient-echo images with $FA(\alpha)=60^\circ$ and $FA(2\alpha)=120^\circ$, respectively. The main requirement is a long TR ($TR \geq 5 \cdot T_1$) to achieve full T_1 relaxation in the sample and hence eliminate T_1 dependence in SI_{α} and $SI_{2\alpha}$, which implies long scan times.

To increase the SNR and hence FA accuracy distal to the RF probe surfaces, an extension of this method was performed. Three FAs were used to compute separate FA maps ($60^\circ/120^\circ$ and $120^\circ/240^\circ$), which were denoised (10th-order polynomial using a polynomial fitting tool⁶²) and merged using an SNR-cutoff.

The transmit (B_1^+) field was computed using the following approximation tailored to the calculated RF pulses used:

$$B_1^+ = \frac{FA \cdot \pi / 180}{\gamma \cdot t_p \cdot S_{int} \cdot V} \quad (2)$$

with γ the gyromagnetic ratio ($\gamma=267.522 \cdot 10^6$ rad s⁻¹ T⁻¹ for ¹H, $\gamma=251.815 \cdot 10^6$ rad s⁻¹ T⁻¹ for ¹⁹F), t_p the pulse duration, S_{int} the area under the RF pulse, and V the related voltage.

The corresponding B_1^- fields were calculated using the low FA approximation^{63,64} using a separate gradient-echo measurement with FA=5°:

$$|B_1^-| = \frac{|B_1^+|}{|SI_{lowFA}|} \quad (3)$$

where the B_1^+ map and the low FA image were normalized by their respective maximum values. The B_1^- map was also denoised using a 10th-order polynomial fit.

2.5.2. Sample preparation and experiments

Sample preparation. Uniform phantoms with small T_1 ($T_1 \approx 300$ ms) that ensured full field of view (FOV) coverage under the transceive surface RF probes were used to reduce the required TR.

To characterize the ¹H-CRP, a 15-mL tube containing a mixture of water and copper sulphate (Carl Roth GmbH & Co. KG) was used. For the RT surface RF coil, a 50-mL cell culture flask filled with an aqueous solution of gadolinium was employed.

To characterize the ¹⁹F-CRP, a 15-mL tube as above containing a mixture of 33.3% 2,2,2-trifluoroethanol in water with 0.08 mM of gadolinium was used. To correct B_1 inhomogeneities on the reference caps, a high-¹⁹F concentration reference cap was constructed (60 mM NPs in 1 mL of 0.75% agarose, dimensions (20×15) mm², thickness~1.5 mm).

MR experiments. ¹H FA mapping was performed using FLASH measurements with nominal excitation FAs of 60°/120°/240° (¹H-CRP) and 60°/120° (RT) and with TE/TR=2.49/2000 ms, matrix=128×128, 3 slices with a slice gap of 0.5 mm and a thickness of 2 mm. FOVs of (25×25) mm² and (35×35) mm² were used, respectively, for the ¹H-CRP and the RT. Total acquisition time was 1 hour and 30 minutes.

^{19}F FA mapping was carried out both in axial and sagittal orientations using FLASH measurements with $\text{TE/TR}=2.16/2000$ ms, $\text{FOV}=(25\times 25)$ mm 2 , matrix=96 \times 96, 5 slices (gap/thickness=0.5/2 mm), and flip angles $\text{FA}=60^\circ/120^\circ/240^\circ$ (uniform phantom) and $\text{FA}=60^\circ/120^\circ$ (reference cap). Total acquisition time was 1 hour per orientation.

In both nuclei, B_1^- maps were acquired using a FLASH measurement with a nominal $\text{FA}=5^\circ$ (rest of the parameters were kept the same).

2.6. Rapid Acquisition with Relaxation Enhancement (RARE)

2.6.1. Basic principles

Rapid Acquisition with Relaxation Enhancement (RARE) is a fast spin-echo imaging method which enables a drastic reduction in scan time.²⁰ After a 90° slice-selective excitation RF pulse, a train of N equidistant refocusing RF pulses follows, generating N echoes per TR. The echo train length (ETL) parameter determines the number of echoes formed during each TR interval. The effective echo time (TE_{eff}) is the time between the excitation RF pulse and the acquisition of the k-space line with zero phase encoding. Echo spacing (ESP) is the time between two consecutive echoes. Each echo in RARE has an independent phase encoding.

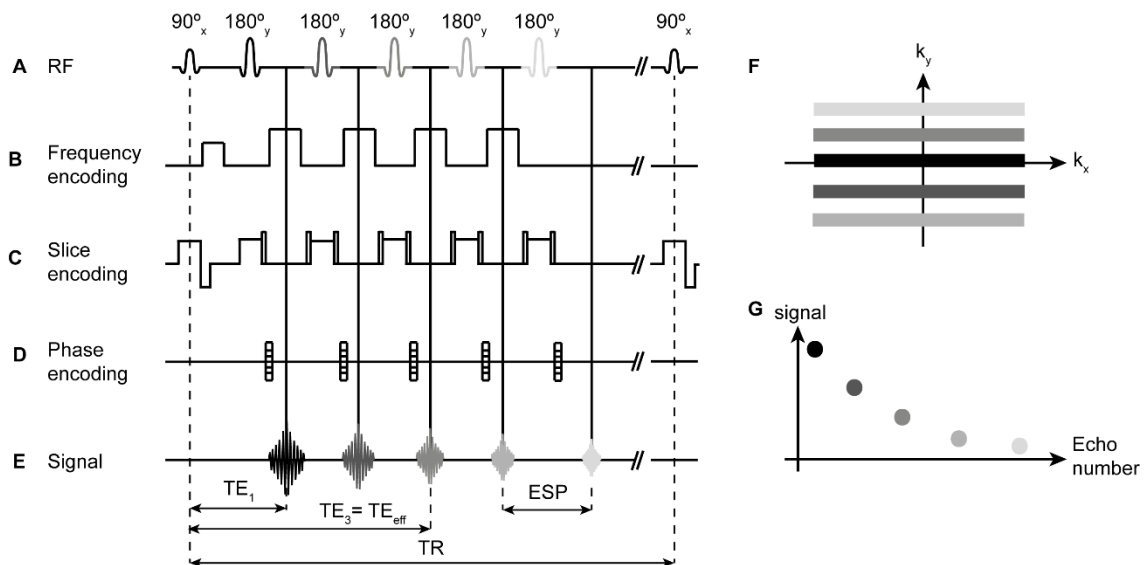


Figure 2. RARE sequence diagram for an ETL=5 with centric Cartesian phase encoding.

(A) RF pulse train composed of one 90° -excitation pulse and five 180° -refocusing pulses (ETL=5), (B) frequency encoding gradients, (C) slice selective excitation, (D) echo-independent

phase encoding, **(E)** echo formation. In **(F)** the corresponding centric k-space filling is shown: the first echo is assigned to the centre of k-space and the following echoes are placed at the sides. **(G)** shows the signal achieved for each echo. The different shades of grey represent the decreasing (T_2 decay) signals achieved.

Due to the complexity of this RF pulse sequence, no exact analytical equation exists that relates the achieved SI with the RF pulse sequence parameters such as the FA, relaxation times, TE, TR, etc. Moreover, small errors in FA due to B_1 inhomogeneity or slice profile imperfections, or sequence timing mismatches will translate in errors in the generated echoes.^{47,48}

2.6.2. Empirical RARE signal intensity model

Retrospective B_1^+ correction typically uses the SI equation of the imaging sequence used. This is, however, not feasible for RARE. Therefore, its SI was modelled as a function of FA and T_1 based on empirical measurements obtained through MR experiments. This approach was validated using ^1H imaging.

Samples with different T_1 (NMR tubes, Thermo Fischer Scientific, Waltham, MA, USA) filled with aqueous solutions of gadolinium at different concentrations (0-0.5 mM) yielding T_1 between 190 and 2871 ms were used. RARE measurements (TE/TR=2.49/1000 ms, ETL=8, BW=50 kHz, centric phase encoding, FOV=(25×25) mm², matrix=128×128, 3 slices of 2 mm thickness. TA=5 minutes and 40 seconds) using the small in-house built were performed both with and without flipback (i.e. longitudinal magnetization recovery which improves SNR). Thirty-five reference RF powers were used to vary the excitation FA in 5° increments, between 5° and 160° (flipback) and between 5° and 110° (without flipback). T_1 maps of all phantoms were acquired using RAREVTR (TR=120-15000 ms, ETL=2, linear phase encoding, other parameters same as RARE scan).

The relationship between SI, FA, and T_1 was estimated using experimental data and a fitting tool. First, images were denoised using a spatially-adaptive non-local means filter,⁶⁵ and T_1 maps computed by fitting $S=S_0(1 - \exp(-TR/T_1))$ to the SIs using in-house developed software in MATLAB. $SI(FA=0^\circ)=0$ was assumed for all T_1 . For each T_1 sample, a circular region of interest (ROI) was drawn to extract average SI and T_1 values from the images and maps,

respectively. To model the $SI=f(FA, T_1)$ relationship a 7th-order polynomial was fitted to the experimental data using MATLAB's *polyfitn* function.

2.6.3. Simulated RARE signal intensity model

Extended phase graph (EPG) simulations describe the location of echoes and their amplitudes using algorithms to trace spin phase evolution pathways.³⁹⁻⁴¹

The ¹⁹F RARE SI model was calculated as a function of FA and T₁ relaxation value for RARE scans (TE/TR=4.62/1000 ms, ETL=32, FOV=(25×25) mm², matrix=96×96, 5 slices (gap/thickness=0.5/2 mm), BW=50 kHz, centric encoding with flipback. TA=1 h per orientation), for 20 equispaced T₁ values (150-2050 ms) and 32 excitation FAs (5°-160° in 5°-steps). Finally, an 8th-degree polynomial was fitted to the simulated data.

2.7. B₁ inhomogeneity correction techniques

2.7.1. Sensitivity B₁ correction method

The *sensitivity correction* is well established in the literature for correction of B₁⁻ inhomogeneities.³¹ A typical application is the correction of B₁⁻ inhomogeneities in a RF coil setup where a volume resonator is used for transmission and a surface RF coil (with or without cryo-cooled technology) for MR signal detection.

This method requires neither the characterization of the transceive RF coil used, nor the calculation of a RARE SI model and it is, therefore, directly applicable after image acquisition with little post-processing.

Figure 3A shows the needed steps to perform a *sensitivity correction*. A RARE image (same parameters) of the low-T₁ uniform phantom used for B₁ field characterization was used. Afterwards, a correction factor was computed as the inverse of the normalized uniform phantom image. Finally, the uncorrected image was multiplied by the estimated correction factor to correct for B₁⁻ inhomogeneities.

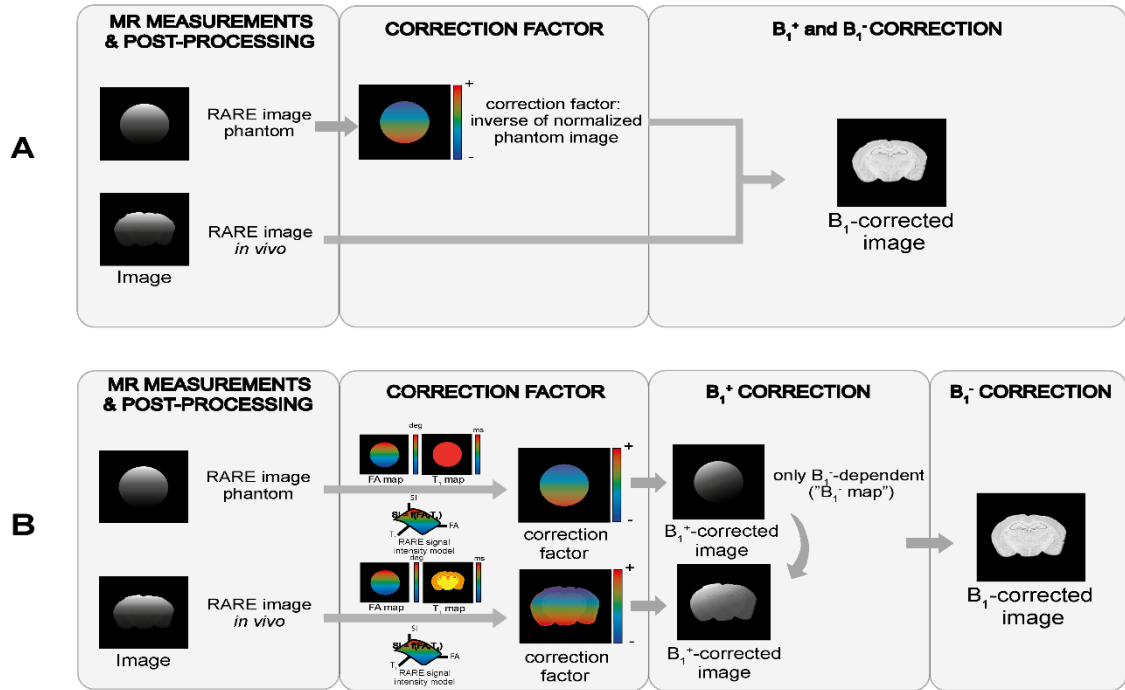


Figure 3. “Workflows of (A) sensitivity correction and (B) hybrid B_1 correction. The *sensitivity correction* merely requires dividing the sample image by that of a normalized uniform phantom. The *hybrid method* combined the *model-based* approach to perform a B_1^+ correction on the sample image and a uniform phantom image. The latter is then used to perform a B_1^- correction using the *sensitivity correction* method” (Ramos Delgado P, Kuehne A, Periquito J, et al. 2020)

2.7.2. Model-based B_1 correction method

The *model-based correction* uses a SI model of RARE (empirical or simulated) to retrospectively correct B_1^+ inhomogeneities, followed by a B_1^- correction. The workflow is summarized in **Figure 4**.

After characterizing the RF probe, a B_1^+ correction factor (f_{corr}) was computed:

$$f_{\text{corr}} = \frac{SI_{\text{nominal}}}{SI_{\text{actual}}} \quad (4)$$

with SI_{nominal} being the modeled RARE SI for a perfect 90° excitation, and SI_{actual} the modeled RARE SI for the actual excitation FA.

Applying this correction factor yielded a B_1^+ -corrected image:

$$\text{image}_{B_1^+\text{corr}} = \text{image} \cdot f_{\text{corr}} \quad (5)$$

In the few cases where the algorithm produced negative values (low-SNR regions), the correction factor was set to zero.

Dividing this B_1^+ -corrected image by the B_1^- map produced the final B_1 -corrected image:

$$\text{image}_{\text{corr}} = \text{image}_{B_1^+ \text{corr}} / B_1^- \cdot f_{\text{corr}} \quad (6)$$

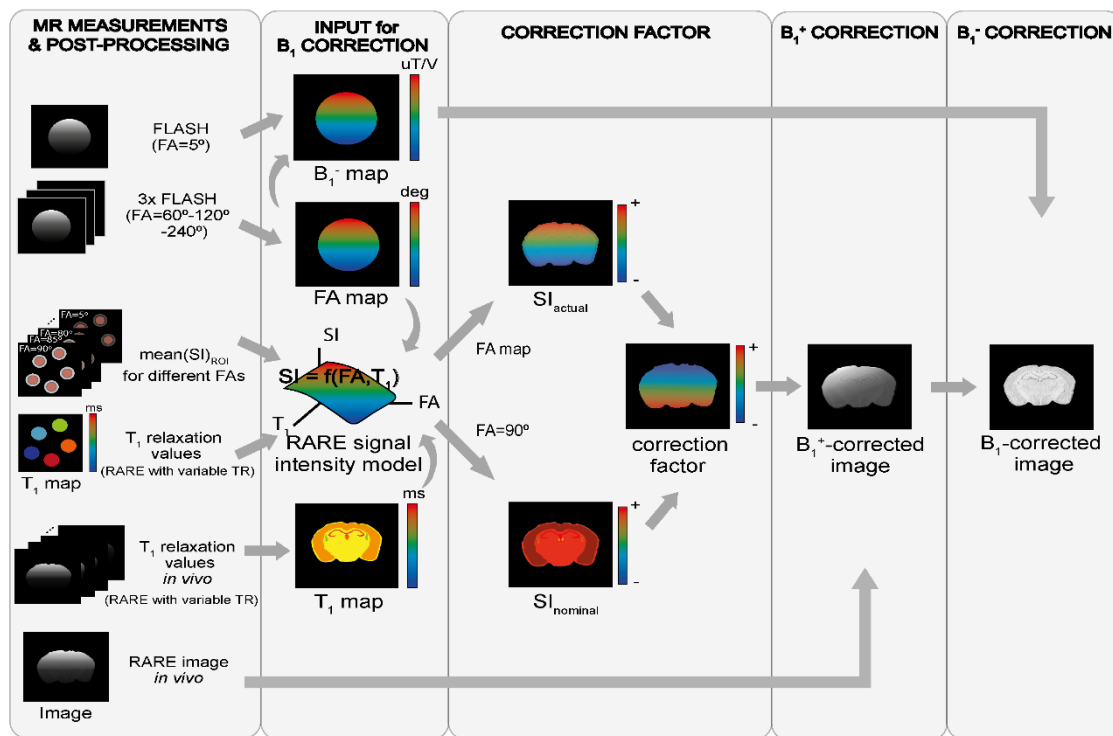


Figure 4. “Workflow of model-based B_1 correction. The necessary images and maps to be acquired are described in MR Measurements & Post-processing column. Then the flip angle (FA) and sensitivity (B_1^-) maps were calculated using the double angle method and the low flip angle approximation, respectively. The RARE signal intensity model was derived from a 2D fit of the signal intensities measured for different FAs and T_1 relaxation times using a volume resonator. The B_1^+ correction factor was computed pixel-wise for the actual FA and T_1 using the RARE signal intensity model. Applying this correction factor and the B_1^- map derived correction factor yielded the final B_1 corrected image” (Ramos Delgado P, Kuehne A, Periquito J, et al. 2020)

2.7.3. Hybrid B_1 correction method

This method combines the *sensitivity* and *model-based correction* (workflow in **Figure 3B**). After computing a *model-based B_1^+ correction* on the sample and uniform phantom image, a *sensitivity B_1^- correction* was calculated, where the

inverse of the B_1^+ -corrected uniform phantom image was applied as the B_1^- correction factor to the B_1^+ -corrected sample image.

2.8. B_1 correction method validation and uncertainty calculation

2.8.1. Central profile plots

The SI profile along a central line perpendicular to the RF coil surface was plotted against distance to the RF coil surface. Seven pixels across the width of the line were averaged, and the SIs were normalized to [0,1] to allow a better comparison. A quantitative comparison was performed by calculating the root-mean-square-error (RMSE) between each profile and the reference. Each profile was scaled to minimize the RMSE against the reference, in order to compensate for the arbitrary scaling and to provide a fair comparison.

2.8.2. Image homogeneity assessment

To quantitatively assess the uniformity of the corrected images, the *percentage integral uniformity* (PIU)⁶⁶ was computed for ROIs of different sizes. A PIU of 100% represents perfect image homogeneity. In the ^1H uniform phantom, five internally tangential circular ROIs with increasing diameter on the central vertical line were defined. For the brain images (*ex vivo*, *in vivo*), the cortex and basal ganglia/thalamus (left and right) were manually outlined, achieving three ROIs. In the ^{19}F uniform phantom, three internally tangential circular ROIs were defined to calculate PIU values.

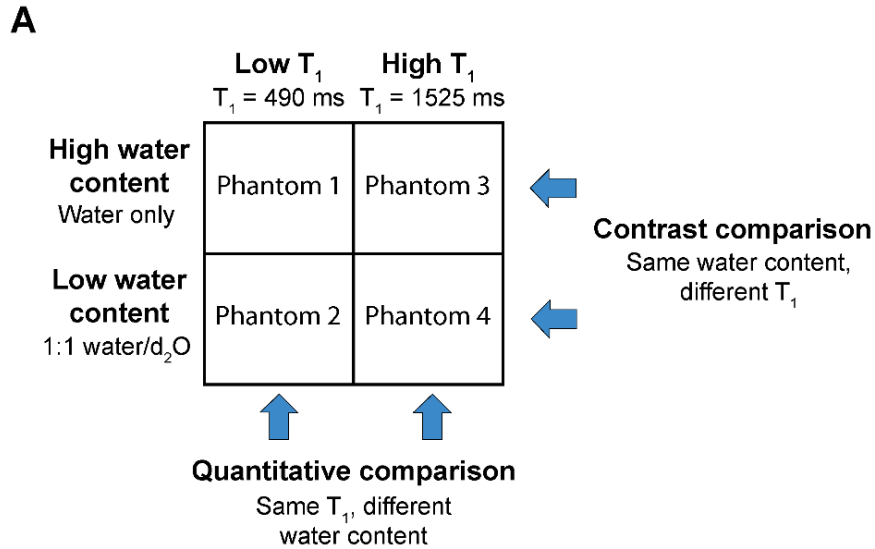
2.8.3. T_1 contrast and quantification performance

An experimental setup (**Figure 5A**) was used to assess T_1 contrast and quantification performance after ^1H B_1 correction by comparing substances with different water content (100% or 50%, respectively) and different T_1 relaxation times (490 or 1525 ms, respectively).

All acquired images (with and without flipback) were corrected using the three B_1 correction methods. Five ROIs were drawn at pseudo-randomized positions (**Figure 5B**) on all sets of images (three corrections, original and reference) for all flasks. For each of the flask image pairs described in **Figure 5A**, mean SI ratios were calculated using all possible ROI combinations for all sets. Mean absolute percentage errors (MAPE) were computed:

$$\text{MAPE} = \frac{\text{abs}(\bar{S}\text{I}_{\text{reference}} - \bar{S}\text{I}_{\text{corrected}})}{\bar{S}\text{I}_{\text{reference}}} \times 100 (\%)$$

with $\bar{S}\text{I}_{\text{reference}}$ being the mean SI ratio computed using all ROI combinations on the reference image pairs, and $\bar{S}\text{I}_{\text{corrected}}$ being that achieved using the corrected image pairs. Finally, the mean error and mean SD were calculated. An example of the workflow is shown in **Figure 5B**.



B Quantitative comparison for low T_1 (example):

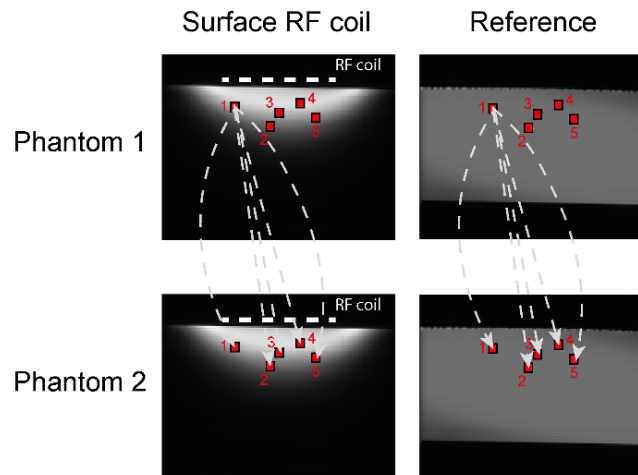


Figure 5. “Illustrations of validation methods. (A) To evaluate the performance of the correction methods (*sensitivity*, *model-based*, and *hybrid*), four phantoms with different water content and T_1 relaxation times were prepared. The quantitative assessment compared flasks with different water content for both low and high T_1 values. Similarly, contrast was evaluated by comparing phantoms with different T_1 values at low and high water content. **(B)** shows the ROI placement and depicts for one selected ROI the ratios that were calculated. In this manner, the

ratios for all possible ROI combinations in the corrected, original and reference images were calculated. The mean relative errors of these ratios with regard to those obtained in the reference served as quantitative measure for the validation” (Ramos Delgado P, Kuehne A, Periquito J, et al. 2020)

Statistical analysis. A non-parametric one-way ANOVA Friedman repeated measures test was performed (mean errors on the original data did not have a Gaussian distribution) followed by Dunn’s test where all corrections were compared to the original data (p -values <0.05 were considered significant). All statistical assessments were performed using GraphPad Prism 5 (GraphPad Software, La Jolla, CA, USA).

2.8.4. Monte Carlo SNR simulations for uncertainty calculation

Given the sparse nature of ^{19}F images and the spatially-varying B_1 fields of the ^{19}F -CRP, concentration uncertainty maps after B_1 correction were computed (**Figure 6**):

Step 1. Monte Carlo SNR simulations^{67,68} (1000 iterations) were performed using measured (T_1 values) and synthetic data (SI computed using the simulated RARE SI model). Simulation parameters (**Table 1**) were defined to mimic realistic excitation FAs, B_1 -values and SNRs within the sample. Shorter parameter ranges were chosen for the reference cap after inspection of the central region of the FA, B_1 and SNR maps obtained (i.e. region used for ^{19}F signal quantification). This was crucial to reduce matrix size and avoid memory problems.

Step 2. Noise levels for the prescribed SNR values were fixed for a 90° excitation and $B_1=1$ using a “reverse *model-based correction*” (inverse steps of the *model-based correction*).

Step 3. For each combination of reference and sample FA, B_1 and T_1 values, the CRP SI (for reference and sample) was calculated and separated in 2 channels. For each Monte Carlo iteration, complex Gaussian noise was added to both channels and a SoS reconstruction computed to simulate a non-central χ distribution. A noise bias correction was performed as described, followed by a *model-based correction*. Finally, the concentration was estimated using the 24 mM reference cap as a reference to determine absolute ^{19}F concentrations:

$$c_{sample} = \frac{SI_{sample} \cdot c_{ref}}{SI_{ref}} \quad (1)$$

where SI_{sample} and SI_{ref} are the SIs for the sample and the reference, respectively, and c_{sample} and c_{ref} are the corresponding concentrations. To compute SI_{ref} , a square-shaped ROI (3×3 pixels) was selected in a B₁-corrected homogeneous region, in the centre of the reference cap.

The mean SNR and mean and SD of the corrected SI throughout the 1000 iterations were determined for both reference and sample, along with the mean and SD of the concentration. Since the Monte Carlo samples conformed to a Gaussian distribution of mean≈1 (*Results*), the corresponding uncertainties in corrected SI and concentration were defined as SD×100 (%).

Step 4. To compute the uncertainty map of an acquired ¹⁹F image, measured data (FA, B₁⁻ and SNR maps, T₁ value) were fed to the corresponding Monte Carlo uncertainty model. The uncertainties were interpolated voxel-wise using a simple linear regression after logarithmically transforming the SNR and uncertainty data and eliminating SNR values<1.

Parameter definition

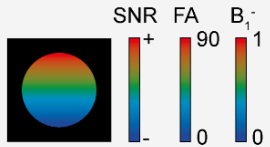
STEP 1

- **Number of Monte Carlo iterations**
- **Ground truth values** for SI and concentration (sample, ref.)
- **Sample:** excitation FA, normalized B_1^- , T_1 relaxation times (ex vivo, in vivo) and SNR
- **Reference cap:** excitation FA, normalized B_1^- , T_1 relaxation times (in agarose) and SNR
- **Lookup table** for bias correction
- **RARE SI model**

Compute fixed noise levels

STEP 2

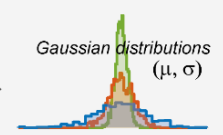
1. **“Reverse” model-based correction** to compute SI_{CRP} :
 - Sample: FA = 90°, $B_1^- = 1$, $T_1 = 1869$ ms
 - Ref.: FA = 90°, $B_1^- = 1$, $T_1 = 936$ ms
2. Calculate noiseSigma for defined SNR values



SNR simulations

STEP 3

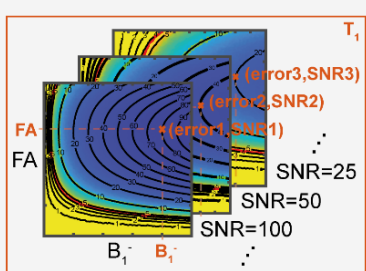
- For each FA, B_1^- and T_1 relaxation time of ref. and sample:
 1. Compute pixel CRP SI (“reverse model-based correction”)
 2. Separate in 2 channels
- For each Monte Carlo iteration:
 1. Add complex Gaussian noise and perform SoS reconstruction
 2. Perform noise bias correction
 3. Model-based B_1^- correction
 4. Determine concentration: $c_{sample} = \frac{SI_{sample} \times c_{ref}}{SI_{ref}}$ c = concentration
 SI = signal intensity
- 3. Compute statistics:
 - Mean SNR
 - Mean and SD of corrected SI
 - Mean and SD of concentration (signal quantification)



Error map estimation

STEP 4

Error dataset for desired (FA, B_1^- , T_1)



Linear fit in log-log plot and error map calculation (find error for desired SNR)

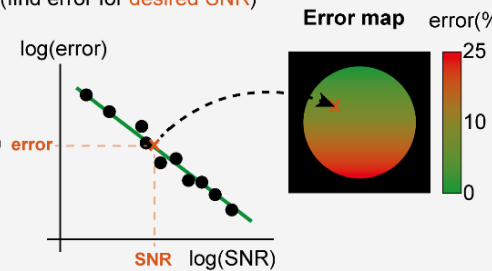


Figure 6. “Monte Carlo SNR simulation and uncertainty map estimation workflow using measured and synthetic data. After determining the noise levels for the defined SNR values, Monte Carlo simulations are performed for each FA, B_1^- and T_1 relaxation time of the sample and reference by adding noise, computing a noise bias correction and calculating a *model-based B_1^- correction*. Concentration was also estimated. Statistics including mean SNR, mean and SD of corrected SI and mean and SD of the concentration were computed after each run. These simulations are afterwards used to derive uncertainty maps for the measured data using the FA, B_1^- , T_1 and SNR measured at each pixel using a linear regression in a log-log plot (error vs SNR). Ref.: reference; SoS: sum-of-squares” (Ramos Delgado P, Kuehne A, Aravina M, et al. 2021)

Parameters	Initialization values	Ranges and steps	Number of elements
Ground truth data			
Ground truth SI sample	1	-	1
Ground truth SI reference cap	1	-	1
Ground truth concentration reference cap	1	-	1
Sample data			
Excitation FA (relative to 90°)	5° to 130°	1°-steps	126
Normalized B ₁ ⁻	0 to 1	0.01-steps	101
SNR values (fixed at 90° excitation)	0 to 1500	0 to 10 in 0.5-steps 11 to 25 in 1.0-steps 27.5 to 100 in 2.5-steps 105 to 500 in 5-steps 510 to 1500 in 10-steps	246
T ₁ values	936 ms 818 ms 1869 ms	-	3
Reference cap data			
Excitation FA (relative to 90°)	50° to 60°	5°-steps	3
Normalized B ₁ ⁻	0.8 to 0.7	0.05-steps	3
SNR value (fixed at 90° excitation)	500	-	1
T ₁ values	936 ms	-	1

Table 1. “Summary of simulation parameters for Monte Carlo SNR simulations” (Ramos Delgado P, Kuehne A, Aravina M, et al. 2021)

2.9. Development of registration methods for longitudinal EAE studies

Image post-processing was done using MATLAB, MIJ⁶⁹ and ANTs (Advanced Normalization Tools).^{70,71}

T₁-maps were computed from de-noised⁶⁵ T₁w-images with different TRs by fitting an exponential growth. The T₁w-image with the largest TR (i.e. 7 seconds, highest SNR) pre-contrast was used for the registration process. Before registration, these images underwent a pre-processing step to ensure the correct function of ANTs—deformation is constrained to be zero at the boundaries. First, an increase of the number of slices (×10 factor) was performed followed by padding. Maps were also padded.

“Multi-step 3D intra-subject registration (with consecutive rigid, affine and elastic registration steps) onto the first time point (pre-immunization) was performed on one of the pre-contrast RAREVTR T₁-mapping images (longest TR) using a cross correlation similarity method. The resulting warping fields were then applied to the T₁ maps. Images and maps were resliced and unpadding.

ROIs of the brain and cerebellum were manually defined for all animals using the baseline (tp_1) T_1 w-images and afterwards applied to the entire series. Minor changes onto ROIs were applied where needed. Average T_1 and ΔT_1 maps were computed. The difference pre- and post-contrast T_1 was calculated and plotted over time”.⁴ The workflow is depicted in **Figure 7**.

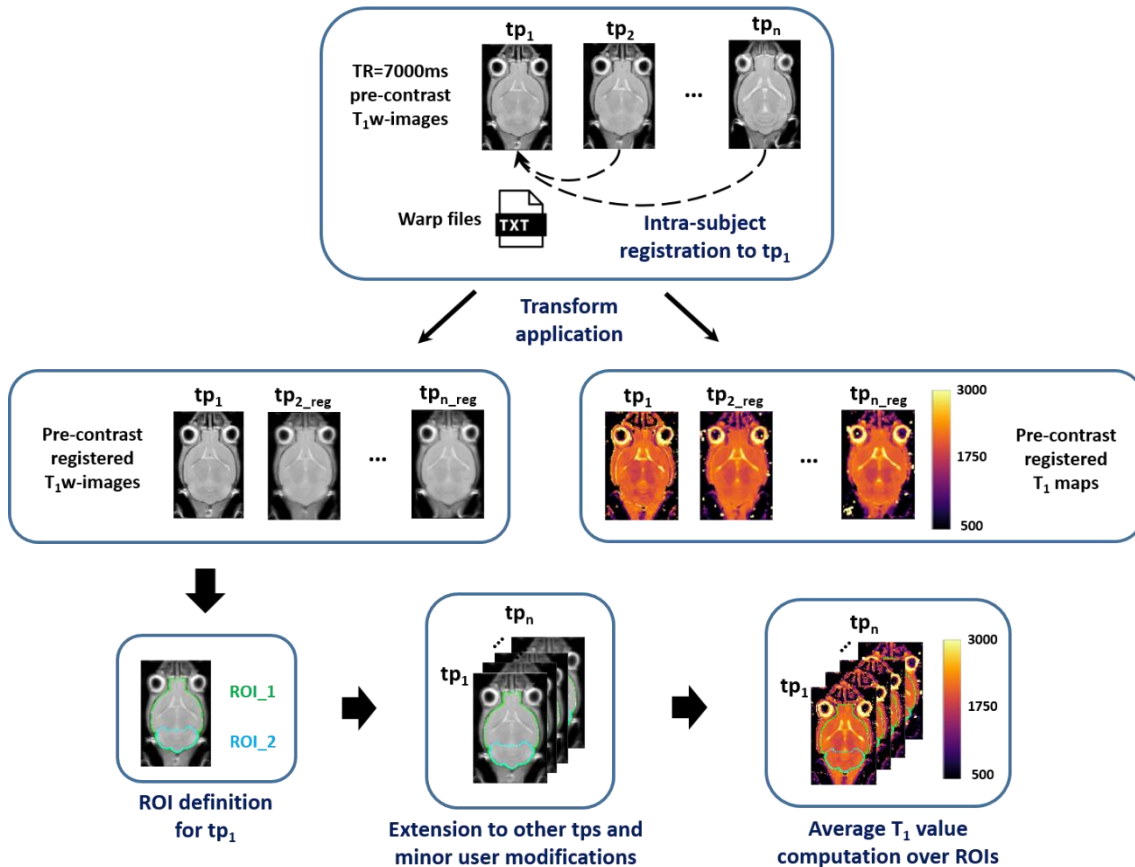


Figure 7. “Multi-step 3D intra-subject registration workflow. For each animal, pre-contrast T_1 w-images were registered to tp_1 . Warping files were applied to T_1 w-images and T_1 maps. ROIs were defined for brain (ROI_1) and cerebellum (ROI_2) using the registered pre-contrast T_1 w-images, replicated for the other timepoints and applied to the pre- and post-contrast T_1 maps to compute ΔT_1 ” (Ramos Delgado P, Millward JM, Huelnhagen T, et al. ESMRMB 2020)

Changes in T_1 were statistically evaluated using one-way ANOVA. P -values < 0.05 were considered significant. Data analysis was done using the statistical computing environment R v.3.3.4 (<https://www.R-project.org>) and GraphPad Prism.

3. Results

3.1. B_1 inhomogeneity correction in ^1H transceiver surface RF probes to enable signal quantification

This chapter contains and uses results that have been published in:

Ramos Delgado P, Kuehne A, Periquito J, Millward JM, Pohlmann A, Waiczies S, Niendorf T. *B_1 Inhomogeneity Correction of RARE MRI with Transceive Surface Radiofrequency Probes*. *Magnetic Resonance in Medicine*, 2020; 84(5):2684-2701. DOI: 10.1002/mrm.28307

and therefore contains text, statements, passages and figures from this publication.

As a first step towards ^{19}F signal quantification, three B_1 correction methods were implemented and validated using ^1H -MRI. B_1 mapping techniques were established to measure the B_1 field inhomogeneity created by the transceiver surface RF probes. An alternative approach to conventional retrospective B_1 correction methods was implemented based on estimating the relationship between FA, SI and T_1 using empirical measurements (*model-based method*). This method was benchmarked against a well-known B_1^- correction method (*sensitivity method*). In addition, a third method was developed as a combination of both (*hybrid method*). A validation of the correction methods using qualitative and quantitative metrics on phantoms and brains—*in vivo* and *ex vivo*—was performed. The author of this thesis performed all the described tasks (except for *in vivo* animal handling).

3.1.1. B_1 field characterization

The maps of the receive field (B_1^-) (**Figure 8A**) and transmit field (B_1^+ , here as FA) relative to a 90° excitation FA (**Figure 8B**) demonstrate the spatially-varying sensitivity and FA for the ^1H -CRP. A closer look at the vertical mid-line profile reveals a strong deviation from the target of $\text{FA}=90^\circ$ (nominal FA) with increasing distance from the surface of the ^1H -CRP (**Figure 8C**). These field maps show the typical inhomogeneity inherent to transceive surface RF coils, which was very similar in the B_1^+ and B_1^- maps and FA profiles for the single loop RF coil (**Figures 8D-F**).

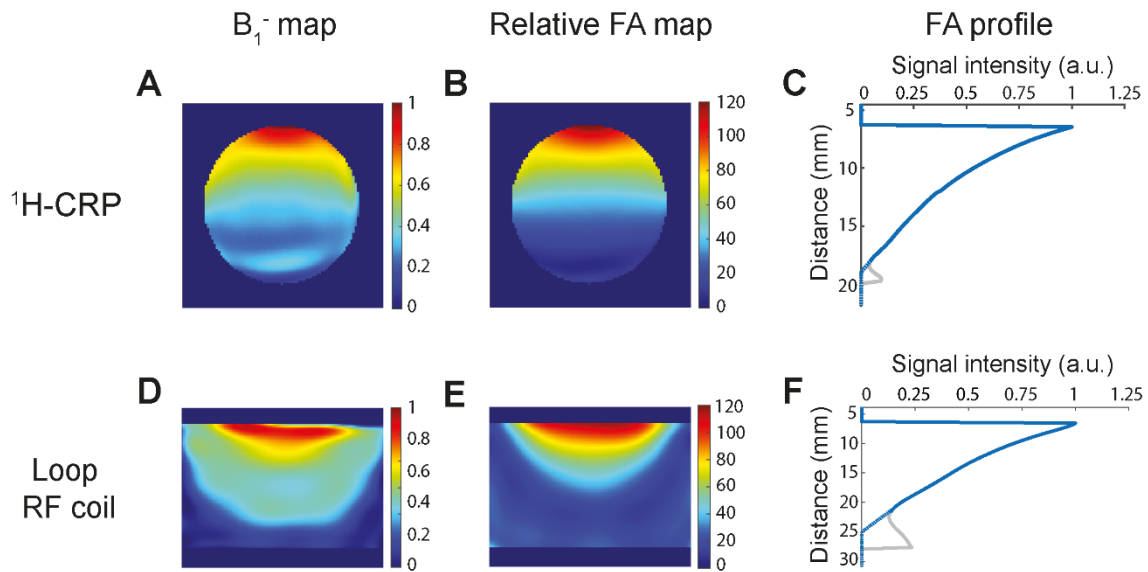


Figure 8. “Sensitivity maps and transmission fields of the two transceive (TxRx) surface RF coils used for testing and validation. (A, D) Axial view of the computed sensitivity (B_1^-) maps for a uniform phantom placed close to the RF coil surface. (B, E) Corresponding FA maps relative to a 90° excitation. (C, F) Normalized central profile plots of the FA along the vertical axis, which reveal a strong decay with increasing distance to the RF coil surfaces. The gray lines depict the true calculated data mis-estimated by the polynomial fit at low-SNR regions far away from the RF coil surface; the assumed true value is shown by the blue dotted lines” (Ramos Delgado P, Kuehne A, Periquito J, et al. 2020)

3.1.2. Empirical RARE signal intensity model

The RARE SI dependency on FA and T_1 ($SI=f(FA, T_1)$) was modelled to the experimental data acquired either incorporating a flipback pulse to restore longitudinal magnetization and hence improve SNR (**Figures 9A-C**), or excluding flipback to allow natural relaxation (**Figures 9D-F**). The fitted 3D-surfaces are shown in **Figures 9A,D**. 2D-projections of the RARE models show the relationships between SI and T_1 for several FA values (**Figures 9B,E**) and between SI and FA for several T_1 values (**Figures 9C,F**). As expected, the fitted SI data predicts lower SI with increasing T_1 and maximal SI for FAs around 90° . The surface fits modelled the experimental data well ($R^2=0.997$ in both cases).

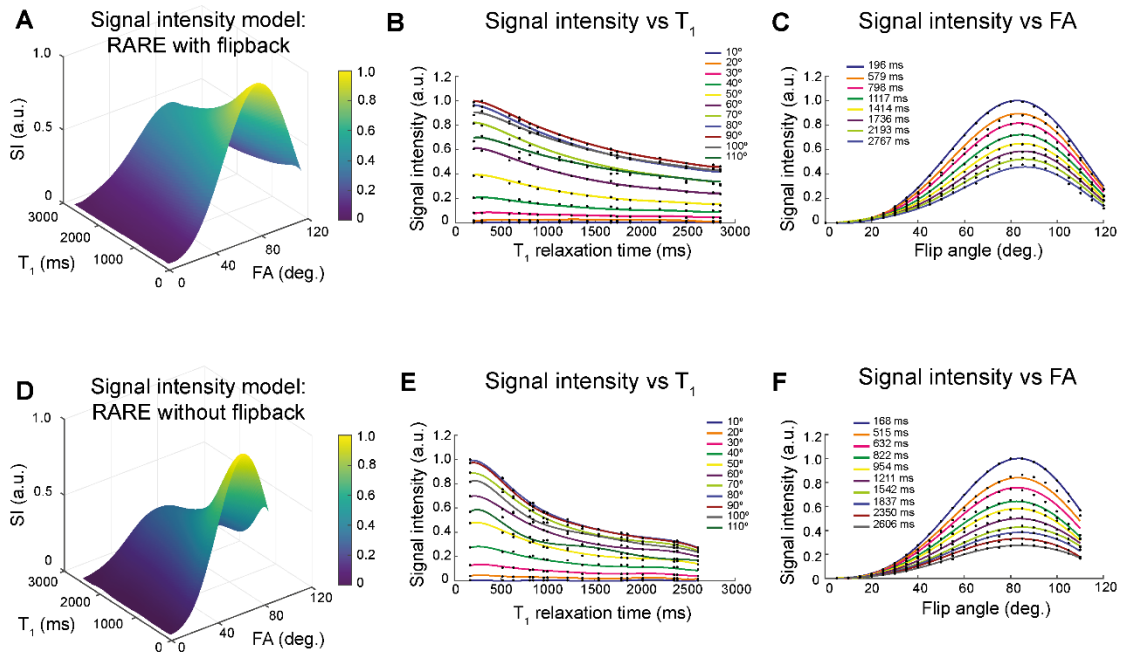


Figure 9. “Signal intensity models for RARE with and without flipback. (A, D) 3D-plots of the modelled RARE signal intensity (SI) as a function of the T_1 relaxation time and flip angle (FA) with and without flipback, respectively ($R^2=0.997$ for both). (B, E) show the SI vs FA projection in both models, whereas (C, F) depict the SI vs T_1 projection. Selected FA and T_1 values are plotted to demonstrate the fidelity of the experimental data and the model. Each colored line depicts a different T_1 and FA, respectively. The dots represent the measured data points” (Ramos Delgado P, Kuehne A, Periquito J, et al. 2020)

3.1.3. B_1 correction method validation

T_1 maps (needed for B_1^+ correction) and reference images of a uniform phantom, an *ex vivo* mouse phantom, and an *in vivo* mouse brain were acquired using a volume resonator (Figures 10A-B). The original uncorrected $^1\text{H-CRP}$ images show the strong spatial SI gradient typical of transceive surface RF coils (Figure 10C). The results obtained with the three B_1 correction methods are shown in Figure 10D-F. The strong spatial SI gradient present in the $^1\text{H-CRP}$ images was removed by all B_1 correction methods, yielding a uniform SI throughout the entire field of view for all investigated samples, including the *in vivo* mouse head. With the *sensitivity* and *model-based corrections* an overshoot in SI in some regions was observed, particularly distal to the CRP. This was due to a combination of increasing inaccuracies in the FA and SI data at low SNR. This overshoot in SI was resolved by combining both methods in the *hybrid correction* approach.

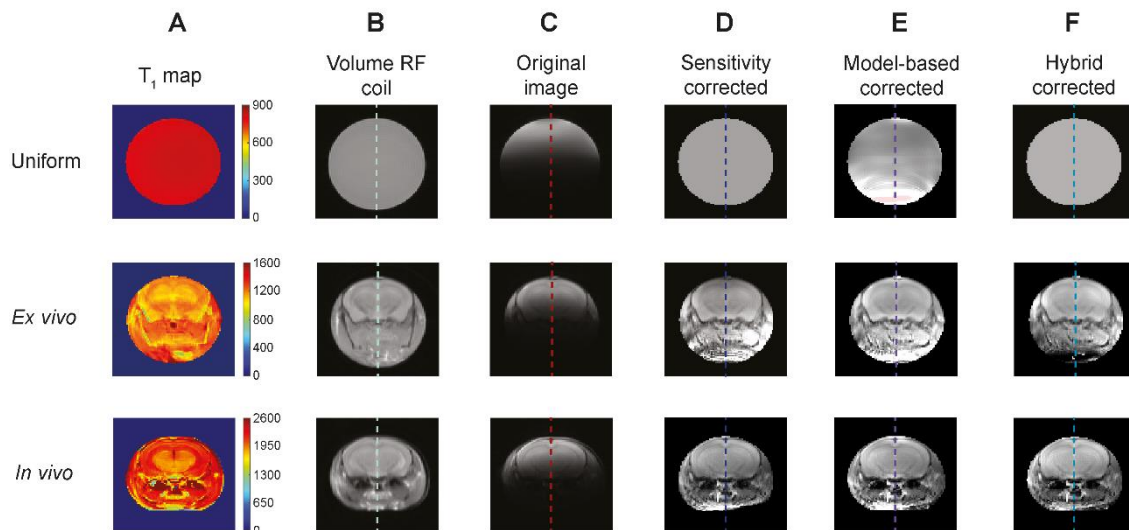


Figure 10. “**B₁ correction for CRP images of a uniform phantom, an *ex vivo* phantom and a living mouse.** From left to right, the columns show **(A)** the acquired T₁ map (reference coil), **(B)** the reference image, **(C)** the original CRP image, **(D-F)** the corrected images. A comparison of the original images with the reference images demonstrates the need of B₁ correction. Quantification is severely hampered by the adverse signal intensity gradient. The corrected images show a remarkably improved homogeneity. All three B₁ correction methods performed well, with only slight differences between the results. Masks containing minor errors in the correction are overlaid and shown in light red” (Ramos Delgado P, Kuehne A, Periquito J, et al. 2020)

Central profile plots (¹H-CRP). To quantitatively assess the correction of the image inhomogeneity, normalized vertical SI profiles were plotted (**Figure 11A-C**). For all three approaches, the corrected SI profiles showed close correspondence with the reference RF coil (plotted as a surface in green). From these profiles, one can determine how far away from the RF coil it is still viable to perform B₁ correction. This depends on the specific scanning parameters and the dimensions of the RF coil; here this distance was approximately 17 mm (for a nominal FA=90°, an actual FA≥8° could be corrected). For our experimental setup, the region beyond 17 mm showed increasing inaccuracies in the field maps and SI measurements, leading to unacceptable errors in all corrected images.

Quantitative examination revealed that all correction methods considerably reduced the RMSE computed on the profiles to a maximum of 0.18 (uniform), 0.12 (*ex vivo*) and 0.26 (*in vivo*), with respect to the reference. For the uniform phantom, the *sensitivity* and *hybrid approaches* performed equally well (0.11).

For the *ex vivo* phantom the *sensitivity* and *model-based correction* performed similarly (0.11). *In vivo*, the *sensitivity correction* achieved the best result (0.21). In comparison, the uncorrected profiles revealed an average RMSE of 0.53 ± 0.07 for all test phantoms.

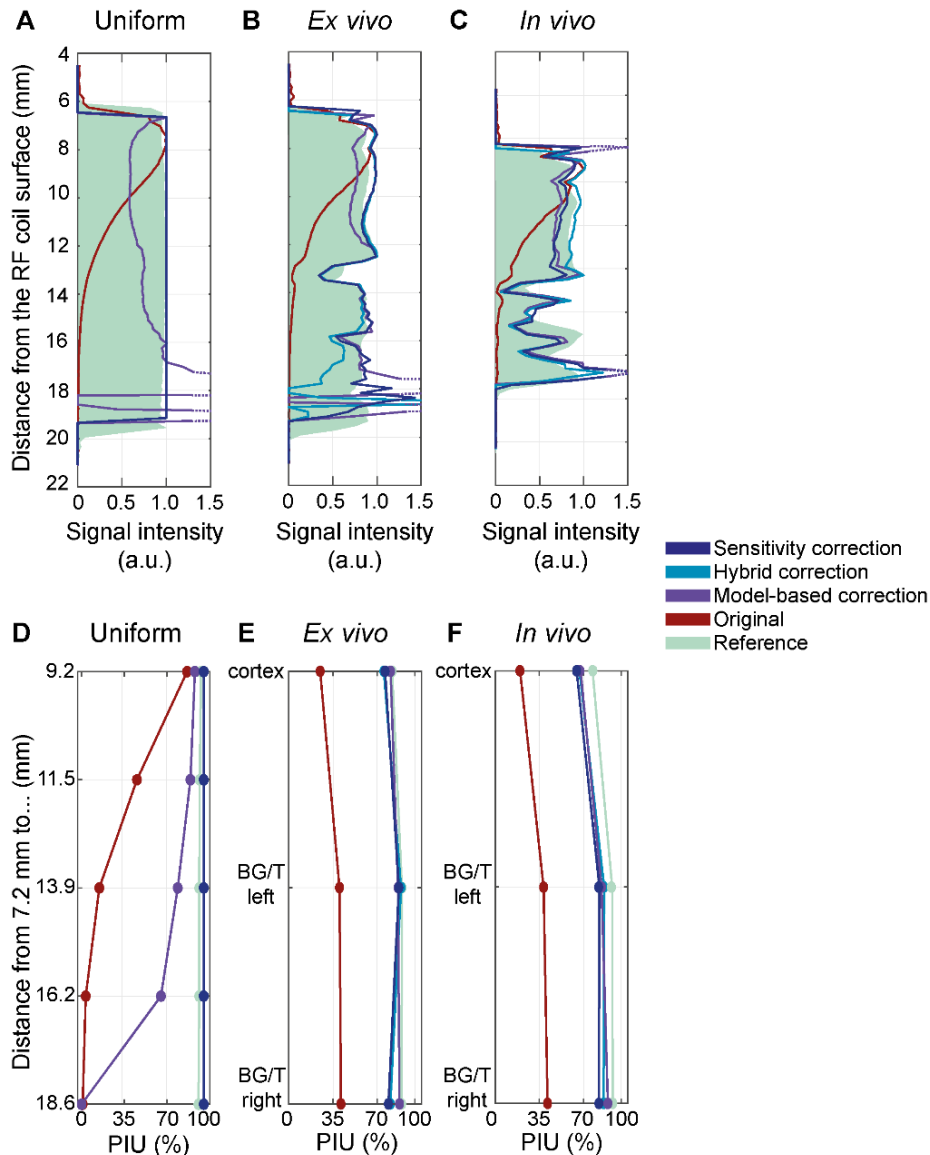


Figure 11. “Normalized signal intensity profiles perpendicular to the RF coil surface and percentage image uniformities (PIU) for the exemplary images shown in Figure 5: (A-D) uniform phantom, (B-E) *ex vivo*, and (C-F) *in vivo*, using five internally-tangent circular ROIs with increasing diameter (uniform) or anatomical regions (*ex vivo*, *in vivo*: cortex and basal ganglia/thalamus, BG/T). The corrected profiles demonstrate a striking increase in image homogeneity and show the same trends as those of the reference coil. In all three phantoms the calculated RMSEs of the corrected profiles reveal a high resemblance to the reference. The PIU plots indicate a significant improvement in image homogeneity after correction” (Ramos Delgado P, Kuehne A, Periquito J, et al. 2020)

Image homogeneity assessment (¹H-CRP). For the uniform phantom, the calculated *percentage integral uniformity* (PIU) (**Figure 11D-F**) was found to be 95.7% within the largest ROI using the volume resonator, indicating no significant inhomogeneities across the image, as expected. Conversely, a PIU of 0.9% was obtained within the same ROI on the uncorrected image. The PIU degradation scaled with increasing ROI diameter. After correction, the *model-based approach* showed a PIU of 65% on the fourth ROI (up to a distance of 16.2 mm from the RF coil surface). Beyond that distance, the observed overshoots confounded the PIU, which decreased to 0% in the largest ROI.

For the mouse brain images, the PIUs showed the expected high homogeneity for the reference RF coil: *ex vivo* 87.0±4.4% and *in vivo* 87.7±9.1%. The original surface RF coil images displayed substantial inhomogeneities: averages of 35.4±9.2% *ex vivo* and 33.2±11.8% *in vivo*. A significant improvement in image homogeneity was achieved with the three correction methods, both *in vivo* and *ex vivo*. The *model-based method* performed best on average (85.0±3.8% *ex vivo* and 80.5±11.3% *in vivo*), closely followed by the *hybrid* (81.6±6.9% *ex vivo* and 79.7±11.2% *in vivo*) and *sensitivity* (80.8±5.7% *ex vivo* and 76.5±10.3% *in vivo*) corrections.

T₁-contrast and quantification performance (RT). The errors in SI ratios between several fixed locations for all four phantoms were studied, comparing original (uncorrected) RARE images and their three corrections, relative to the ground truth (reference images). These validation assessments were performed for RARE without flipback (**Figure 12**) and with flipback (**Figure 13**). The box plots (whiskers at 5-95 percentile) depict the mean errors for quantification at low and high T₁ relaxation times, and for T₁ contrast measurements with low and high proton density. Errors below 10% (dashed line) were considered acceptable.

Correction of RARE MR images without flipback (Figure 12): All correction methods reduced the errors to less than 10% for both quantification and contrast, contrary to uncorrected images, which showed substantial errors (41-45%), and variabilities (37-42%). None of the calculated mean errors reached a value >8.3% after correction.

The *sensitivity correction* performed best when calculating water content proportions at low T_1 values ($5.0 \pm 2.9\%$), followed closely by the *hybrid* ($6.0 \pm 2.7\%$) and *model-based* ($6.6 \pm 4.5\%$) methods. All three methods behaved similarly for higher T_1 values, with mean errors of approximately 8% (*sensitivity* $8.1 \pm 2.9\%$, *model-based* $8.3 \pm 5.9\%$, *hybrid* $8.1 \pm 3.3\%$). All correction methods improved quantification significantly (p -value <0.0001) when compared to the original data.

When measuring T_1 contrast, the *hybrid method* performed best for both water content phantoms ($2.4 \pm 1.7\%$ high, $4.7 \pm 3.8\%$ low). The *sensitivity correction* method performed better than the *model-based method* for the high water content phantom ($3.5 \pm 2.5\%$ vs. $6.2 \pm 5.5\%$). However, for the low water content comparison, the *model-based correction* method performed better than the *sensitivity correction* ($5.2 \pm 3.9\%$ vs. $6.1 \pm 3.1\%$). Similarly, the three described correction methods significantly improved T_1 contrast, when compared to the original data (p -value <0.0001).

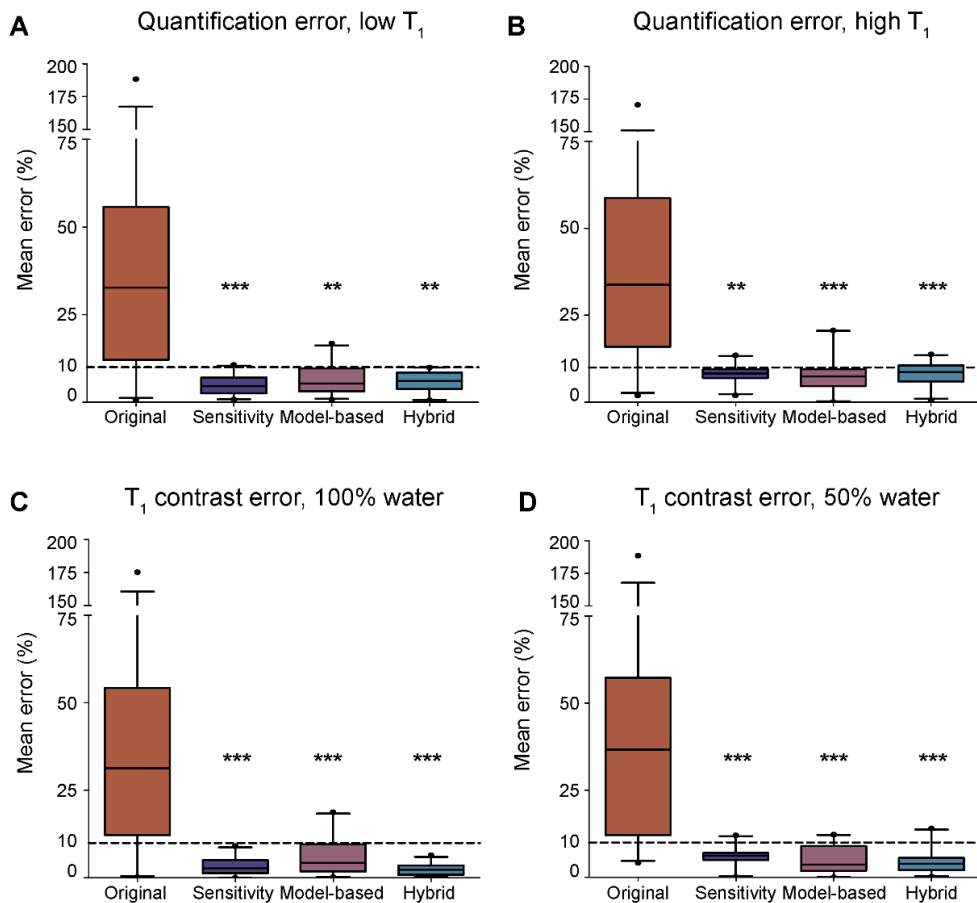


Figure 12. “Assessment of quantification and contrast accuracy for RARE without flipback. Box plot of relative quantification and contrast errors for the original uncorrected

images and those corrected with each of the three B₁ correction methods. All B₁ correction methods reduced the median error from well above 25% to below 10% (dashed line). Whiskers represent the 5 and 95 percentiles. Asterisks indicate statistically significant differences compared to the uncorrected images” (Ramos Delgado P, Kuehne A, Periquito J, et al. 2020)

Correction of RARE MR images with flipback (Figure 13): In general, all correction methods performed worse when flipback was enabled in RARE measurements, compared to RARE without flipback. The errors without correction were comparable to the case without the flipback option (40-58%). Their variabilities, however, were spread along a wider range (40-62%).

For quantification, the correction methods performed worse at low T₁ relaxation times (overall about 10%: *sensitivity* 11.0±7.6%, *model-based* 10.7±7.9%, *hybrid* 12.2±8.6%) than at higher ones (*sensitivity* 4.8±4.0%, *model-based* 11.4±10.1%, *hybrid* 7.2±6.0%). All correction methods significantly improved quantification when compared to the original data (*p*-value<0.0001).

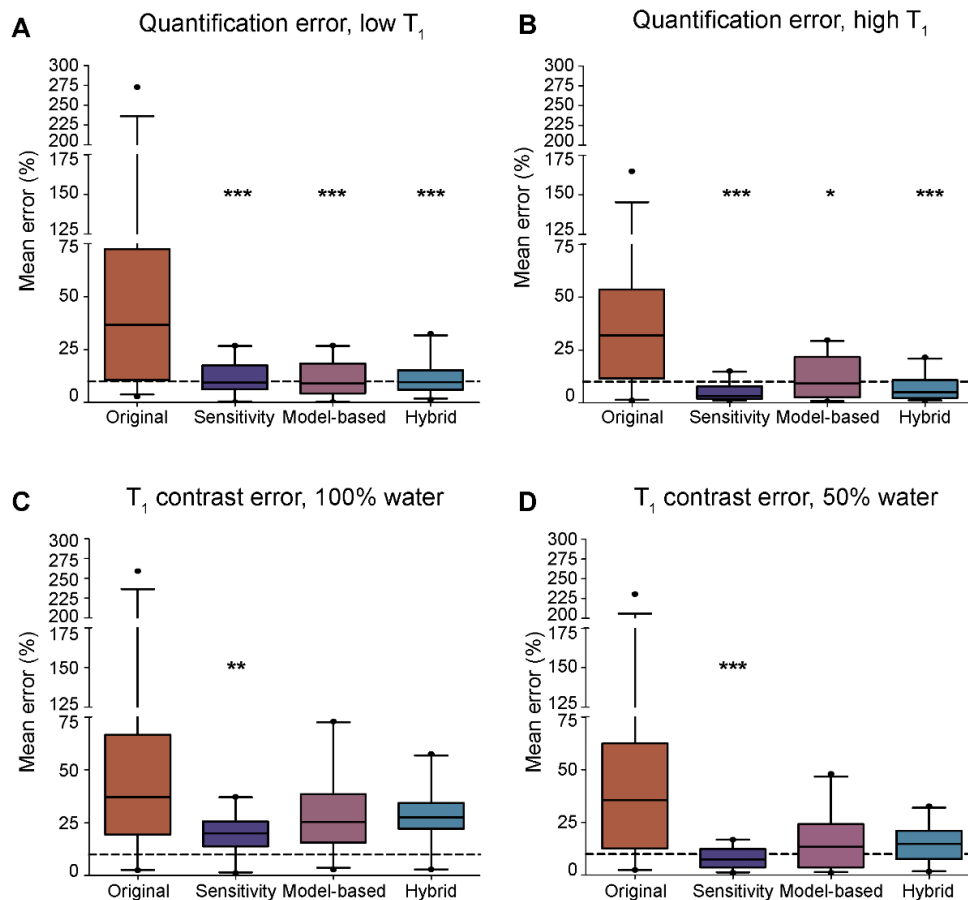


Figure 13. “Assessment of quantification and contrast accuracy for RARE with active flipback. Box plot of relative quantification and contrast errors for the original uncorrected images and those corrected with each of the three B₁ correction methods. B₁ correction reduced

the median quantification error from well above 25% to below 10% (dashed line), but achieved only a modest improvement in the T₁ contrast error. Whiskers represent the 5 and 95 percentiles. Asterisks indicate statistically significant differences compared to the uncorrected images” (Ramos Delgado P, Kuehne A, Periquito J, et al. 2020)

T₁ contrast accuracy was considerably reduced when using flipback during the measurements, with errors approaching 20-30% for high water content. The *sensitivity correction* method (19.5±9.7%) performed marginally better than the *model-based* (28.9±19.4%) and *hybrid* (28.4±14.5%) methods. For higher water content, the errors were smaller (8-15%). Similarly, the *sensitivity correction* method (8.3±5.0%) performed slightly better than the other two (*model-based* 15.2±13.2%, *hybrid* 15.2±8.7%). Only the *sensitivity method* significantly improved T₁ contrast (*p*-value=0.0002 and 0.0003 for high and low proton density, respectively).

3.2. B_1 inhomogeneity correction at low SNR: first quantitative *in vivo* ^{19}F -MRI of mouse brain inflammation using a transceive surface RF probe

This chapter contains and uses results that have been published by the author of this thesis:

Ramos Delgado P, Kuehne A, Aravina M, Millward JM, Vazquez A, Starke L, Waiczies H, Pohlmann A, Niendorf T, Waiczies S. *B_1 Inhomogeneity Correction of RARE MRI at Low SNR: Quantitative In Vivo ^{19}F -MRI of Mouse Neuroinflammation with a Cryogenically-cooled Transceive Surface Radiofrequency Probe*. *Magnetic Resonance in Medicine*, 2021; 87(4):1952-1970. DOI: 10.1002/mrm.29094

and therefore contains text, statements, passages and figures from this publication.

In the previous chapter, three B_1 correction methods were developed and validated on ^1H -MRI to correct for the B_1 field inhomogeneities inherent to sensitivity-boosting transceiver surface RF probes and enable signal quantification. This chapter builds upon previous findings in order to correct ^{19}F -MR brain images acquired with a ^{19}F -CRP in mice with experimental autoimmune encephalomyelitis and to determine brain inflammation. Unlike ^1H -MRI, ^{19}F imaging suffers from low SNR, leading to long scan times. Therefore, the use of SNR-enhancing technologies such as transceiver surface RF probes (with or without cryo-cooling) is even more indispensable. To obtain higher SNR gains, quadrature RF coil designs are chosen over linear implementations, but this leads to single-tuned characteristics. The missing ^1H -MRI capability of this RF technology requires the establishment of a workflow, in which *in vivo* ^{19}F -MR images can be co-localized onto anatomical images. The previously introduced retrospective B_1 correction methods were implemented in this study and validated for a ^{19}F -CRP using a uniform phantom and inflamed mouse brains—*ex vivo* and *in vivo*. Additionally, computations of concentration uncertainty maps using Monte Carlo SNR simulations were introduced to demonstrate the markedly improved ^{19}F quantification of B_1 -corrected images, as well as to propose SNR requirements to achieve acceptable error levels. The author of this thesis performed all the described tasks (except for *in vivo* animal handling, head holder design and reference cap building).

3.2.1. B_1 field characterization and simulated RARE signal intensity model

The sensitivity maps (**Figure 14A,D**) and the FA maps (relative to an excitation $FA=90^\circ$, **Figure 14B,E**) of the ^{19}F -CRP revealed a strong decline with increasing distance from the RF probe surface, in both axial and sagittal orientations.

The B_1^+ inhomogeneity is clearly depicted in **Figures 14C** (axial) and **14F** (sagittal) which show the normalized central vertical profile lines. The maximum distance until which there is signal above the detection threshold ($\text{SNR}>3.5$) is, in this case, ca. 14.6 mm from the ^{19}F -CRP surface. **Figure 14G** shows the 3D view of the RARE SI model simulated using EPG simulations. The SI was modelled as a function of FA and T_1 . The SI demonstrates a lower SI with increasing T_1 (**Figure 14H**) and maximal SI for $FA=90^\circ$ (**Figure 14I**). When using EPG simulations, the *hybrid* and *sensitivity methods* yielded the same results up to a constant factor. Therefore, only the *sensitivity* and *model-based correction* were used moving forward.

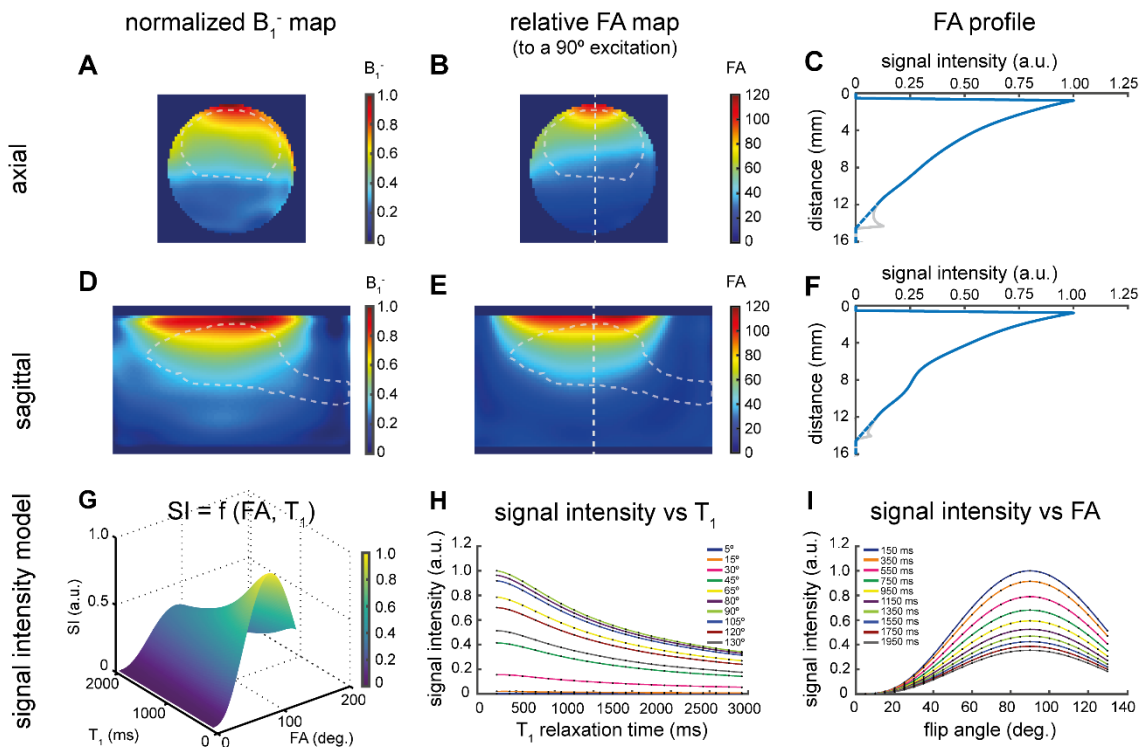


Figure 14. “ B_1 field maps of the quadrature ^{19}F cryogenically-cooled transceive surface RF probe (^{19}F -CRP) and SI model used. B_1^+ and relative FA maps to a 90° excitation FA in (A-B) axial and (D-E) sagittal orientation. The expected position of the mouse brain relative to the ^{19}F -CRP is outlined as a dashed grey line. Corresponding normalized central vertical profiles are shown in (C,F). The grey line depicts the artefact miscalculated by the polynomial fit at low-

SNR regions far away from the RF probe surface. The physically-correct value is depicted using blue dotted lines. The simulated 3D SI model (**G**) shows the dependency of RARE's SI on the T_1 relaxation time and FA. (**H,I**) show the 2D-projections of SI vs T_1 and SI vs FA, respectively” (Ramos Delgado P, Kuehne A, Aravina M, et al. 2021)

3.2.2. T_1 relaxation time estimation

Calculated T_1 values for PFCE-NPs in agarose (reference caps, 935.9 ± 10.0 ms) using non-localized MRS agreed with previously published values at 9.4 T.^{72,73} T_1 values of ^{19}F -NPs in inflammatory lesions in the brain (PRESS) were 818.1 ± 13.4 ms (*ex vivo*) and 1868.7 ± 43.9 ms (*in vivo*). This indicated an effective reduction of 117.8 ms in T_1 for *ex vivo* compared to the reference caps, and an increase of nearly 1 second in T_1 *in vivo* measurements.

Exemplary spectra used to compute T_1 values in reference caps, *ex vivo* and *in vivo* mice are showed in **Figure 15**.

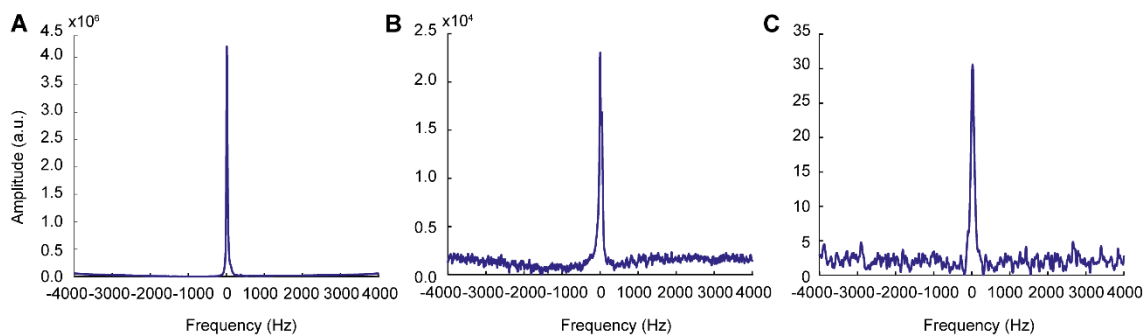


Figure 15. “Exemplary spectra used for T_1 calculation for (A) reference cap containing 24mM ^{19}F -loaded NPs (non-localized spectroscopy), (B) *ex vivo* CNS of an EAE mouse with administered ^{19}F -loaded NPs prior to perfusion (PRESS), and (C) *in vivo* mouse with active EAE and administered ^{19}F -loaded NPs (PRESS). Measurements were performed using a $^1\text{H}/^{19}\text{F}$ volume resonator. Selected TR=10000 ms” (Ramos Delgado P, Kuehne A, Aravina M, et al. 2021)

3.2.3. Monte Carlo SNR simulations to estimate the ^{19}F concentration uncertainty

Figures 16A-C show the concentration uncertainty (uncertainty= $\text{SD} \times 100$ (%)) for all FAs/ B_1^- and three SNR values fixed for FA= 90° , B_1^- =1 and T_1 =1869 ms (*in vivo*). For the reference, representative values (FA= 60° , B_1^- =0.8) were used. The level of uncertainty increases with decreasing FAs and B_1^- . This trend is more pronounced for regions farther away from the RF probe surface. The

contour lines represent SNR values. The green and red isolines depict the border of the regions where uncertainty $\leq 10\%$ and $\leq 25\%$, respectively. These borders occur at $\text{SNR} \approx 10.1$ and $\text{SNR} \approx 4.25$, respectively, independent of the FA/B_1^- and SNR combination.

The linear dependence of the SD of both corrected SI and concentration on SNR for exemplary data ($\text{FA}=90^\circ$, $B_1^- = 1.0$, *in vivo* T_1) using the *model-based method* (**Figure 16D**, linear fit, dashed orange line) was studied. The corrected SI of the sample (blue dots) demonstrated a linear trend throughout the SNR range. The concentration SD (green boxes) was linearly dependent on the sample SNR until an $\text{SNR} \approx 160$ ($\text{SD} = 7 \times 10^{-3}$), after which it asymptotically approached a constant value of approximately 3.5×10^{-3} (uncertainty = 0.35%) due to small but non-negligible errors in the B_1^- -corrected data.

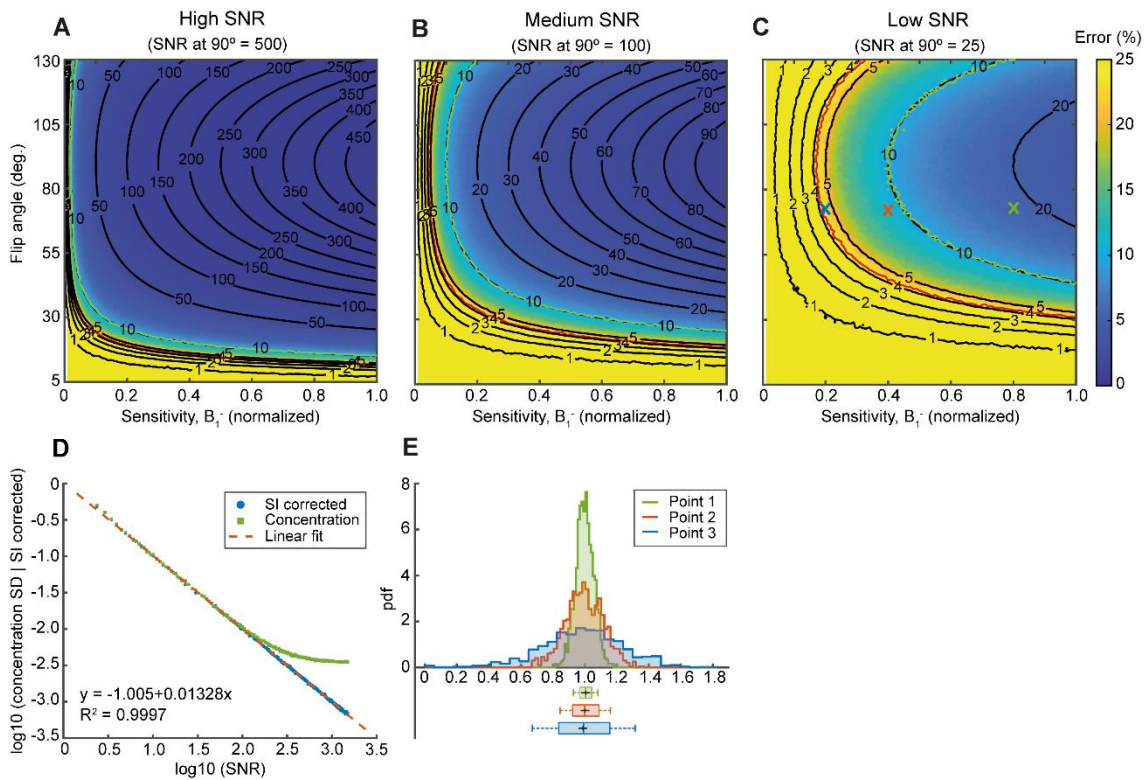


Figure 16. “SNR simulation results corresponding to a *model-based* correction for $T_1=1869$ ms (in vivo mouse) for (A) $\text{SNR}=1000$, (B) $\text{SNR}=500$, and (C) $\text{SNR}=25$, fixed for a 90° excitation and $B_1^- = 1$. The contour lines represent equal SNR values (in black), and errors of $\leq 10\%$ (in green) and $\leq 25\%$ (in red). (D) shows the linear dependence on the SD of the corrected SI and SNR, and the quasi-linear dependence on the SD of the concentration and SNR (log-log plot). A histogram from the Monte Carlo samples for the three points depicted in (C) is illustrated in (E). In all three cases, the distributions exhibit a Gaussian distribution of mean ≈ 1 and

increasing SDs (uncertainties) with decreasing SNR” (Ramos Delgado P, Kuehne A, Aravina M, et al. 2021)

Finally, **Figure 16E** shows histograms and error bars⁷⁴ of the concentration calculated over the 1000 iterations corresponding to the three depicted example points (FA=70°, B₁=0.8/0.4/0.2 as coloured crosses on **Figure 16C**). The concentration samples exhibited a Gaussian shape with mean≈1 (μ₁=1.0003, μ₂=0.9964, μ₃=0.9834) and increasing SD (σ₁=0.0564, σ₂=0.1199, σ₃=0.2529) with decreasing SNR, as expected. This demonstrated that the model recovered SIs without introducing bias. Randomness was propagated such that the variability of the corrected SI (i.e. its SD) increased with decreasing SNR.

3.2.4. B₁ correction method validation

Corrected Images. B₁ correction performance was assessed in a low-SNR scenario at regions far from the probe surface using a low-concentration uniform phantom and a short acquisition. The SNR map is shown in **Figure 17A**. The original image shows a steep SI decay away from the RF probe surface, typical of transceive surface RF coils (**Figure 17B**). Compared to the reference image, B₁-corrected images (**Figure 17C-D**) yielded uniform SIs over the FOV (**Figure 17E**). A ghosting artefact due to fast RARE imaging is present in the uniform phantom image used for the *sensitivity method*, and in the test uniform phantom, producing an overshoot in the *sensitivity-corrected* image far from the probe surface.

Central profile plots (Figure 17F). Corrected SI profiles demonstrated close correspondence with the reference RF coil (green area) up to a distance of approximately 6-7 mm from the CRP surface for our specific scanning parameters, dimensions of the RF coil and SNR.

Image homogeneity assessment (Figure 17H). The calculated PIU in the reference image was 91.4% within the largest ROI (distance from CRP surface=7.8 mm), indicating no substantial inhomogeneities across the image. In contrast, a PIU of 13.6% was computed for the original image within the same ROI. Corrections yielded improved PIUs (56.7% for *model-based* and 32.4% for *sensitivity corrections*). In general, PIU degrades with increasing distance from the RF probe where acquired image artefacts prevail.

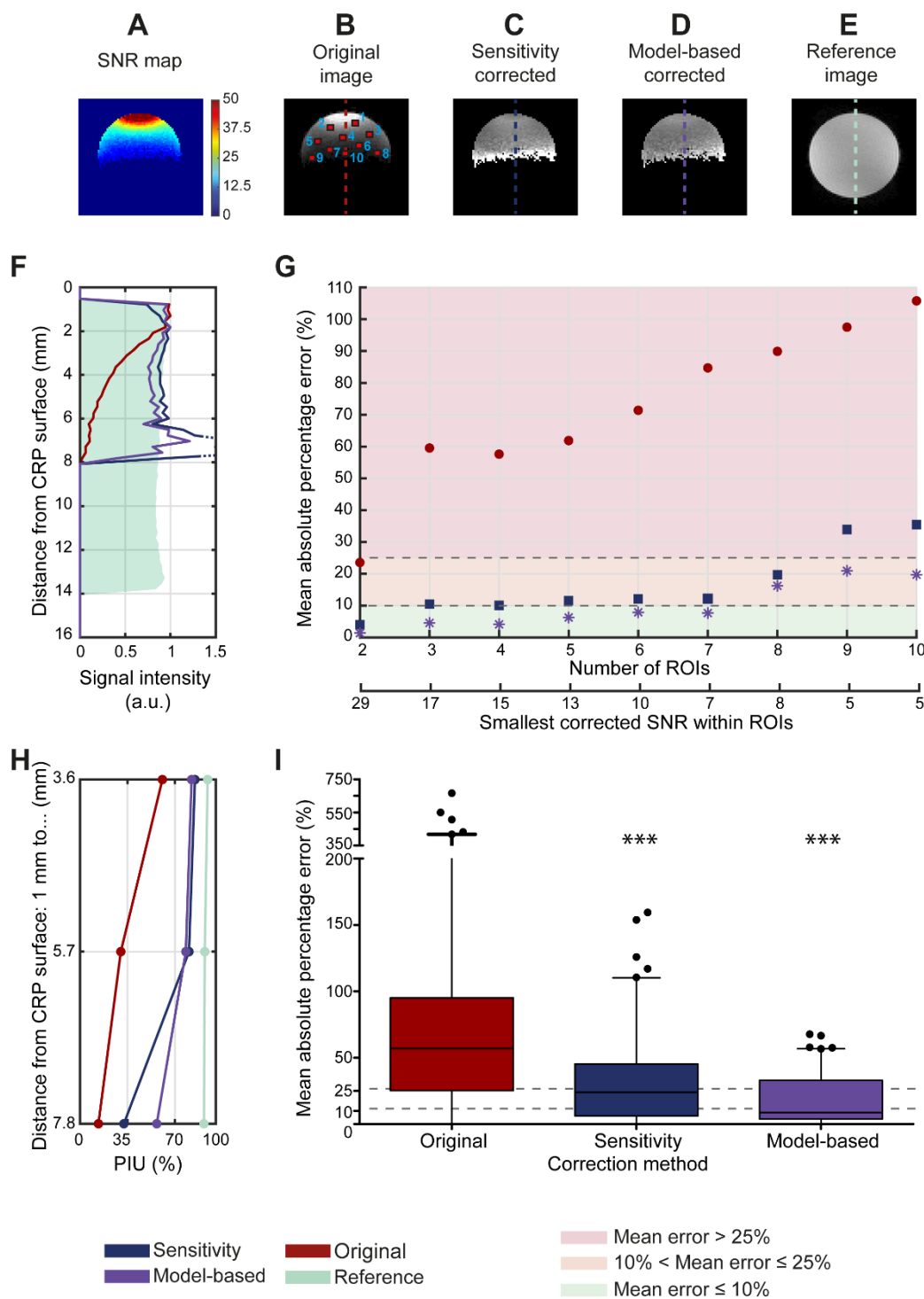


Figure 17. “Uniform phantom validation. (A) SNR map, **(B)** original, **(C-D)** corrected and **(E)** reference images, respectively. The original image includes the placement of the 10 ROIs selected for error calculations. **(F)** Normalized signal intensity profiles perpendicular to the RF coil surface. **(G)** Mean absolute percentage error (MAPE) of original and corrected images for an increasing number of ROIs demonstrates a remarkable reduction in errors after B_1 correction compared to original images. The *model-based correction* provides quantitatively good results

in regions far from the RF probe. **(H)** Percentage of integral uniformity (PIU) of corrected images show a quantitative improvement in homogeneity in comparison with original images. **(I)** Statistical assessment of signal intensity accuracy. Whiskers represent the 5 and 95 percentiles. Asterisks indicate statistical significance compared to uncorrected images” (Ramos Delgado P, Kuehne A, Aravina M, et al. 2021)

Quantification performance and statistics. According to our MAPE classification, only the *model-based correction* provided excellent results for SNRs between 38 and 7 (**Figure 17G**, ROIs=1-7, distance=2.1-6.3 mm). Uncorrected images showed high errors within this SNR range ($84.7\pm 85.8\%$). Within this region (distance=2.1-6.3 mm), the *model-based correction* performed best ($7.7\pm 4.7\%$), followed by the *sensitivity correction* which yielded good results ($12.2\pm 8.2\%$). Both corrections provided equally good results (*model-based* $16.2\pm 16.5\%$, *sensitivity* $19.7\pm 16.6\%$) up to the 8th ROI (distance=2.1-6.5 mm), in contrast to uncorrected images ($89.9\pm 95.6\%$). When considering all ROIs (distance=2.1-7.6 mm), only the *model-based correction* ($19.7\pm 18.9\%$) yielded good results. In this case, the *sensitivity correction* provided unacceptable results ($35.5\pm 33.3\%$), but was still lower than the MAPE of uncorrected images ($105.8\pm 125.9\%$). **Figure 17G** also shows similarities between the proposed ranges using simulations (uncertainty $\leq 10\%$ when $\text{SNR}\geq 10.1$ and uncertainty $\leq 25\%$ when $\text{SNR}\geq 4.25$) and experimental results.

The *model-based correction* performed best overall, significantly reducing quantification errors compared to original mean errors (both B₁ correction methods $p\text{-value}<0.001$, **Figure 17I**). Therefore, this method was used for further B₁ corrections.

Ex vivo MR measurements. **Figures 18** and **19** show the results for axial and sagittal orientations, respectively.

Concentration maps of the *ex vivo* EAE phantom were computed for different measurement times (15 minutes [NEX=300], 1, 3 and 6 hours [NEX=1200/3600/7200]) using the 24mM-reference cap in images acquired with the reference volume resonator (**Figures 18A, 19A**) and original ¹⁹F-CRP images (**Figures 18B, 19B**). Qualitative comparison of the reference images after 3 hours and original CRP images after 15 minutes revealed distinct similarities, demonstrating the remarkable SNR capabilities of the CRP. However, the ¹⁹F

signal at the lymph nodes, indicating accumulation of ^{19}F -labeled inflammatory cells (white arrows) in reference images was absent in the ^{19}F -CRP images.

Assessment of the ^{19}F concentration shown by original CRP images and corresponding *model-based B_1 -corrected* images (**Figures 18D, 19D**) demonstrated that correction considerably improved the concentration estimation, compared to reference images (ground truth). SNR maps from original CRP images showed the expected increase of SNR with scan time (**Figures 18C, 19C**), translating to fewer uncertainties in concentration (**Figures 18E, 19E**). Overall, the uncertainty maps indicated the reliability of the B_1 -corrected concentration maps, with most pixels being green (uncertainty \leq 10%) or orange (10% $<$ uncertainty \leq 25%).

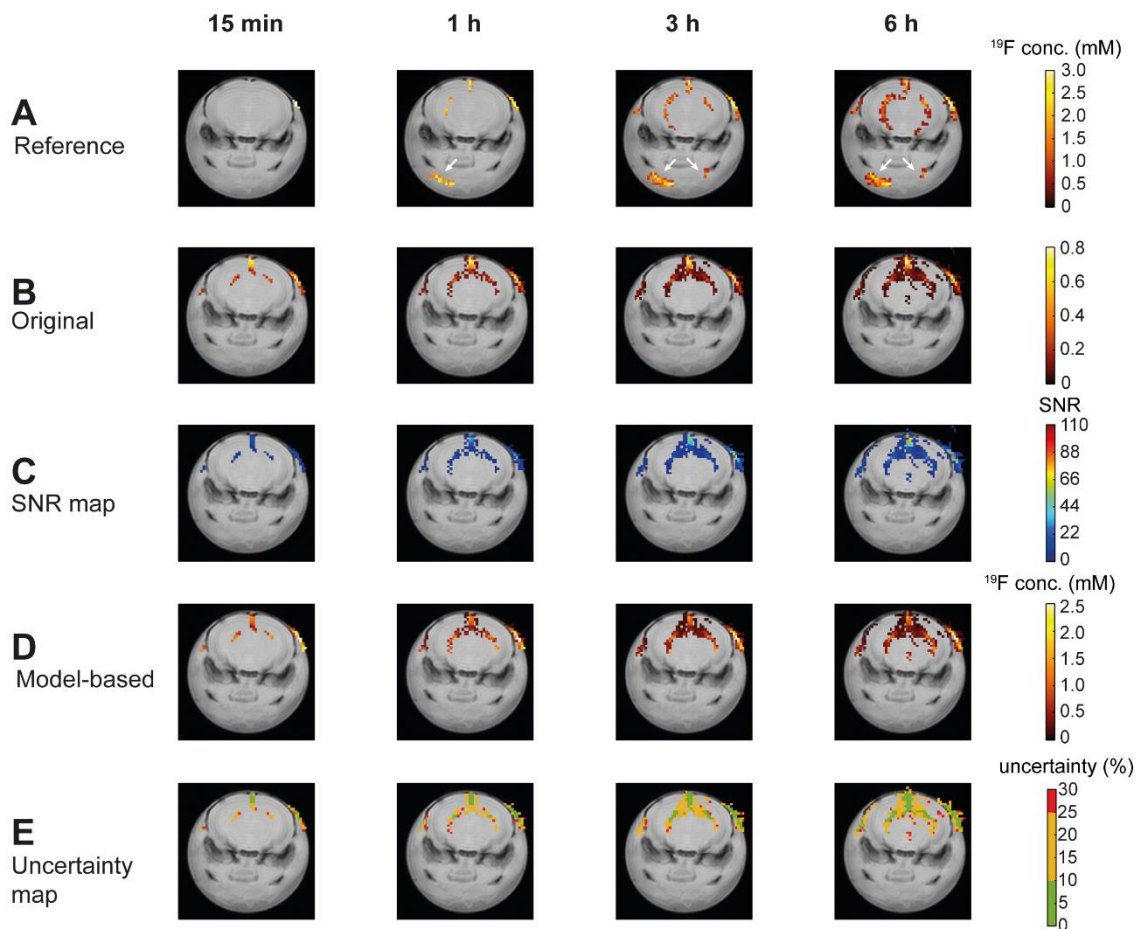


Figure 18. “*Ex vivo* phantom (score=2.0) in axial orientation for increasing scan times (15 minutes, 1 hour, 3 hours and 6 hours). Reference images (**A**) acquired with the $^1\text{H}/^{19}\text{F}$ volume resonator show less ^{19}F signal in the brain compared to ^{19}F -CRP images (**B**). The steep gradient in B_1 field of the ^{19}F -CRP prevents from detecting the prominent lymph node signals in contrast to the volume resonator. SNR maps for the CRP images are presented in (**C**). B_1 -corrected images show concentration values closer to the reference obtained with the volume

resonator **(D)**. Uncertainty maps **(E)** reveal the reliability of the B₁-corrected concentration maps, with most pixels indicating green (uncertainty≤10%) and orange (10%<uncertainty≤25%) values” (Ramos Delgado P, Kuehne A, Aravina M, et al. 2021)

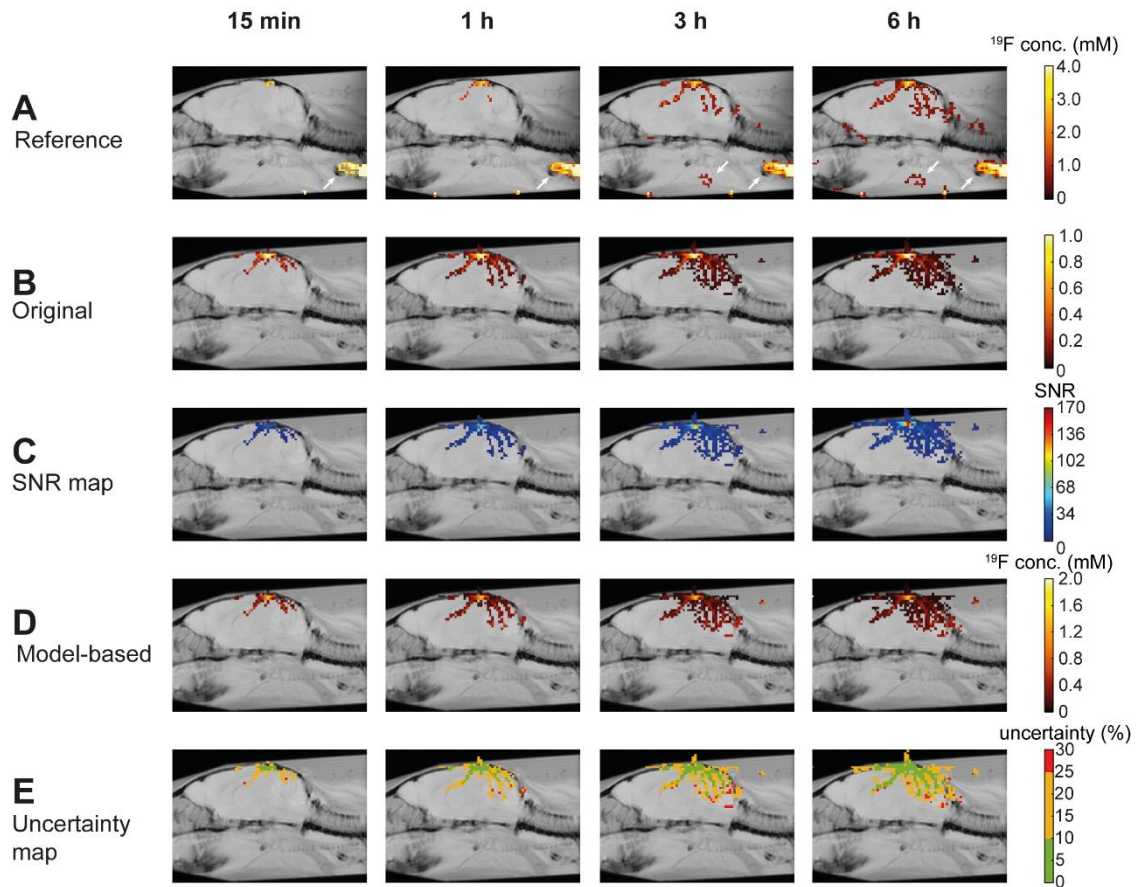


Figure 19. "Ex vivo phantom (score=2.0) in sagittal orientation for increasing scan times (15 minutes, 1 hour, 3 hours and 6 hours). Reference images **(A)** show impressive ¹⁹F signal in the lymph nodes, not visible with the ¹⁹F-CRP **(B)**, since they are located too far away from the CRP surface to be detected. Distinct similarities when comparing CRP images after 15 minutes and those acquired with the volume resonator after 3 hours demonstrate the remarkable SNR capabilities of the CRP. SNR maps for the CRP images are presented in **(C)**. After performing the B₁ correction **(D)**, images show concentration values closer to the reference obtained with the volume resonator. Uncertainty maps **(E)** reveal the reliability of the B₁-corrected concentration maps, with most pixels indicating green (uncertainty≤10%) and orange (10%<uncertainty≤25%) values” (Ramos Delgado P, Kuehne A, Aravina M, et al. 2021)

In vivo MR measurements. The performance of the *model-based correction* in a typically time-constrained and low-SNR *in vivo* EAE ¹⁹F-MRI experiment was studied.

The first animal shown (**Figures 20 and 21**, axial and sagittal orientations, respectively) exhibited severe clinical symptoms (score=2.5) whereas the

second (**Figure 22** and **23**, axial and sagittal orientations, respectively) presented moderate clinical symptoms (score=1.5). Images were acquired in axial and sagittal orientations for 15, 30 and 45 minutes [NEX=300/600/900].

Concentration maps of uncorrected images of mouse 1 (**Figures 20A, 21A**) showed an overestimation of ^{19}F concentrations in regions close to the RF probe surface, which correspond to meningeal inflammatory cell infiltration, common in EAE. White arrows indicate external signals (i.e. in ears and other adjacent tissues), which are not corrected when located outside of the FA/B $_1$ maps. SNR maps (**Figures 20B, 21B**) correlate with the original concentration maps.

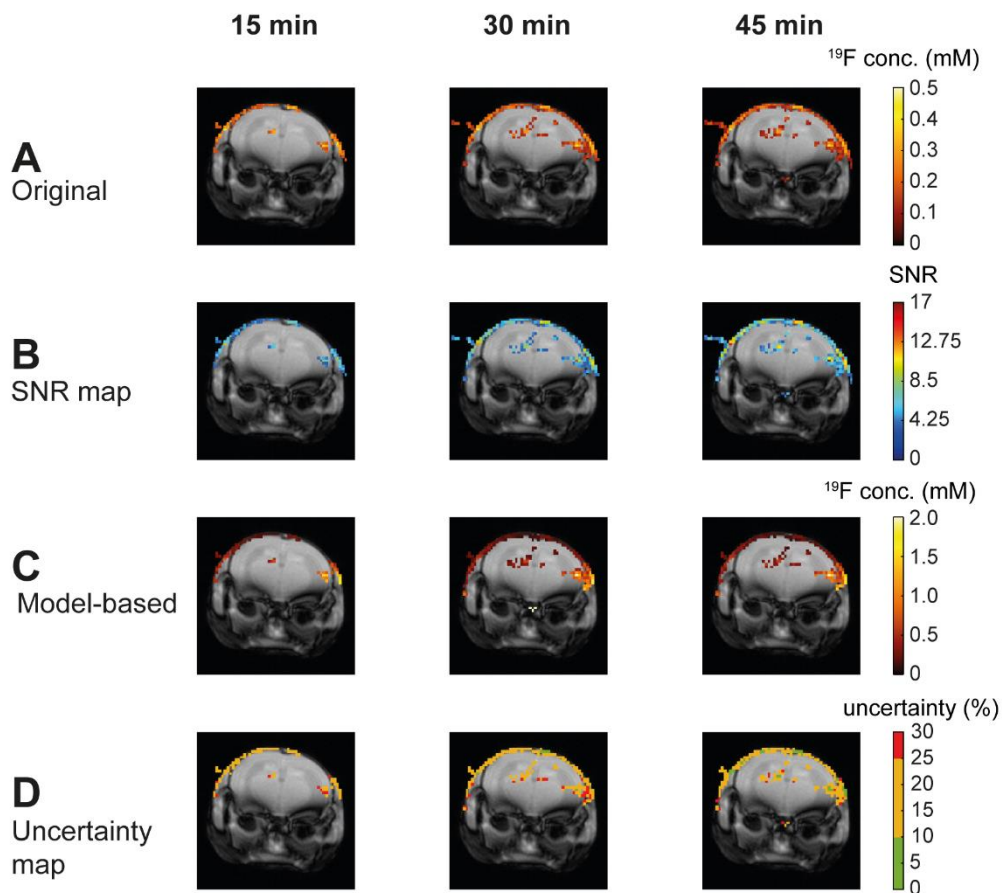


Figure 20. “*In vivo* EAE mouse 1 (score=2.5) in axial orientation. Concentration maps of original images (**A**) show an initial overestimation of the ^{19}F concentration in regions close to the RF probe surface (e.g. meninges) which partly correspond with regions with high SNR (**B**). After performing the *model-based B $_1$ correction* (**C**), ^{19}F concentration maps are computed. Their reliability is presented by the uncertainty maps (**D**) which show green (uncertainty \leq 10%) and orange (10%<uncertainty \leq 25%) values for most pixels” (Ramos Delgado P, Kuehne A, Aravina M, et al. 2021)

Following the *model-based B₁ correction*, concentration maps (**Figures 20C, 21C**) showed reduced ¹⁹F concentration in regions close to the RF probe and increased ¹⁹F concentration in regions with high SNR far from the CRP surface. The reliability of the correction is represented by the concentration uncertainty maps that mostly show values with 10<uncertainty≤25% (orange pixels) and ≤10% (green pixels) especially at higher SNR (**Figures 20D, 21D**).

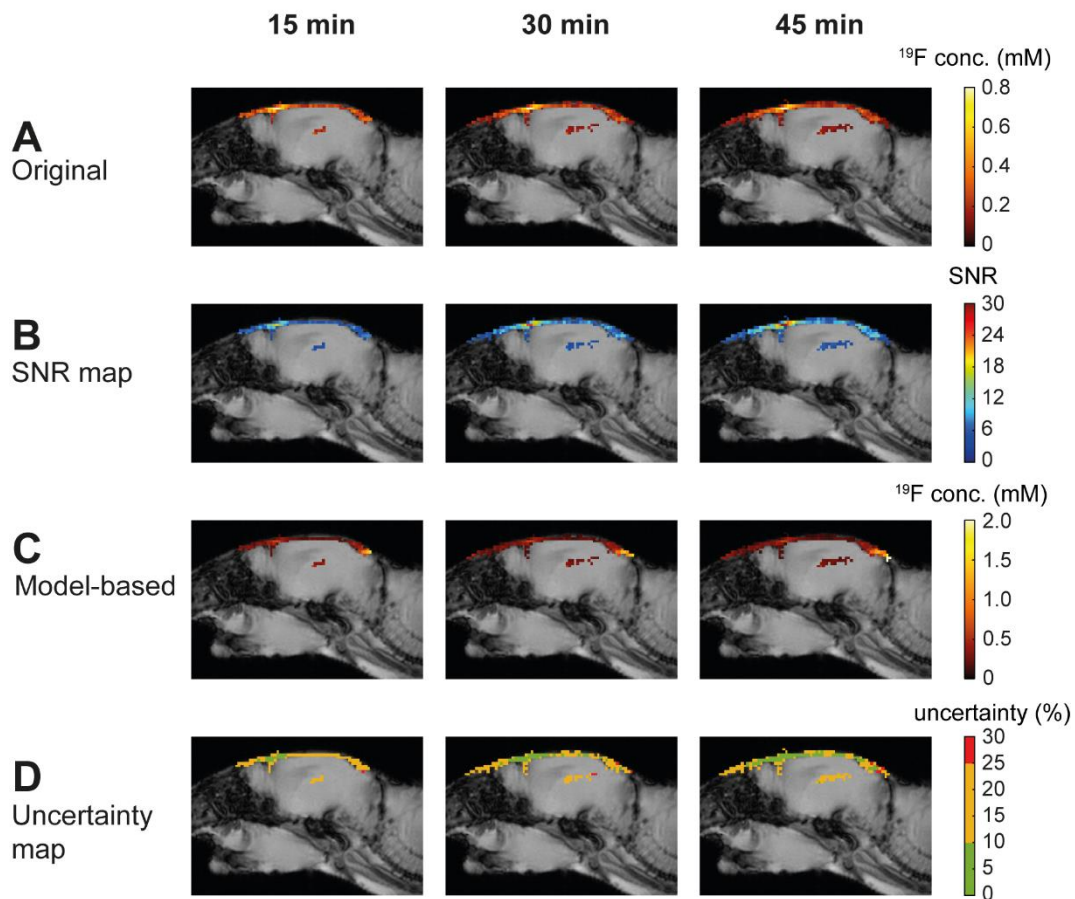


Figure 21. “*In vivo* EAE mouse 1 (score=2.5) in sagittal orientation. Concentration maps of original images (**A**) show an initial overestimation of the ¹⁹F concentration in regions close to the RF probe surface (e.g. meninges) which partly correspond with regions with high SNR (**B**). B₁-corrected images (**C**) present an adjustment in scale, where ¹⁹F concentration not only depends on the distance to the CRP surface and SNR (heavily dependent on B₁⁺ and B₁⁻) but on the ¹⁹F-NPs accumulated per pixel. The reliability of the B₁-corrected concentration maps is presented by the uncertainty maps (**D**) which show green (uncertainty≤10%) and orange (10%<uncertainty≤25%) values for most pixels” (Ramos Delgado P, Kuehne A, Aravina M, et al. 2021)

Compared to mouse 1, mouse 2 presented with more ¹⁹F signal, even though its disease score was less severe. This is evident from the original

concentration maps (**Figures 22A, 23A**) and corresponding SNR maps (**Figures 22B, 23B**). Mouse 2 exhibited meningeal inflammation, visible as a thin layer of ^{19}F signal with an SNR ranging from 3.6 to 49.5 and ^{19}F concentrations ranging from 0.1 to 1.7 mM, as well as inflammatory cell accumulation in deeper regions of the brain. After applying the *model-based correction* (**Figure 22C, 23C**), concentration maps showed an expected reduction in ^{19}F concentration in the meninges and an increase in features far from the CRP surface. Corresponding concentration uncertainty maps (**Figure 22D, 23D**) demonstrate the reliability of the B_1 corrections, with most pixels being orange ($10\% < \text{uncertainty} \leq 25\%$) and green ($\text{uncertainty} \leq 10\%$) especially at higher SNR.

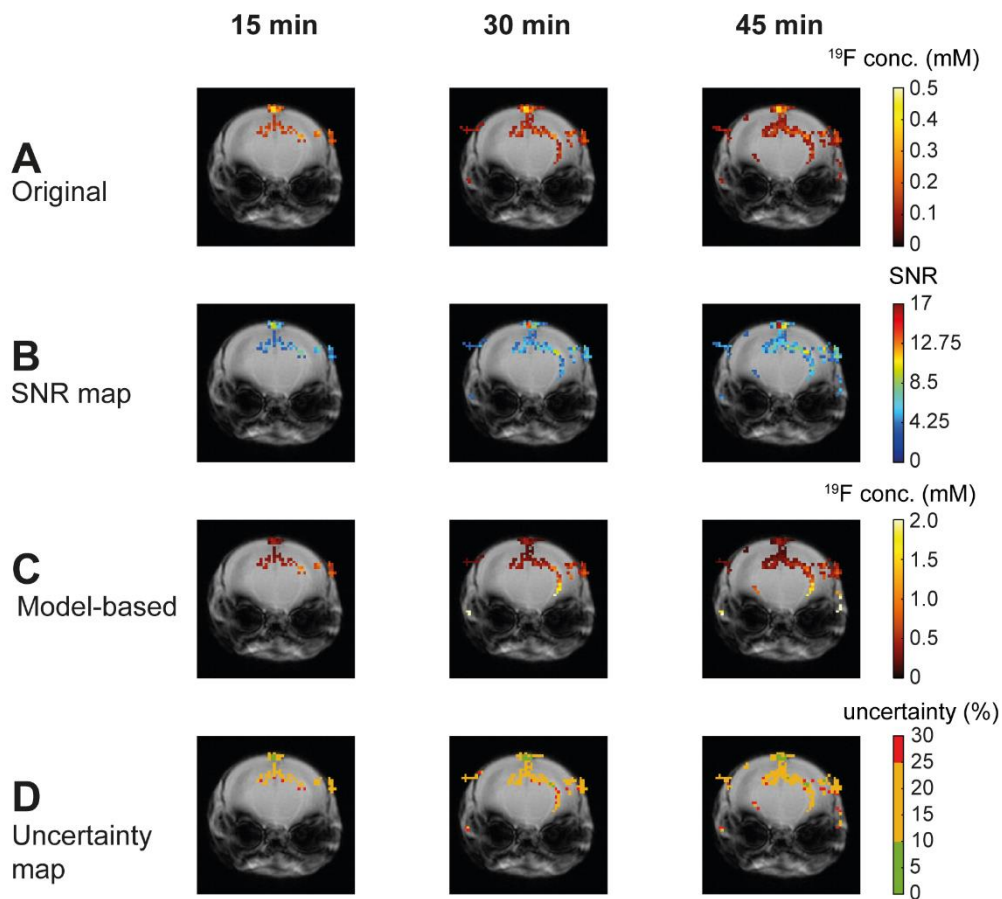


Figure 22. “*In vivo* EAE mouse 2 (score=1.5) in axial orientation. (A) Concentration maps of original images present signals in the meninges as well as in deeper regions of the brain, indicating increased inflammatory cell accumulation. (B) SNR maps show high SNR at pixels at the top of the mouse head and a reduced SNR in regions distant to the RF probe. After applying the *model-based B_1 correction* (C), concentration maps show an expected reduction in ^{19}F concentration in the meninges and an increase in pixels far from the CRP surface.

Corresponding uncertainty maps **(D)** demonstrate the reliability of the B_1 -corrected concentration maps, with most pixels indicating green (uncertainty \leq 10%) and orange (10%<uncertainty \leq 25%) values” (Ramos Delgado P, Kuehne A, Aravina M, et al. 2021)

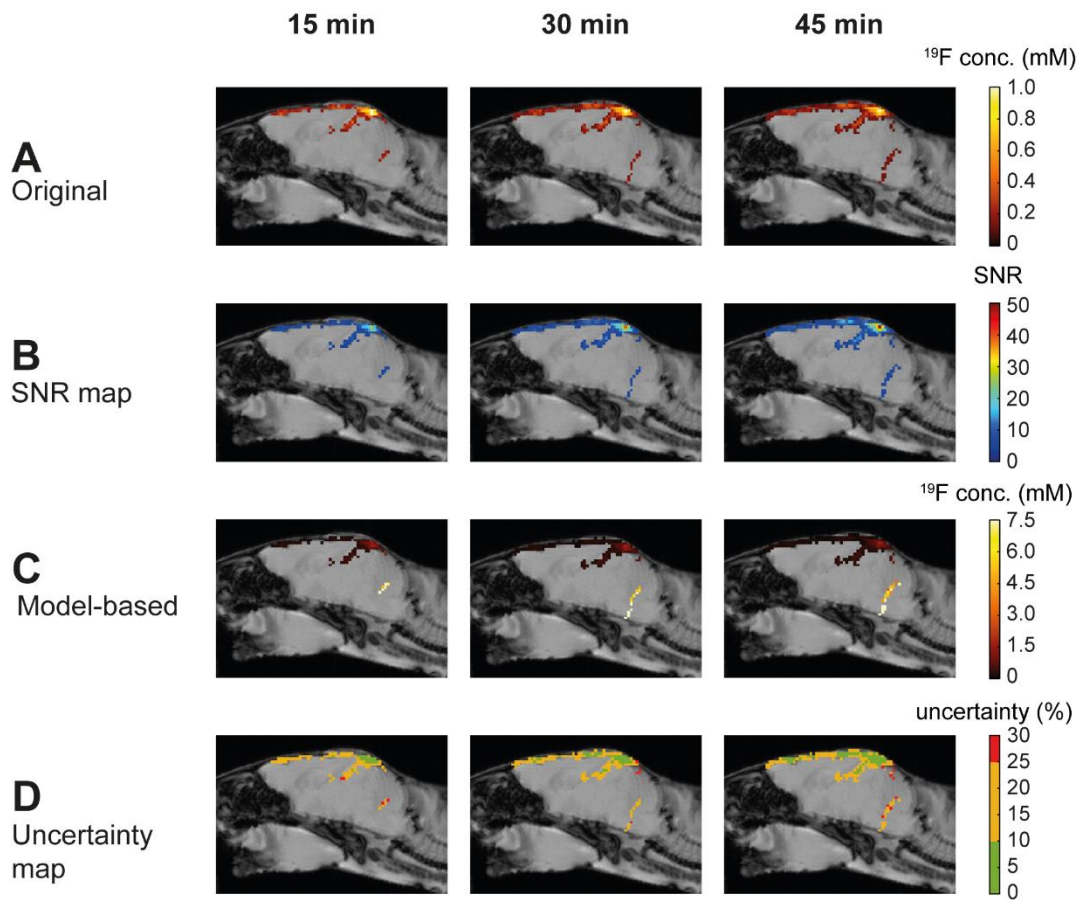


Figure 23. “*In vivo* EAE mouse 2 (score=1.5) in sagittal orientation. **(A)** Concentration maps of original images present signals in the meninges as well as in deeper regions of the brain, indicating increased inflammatory cell accumulation. **(B)** SNR maps show high SNR at pixels at the top of the mouse head and a reduced SNR in regions distant to the RF probe. After applying the *model-based B_1 correction* **(C)**, concentration maps show an expected reduction in ^{19}F concentration in the meninges and an increase in pixels far from the CRP surface. Corresponding uncertainty maps **(D)** demonstrate the reliability of the B_1 -corrected concentration maps, with most pixels indicating green (uncertainty \leq 10%) and orange (10%<uncertainty \leq 25%) values” (Ramos Delgado P, Kuehne A, Aravina M, et al. 2021)

3.2.5. Proportionality of hybrid and sensitivity methods for a “perfect” EPG-simulated RARE SI model

The *hybrid method* is proportional to the *sensitivity method* when the RARE SI model is calculated using simulations and does not have a bias introduced by measurements.

Both correction methods can be expressed as:

$$sensitivity = \frac{image(sample)}{image(uniform\ sample)}$$

$$hybrid = \frac{B_1^+ correction(image(sample))}{B_1^+ correction(image(uniform\ sample))}$$

being $image(sample)$ and $image(uniform\ sample)$ the image to be corrected and the uniform phantom image used for *sensitivity correction*, respectively.

Replacing the B_1^+ corrections by their definitions⁵¹ as:

$$= \frac{image(T_1(sample), FA) \times \frac{SI_{nominal}(sample)}{SI_{actual}(sample)}}{\left| image(T_1(uniform\ sample), FA) \times \frac{SI_{nominal}(uniform\ sample)}{SI_{actual}(uniform\ sample)} \right|}$$

Since $SI_{nominal}(sample)$ and $SI_{nominal}(uniform\ sample)$ are the SIs for perfect 90° excitations and both samples have constant T_1 relaxation times, they can be replaced by a constant. Similarly, $SI_{actual}(sample)$ and $SI_{actual}(uniform\ sample)$ are the SIs for the actual excitations FA which equal to a constant for each pixel. Thus:

$$= k \times \frac{image(T_1(sample), FA)}{\left| image(T_1(uniform\ sample), FA) \right|} = k \times sensitivity$$

3.3. Development of registration methods for longitudinal EAE studies: validation and applications

This chapter includes and uses results that have been published in:

Millward JM, **Ramos Delgado P**, Smorodchenko A, Boehmert L, Periquito J, Reimann HM, Prinz C, Els A, Scheel M, Bellmann-Strobl J, Waiczies H, Wuerfel J, Infante-Duarte C, Chien C, Kuchling J, Pohlmann A, Zipp F, Paul F, Niendorf T, Waiczies S. *Transient Enlargement of Brain Ventricles During Relapsing-Remitting Multiple Sclerosis and Experimental Autoimmune Encephalomyelitis*. JCI Insight, 2020; 5(21):e140040. DOI: 10.1172/jci.insight.140040

and therefore contains text, statements, passages and figures from this publication.

In the previous study it was necessary to develop a registration method to register ^{19}F -MR images onto anatomical ^1H -MR images in the EAE. The EAE mouse model mimics a relapse-remitting MS disease course (RRMS), and is associated with substantial macroscopic changes in the brain, namely transient changes in ventricle size (see **Figure 24A**).⁵⁵ This could severely challenge the quantification of longitudinal MR studies that follow the course of disease in the EAE, such as the previously presented ^{19}F -MR methods. To quantify the changes associated with brain inflammation, longitudinally-acquired images should be spatially aligned via registration methods. Due to the transient macroscopic changes in the EAE, registration is not trivial and requires standardized protocols and workflows that will enable the quantification of changes that are related to the pathology.

In this section, a registration approach was proposed and applied to T_1 mapping in association with GBCAs in a longitudinal study in order to provide quantitative information about the inflammatory lesion load in EAE mice. The obtained results demonstrated that T_1 mapping methods could be used as imaging biomarkers of disease activity in EAE. The author of this thesis registered all T_1 maps acquired during the longitudinal EAE study using a post-processing workflow.

3.3.1. Registration methods implementation and validation

Despite careful slice planning during the MR acquisitions, minor differences exist between slices. EAE-related anatomical changes (e.g. ventricle contractions and expansions) make voxel-by-voxel comparison even more challenging. **Figure 24A** shows an exemplary mid-brain slice demonstrating only very subtle longitudinal variations in position, slicing and structure within the brain. Images and T_1 maps show improved alignment despite substantial macroscopic changes in the EAE mouse brain (**Figure 24B-C**). This allows accurate image/map comparison due to improved voxel alignment. The workflow and registration procedure were applied to all EAE brain images for all time points investigated.

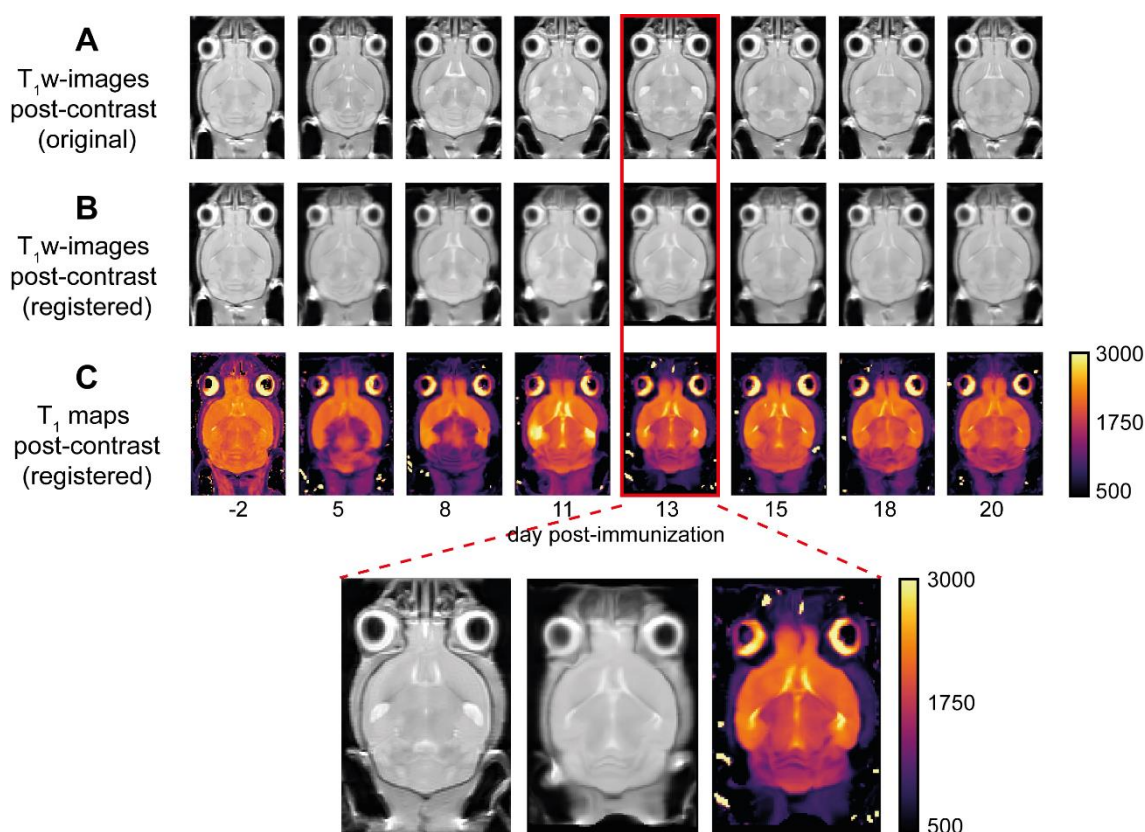


Figure 24. “Registration of post-contrast T_1 w-images and maps. (A) Minor differences within slices coexist with anatomical changes. (B) Registration increases similarity between slices allowing accurate comparison. (C) Registered T_1 maps, ready for quantification. The lower row corresponds to a zoom on day 13 post-immunization, demonstrating the successful intra-subject registration onto time point 1 (day 2 before immunization)” (Ramos Delgado P, Millward JM, Huelnhagen T, et al. ESMRMB 2020)

To demonstrate the robustness of this approach, ROIs defined for the baseline images (first time point, tp_1 , both brain and cerebellum) were superimposed with only minor changes onto ROIs replicated from tp_1 and applied to the entire series of 8 time points to perform a manual segmentation. **Figure 25** shows two exemplary images. On the left, ROIs were drawn onto the baseline T_1 -image. The image on the right shows the same ROIs superimposed onto the registered T_1 -image corresponding to tp_2 .

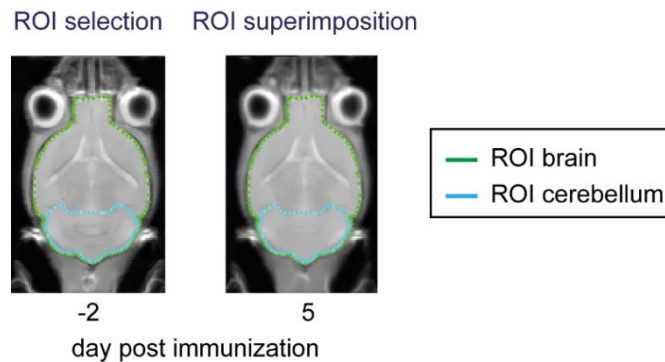


Figure 25. “ROI validation. After superimposing the ROIs drawn using tp_1 onto tp_2 , pixel-by-pixel correspondence was achieved. This was also the case for other time points and other animals” (Ramos Delgado P, Millward JM, Huelnhagen T, et al. ESMRMB 2020)

3.3.2. GBCA-lesion burden quantification as a measure of inflammation in EAE using T_1 mapping methods

A typical pattern of contrast enhancement—with diffuse lesions especially prominent in the cerebellum, meninges, and periventricular regions—was observed already by d5 post immunization (**Figure 26A**). The change in brain T_1 values after GBCA administration (ΔT_1 =pre-contrast minus post-contrast mean values) was calculated for $n=16$ mice, at time points ranging from baseline (d-2 post immunization) to d25 post immunization (**Figure 26B-C**). Compared with baseline, the ΔT_1 in the cerebellum was significantly increased at d8 and d11 post immunization (592.9 ± 103.8 ms and 551.2 ± 71.4 ms, respectively; p -value=0.0030) (**Figure 26B**). The ΔT_1 in the whole brain (**Figure 26BC**) was also significantly increased at d8 and d11 post immunization (373.1 ± 52.9 ms and 342.8 ± 43.2 ms, respectively; p -value=0.0023).

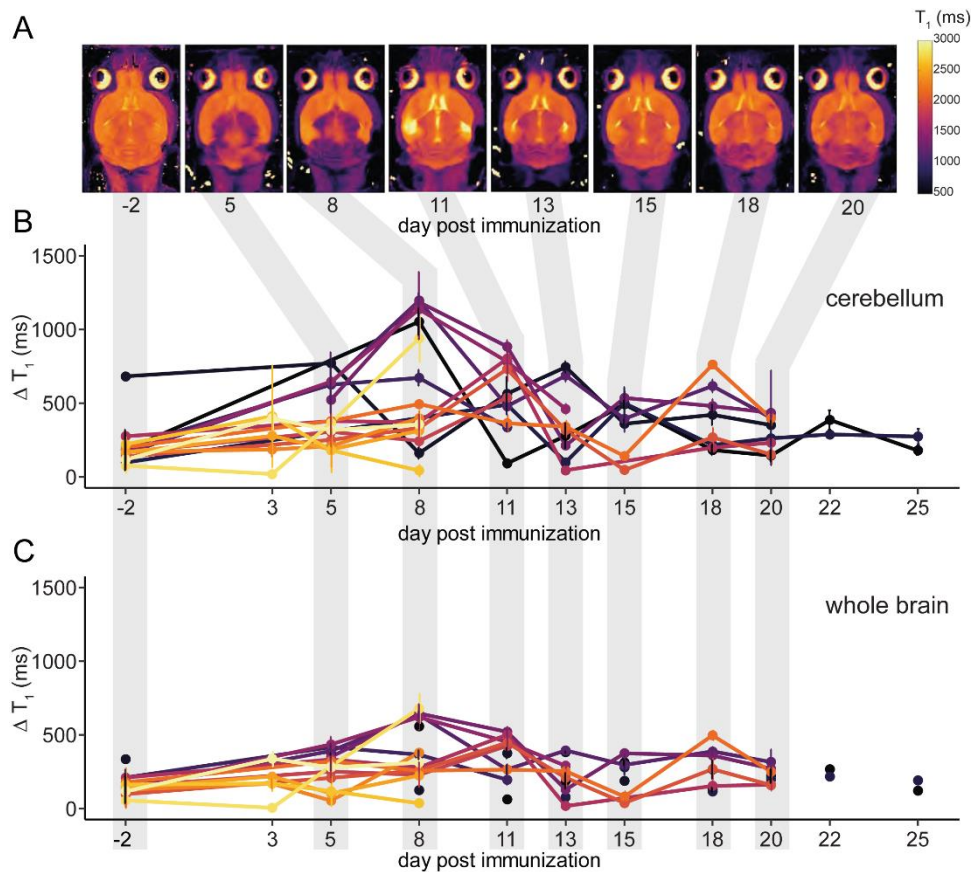


Figure 26. “Gadolinium-enhancing lesions can be used as an objective quantitative measure of inflammation in EAE. (A) T_1 map MRIs of a representative brain show altered tissue relaxation due to blood-brain barrier disruption following administration of gadolinium-based contrast agent. Reduced tissue T_1 (purple) is apparent in the meninges, cerebellum, and periventricular regions already by day 5 post immunization. Note that the brain images have been registered to the baseline image for quantification; therefore, changes in ventricle volume are not apparent in these images. **(B)** Quantification of global changes in tissue T_1 following gadolinium contrast administration were especially prominent in the cerebellum ($n=16$). The ΔT_1 (precontrast - postcontrast values) was significantly increased from baseline at days 8-11 post immunization (p -value=0.0030, ANOVA). **(C)** The ΔT_1 of the whole-brain was also significantly increased at days 8-11 post immunization (p -value=0.0023, ANOVA)” (Modified from Millward JM, Ramos Delgado P, Smorodchenko A, et al., 2020)

4. Discussion

This part of the thesis contains and uses the conclusions and discussion published in:

- **Ramos Delgado P**, Kuehne A, Periquito J, Millward JM, Pohlmann A, Waiczies S, Niendorf T. *B₁ Inhomogeneity Correction of RARE MRI with Transceive Surface Radiofrequency Probes*. *Magnetic Resonance in Medicine*, 2020; 84(5):2684-2701. DOI: 10.1002/mrm.28307
- **Ramos Delgado P**, Kuehne A, Aravina M, Millward JM, Vazquez A, Starke L, Waiczies H, Pohlmann A, Niendorf T, Waiczies S. *B₁ Inhomogeneity Correction of RARE MRI at Low SNR: Quantitative In Vivo ¹⁹F-MRI of Mouse Neuroinflammation with a Cryogenically-cooled Transceive Surface Radiofrequency Probe*. *Magnetic Resonance in Medicine*, 2021; 87(4):1952-1970. DOI: 10.1002/mrm.29094
- Millward JM, **Ramos Delgado P**, Smorodchenko A, Boehmert L, Periquito J, Reimann HM, Prinz C, Els A, Scheel M, Bellmann-Strobl J, Waiczies H, Wuerfel J, Infante-Duarte C, Chien C, Kuchling J, Pohlmann A, Zipp F, Paul F, Niendorf T, Waiczies S. *Transient Enlargement of Brain Ventricles During Relapsing-Remitting Multiple Sclerosis and Experimental Autoimmune Encephalomyelitis*. *JCI Insight*, 2020; 5(21):e140040. DOI: 10.1172/jci.insight.140040

and contains text, statements, passages and figures from these publications.

4.1. B₁ inhomogeneity correction in ¹H transceiver surface RF probes

Several methods have been described in the literature to correct B₁ inhomogeneities.⁴²⁻⁴⁶ These methods are especially crucial for images acquired with transceive surface RF coils. The main accomplishment of this project was to extend this work, demonstrating the feasibility and efficacy of B₁ inhomogeneity correction methods for RARE MRI, for which an analytical SI equation is not available.^{47,48}

Phantom results showed a substantial improvement in image homogeneity after B₁ correction using the investigated methods. The feasibility of these approaches for samples with more complex structures (*ex vivo* and *in vivo*

mouse) and in time-constrained scenarios (*in vivo*) was established. These results demonstrate that images derived from the correction procedures are suitable for accurate T_1 contrast and SI quantification purposes, thus opening the way for parametric T_1 mapping and X-nuclei quantification using surface transceive RF coils/probes. Compared to previously developed correction methods, these approaches are applicable to MR imaging techniques for which no analytical SI equation exists, including but not limited to EPI⁵⁰ and UTE⁴⁹ imaging techniques.

Although the *sensitivity correction* method³¹ is typically used to correct B_1^- inhomogeneities, this work demonstrated that this method is also effective for correction of B_1^+ inhomogeneities, since it includes an inherently linear B_1^+ correction—all images are the product of the transmission and reception capabilities of an RF coil. This concept is supported by the quasi-linear trends shown in the RARE SI model for SI vs. T_1 relaxation time, and the linear trends present for the majority of the SI vs. FA range (e.g. between 30°-70° and between 90°-140°).

The two novel B_1 correction methods (*model-based*, *hybrid*) proposed here use an empirical SI model of the RF pulse sequence. The correction workflow involves using the calculated SI model to adjust the SI to that of the nominal FA, based on the actual FA and T_1 . This rectifies the inhomogeneities related to RF transmission (B_1^+), whereas those related to the RF coil sensitivity (B_1^-) are addressed in a separate step using a previously calculated B_1^- map (*model-based*) or using a B_1^+ -corrected uniform phantom (*hybrid*).

Tests on corrected and reference images revealed a high image homogeneity, maintained when comparing the *ex vivo* phantom to the *in vivo* situation (difference in mean below 5% in both cases compared to reference images). Assessing the accuracy of SI quantification and T_1 contrast measurements yielded different results for RARE with and without flipback that drives the equilibrium regimen. Without the driven equilibrium regimen all correction methods reduced the errors to less than 10% for both quantification and T_1 contrast, and produced statistically significant improvements compared to the original data. For the driven equilibrium regimen, the errors in the original data were more pronounced, which translated into higher SI quantification and T_1

contrast errors after correction. For all three B_1 correction methods, errors were around 10% for quantification, but the accuracy of T_1 contrast was considerably reduced, with errors up to 20-30% (for high water content). Only the *sensitivity method* improved T_1 contrast significantly.

When flipback was inactive, all three methods performed similarly for SI quantification purposes, and yielded improved performance for the low T_1 mode. This can be attributed to the reduced T_1 -weighting at the repetition times used, so that less correction was needed. The *sensitivity correction* method performed slightly better than the other two for SI quantification purposes. The simplicity of this approach makes it preferable for absolute SI quantification. Conversely, results showed that the *hybrid correction* provides more accuracy in cases when T_1 contrast is essential (e.g. for contrast-enhanced imaging in inflammatory disease).

Overall, the *hybrid method* performed better than the *model-based* one. Since the only difference between them is the sensitivity profile calculation, it was concluded that the simple *sensitivity correction* performs better than the low flip angle approximation when computing a B_1^- map from measurements. The minor artifacts produced at regions distal to the coil are caused by inaccuracies in the FA information associated with low SNR.

The B_1 correction methods presented here have widespread implications. These methods are not only useful for the specific case of cryogenically-cooled RF probes, frequently used to boost SNR in preclinical MRI but are also generally applicable for transceive surface RF coils like single-loop RF coils. While the applicability of the correction methods in conventional ^1H brain imaging was thoroughly demonstrated, these methods can also be applied to moving organs, e.g. cardiovascular research, as long as the calculated reference power is correct and the maps and images are acquired using a trigger and spatially aligned. These B_1 correction methods permit quantitative SI and T_1 contrast measurements with transceiver surface RF coils, using MRI techniques for which analytical SI equations do not exist. This circumvents a key limitation, and offers a new approach for correcting B_1 inhomogeneity that may be applied for a broad range of biomedical research applications.

4.1.1. Limitations and future directions

The described *model-based approach* is fundamentally limited by SNR constraints at larger distances from the RF coil, and by the accuracy of the B_1 and T_1 maps and the polynomial fit. Determining the distance until which a meaningful correction can be achieved is challenging, since it depends on the conditions and scanning parameters used (e.g. RF coil dimensions, SNR, TA). Hence, this distance should be determined by each user, for each specific setup: 1) calculate the central profile plots for each correction; 2) determine at what distance from the coil the corrected profile still follows that of the reference volume RF coil. This will not require extra time, since T_1 mapping with the reference RF coil is anyway required for the B_1 correction.

Accurate knowledge of T_1 and FA is crucial for the precise correction of the B_1 inhomogeneities using the *model-based* and *hybrid methods*. For the presented workflow, readily-available MR imaging protocols (e.g. double angle mapping, RARE with variable TR) were selected. Limitations are related to the inherent instability associated with the FA and T_1 mapping techniques, the lack of an established gold standard, and substantial variability among the different methods. FA mapping depends on the slice excitation profile, B_0 homogeneity and other factors,⁷⁵ which produce additional uncertainties. Moreover, FA mapping techniques are usually imprecise for low FAs,⁷⁶ increasing the FA error at large distances from the RF coil.

T_1 mapping is equally challenging and subject to many sources of error. Fundamentally dependent on the FA, it is usually performed using volume resonators or a combination of RF coils for transmit-receive (volume for transmit, surface for receive) to attenuate the effects of B_1^+ inhomogeneity. A caveat of this method is the need to acquire a T_1 map with each image (in order to consider the T_1 contrast of tissues) when removing the field inhomogeneities in ^1H images. Although T_1 mapping is feasible using a cryo-cooled RF probe,⁷⁷ the extra time was invested on using a volume resonator to reduce T_1 map errors.

An alternative to calculate the signal evolution (SI model) would be to use extended phase graphs³⁹⁻⁴¹ or Bloch simulations.⁷⁸ Equally, magnetic

resonance fingerprinting (MRF)⁷⁹ could be used not only to create the model but also to acquire a T_1 and B_1 map altogether by changing FA and TR, reducing the amount of scan time needed and producing a tailored correction (“real” B_1 map of the phantom/mouse). According to our knowledge there are no MRF-RARE techniques available to date and the development of such MR sequences was out of the scope of this study.

When considering SNR, it is important to bear in mind that these correction methods entail multiplication by a position-dependent matrix of correction factors. Thus, both the signal and the noise will be increased; furthermore, this effect will be different for each image pixel. Therefore, SNR calculations must be performed on the original uncorrected images.

Differences seen in image homogeneity might be related to a change in animal position when transferring the animal from ^1H -CRP to reference RF coil. These differences might be also caused by motion (e.g. due to misalignment of the flip angle map, worse B_0 shimming, etc.). Although the option motion averaging was used, it might not have been enough to compensate for bulk motion. Since a RARE-based imaging sequence was used where the blood signal in large vessels is inherently suppressed due to the use of a spin-echo train, the changes in performance are not believed to be related to blood flow.⁸⁰

Finally, the proposed B_1 correction methods could be of high importance in future clinical applications due to the increasing use of transceive surface RF coils in human MRI at ultrahigh fields (UHF),⁸¹⁻⁸⁹ where large volume body RF coils are not used for signal excitation and are not provided with UHF-MR scanners.

4.2. B_1 inhomogeneity correction at low SNR using ^{19}F transceiver surface RF probes

The potential of ^{19}F -MR has long been recognized.¹⁷ However, low *in vivo* ^{19}F concentrations demand SNR-enhancing strategies. Transceive surface RF probes such as the ^{19}F -CRP maximize SNR but their inhomogeneous B_1 field hampers quantification. To date, efforts in B_1 field correction for ^{19}F -MRI have been scarce, and usually limited to less complex imaging techniques.^{43,77,90,91}

This part of this thesis project built upon the previous work on B_1 correction methods tailored for ^1H transceive surface RF probes and SNR-efficient RARE imaging to enable ^{19}F signal quantification in low SNR time-constrained scenarios. Low-concentration uniform phantom images showed considerable increase in homogeneity after B_1 correction even in low SNR regions distal from the coil. *Ex vivo* concentration maps using reference caps demonstrated substantial improvement in concentration estimation, compared to reference images. A method was established to determine concentration error after B_1 correction using Monte Carlo SNR simulations and an acquisition workflow to co-localize ^{19}F -CRP images with anatomical images from an external volume resonator. Furthermore, first *in vivo* ^{19}F -nanoparticle T_1 values were determined in EAE brains to compute *model-based corrections*. Successful implementation ultimately yielded the first quantitative *in vivo* ^{19}F -MR images of inflamed EAE brains using a ^{19}F -CRP.

In the previous study, several samples with different T_1 were prepared and scanned to compute the RARE SI model.⁵¹ Here, EPG simulations were introduced to reduce the burden on the MR measurements, improving the accuracy of the model; by eliminating possible errors introduced by the measurements, especially at low FAs where SIs corresponding to different T_1 s are closer to each other. Using EPG simulations, it was found that the *hybrid* and *sensitivity methods* yielded similar results, up to a constant factor. Unlike EPG simulations, imperfections originating from an empirical model disturb the symmetry underlying this degeneracy, thereby leading to slight differences between the *hybrid* and *sensitivity methods* (see chapter *Proportionality of hybrid and sensitivity methods for a “perfect” EPG-simulated RARE SI model*). This demonstrates that simulations have a clear advantage, which expected to also be true for other MR sequences lacking closed-form SI equations.

A reliable B_1 correction is indispensable for robustly quantifying the ^{19}F signal when employing the ^{19}F -CRP in studies using ^{19}F -NPs to measure the inflammatory burden in EAE *in vivo*. In this study, two EAE animals were presented with discrepancies between ^{19}F signal and clinical score—the animal with lower clinical severity showed more ^{19}F signal. This reflects the clinico-radiological paradox, well described in MS⁹² and EAE,⁹³ whereby clinical status

and radiological findings diverge, underscoring the urgent need to establish more quantitative MRI methods to assess disease severity objectively, such as that presented in the current study.

Furthermore, the uniform phantom was prepared with ^{19}F concentration (0.2 mM) and SNR (range 50 to 0) comparable to those achieved in EAE mice administered with PFCE-NPs (maximum ^{19}F concentration 2 mM, SNR between 50 and 0 in all cases). Since in transceive surface RF probes the SNR is much higher when close to the RF probe, the B_1 correction approach and uncertainty propagation model were assessed in realistic scenarios and validated for low SNRs far away from the RF probe (**Figures 17F-I**).

Monte Carlo SNR simulations were performed to estimate SI quantification uncertainties. Simulations were designed to include a wide SNR range (**Table 1**), taking into account the typically low SNR values for ^{19}F (SNR=0-10 in 0.5-steps) as well as higher SNRs (SNR up to 1500). Concentration uncertainty maps were found to yield a linear dependence of the uncertainty on SNR, with constant regions ($\leq 10\%$ with $\text{SNR} \geq 10.1$ and $\leq 25\%$ when $\text{SNR} \geq 4.25$). This is consistent with the results previously demonstrated for ^1H imaging, where SNR was not limited. The above-mentioned SNR requirements are highly relevant for the experimental implementation of the proposed approach and aim to guide other researchers to balance scan time with the uncertainty of the quantification of low SNR ^{19}F RARE MRI applications.

4.2.1. Limitations and future directions

The use of higher ETLs to further improve SNR through signal averaging produced ghosting artefacts in uniform phantoms (in test images, but also images used for *sensitivity correction*) in regions where ^{19}F signal was lower. This effect has been widely recognized^{94,95} and produced an abnormal increase of signal with the *sensitivity method* in regions adjacent to the artefact, which could not be removed even when changing phase encoding direction. The *model-based correction* was affected to a lesser extent (test images still showed ghosting artefacts), since this correction uses FA and B_1 maps computed with FLASH images. This was observed when correcting the uniform phantom where the *model-based correction* yielded MAPEs < 25% for all ROIs, and calculated

PIUs were equally higher than those achieved with the *sensitivity method*. Therefore, it was concluded that the *model-based correction method* is more robust than the *sensitivity method*, which poses some constraints in MR scanning parameters.

Reference caps placed above the phantoms or mouse heads were developed to allow for reference power calibrations. Little extra time was needed to acquire separate reference images to compute ^{19}F concentrations. Furthermore, individual B_1 maps were measured to correct more pixels in the reference caps, since the wall thickness of the 15-mL tube (0.8 mm) excluded more than half of the pixels of the reference. Corrections of the reference caps were nevertheless of poorer quality, with B_1 inhomogeneities at the sides. This was expected due to the large gradient close to the probe surface. Also, reference power adjustments may not be reliable in the close slices, further demonstrating that FA calibration is non-trivial and could be improved.^{90,96}

To examine the accuracy of B_1 -corrected *ex vivo* concentration maps, these were compared to those obtained with a volume resonator. Despite the best efforts to select an identical anatomical position with both volume resonators, minor differences in ^1H might cause slight changes in the visible ^{19}F signal. Nevertheless, there was overall good agreement in ^{19}F features and corresponding concentrations, confirmed by the computed uncertainty maps. *In vivo* error concentration maps showed positive results even when SNR values achieved were significantly lower than *ex vivo*, due to reduced scan times. Future studies using 3D-RARE combined with accelerated acquisition could help further improve concentration errors.^{97,98} Moreover, adiabatic pulses could be an interesting addition to 3D-RARE acquisitions to further improve B_1^+ -field uniformity up to a certain region.^{99,100} A subsequent *model-based B_1 correction* could be of value to increase the B_1 -corrected area.

The presented approach remarkably improved concentration errors from >100% to <25%. B_1 correction methods will be critical to ensure that the detected ^{19}F signal depends exclusively on ^{19}F spin density and not on distance to the RF probe surface, while utilizing the SNR benefit provided by ^{19}F -CRPs. These results are particularly promising for future clinical applications such as drug imaging, cell-tracking or cell therapy applications,¹⁰¹⁻¹⁰⁵ where the lower SNR

achieved at clinical field strengths necessitate the use of transceive surface RF probes.

4.3. Development of registration methods for longitudinal EAE studies

The last part of this thesis demonstrates the feasibility of the investigated registration methods for a time series of T₁w-images and T₁ mapping scans obtained from longitudinal EAE studies. The implemented registration process facilitated successful alignment of images, and was robust enough to accommodate the considerable macroscopic morphological changes of the EAE brain over time. Manual ROI definitions were easily translated to all timepoints, offering a suitable workflow for longitudinal neuroimmunological studies.

One important finding of this study was that T₁ mapping could objectively quantify GBCA lesion burden as a measure of inflammatory activity in EAE and that this correlated with disease activity and changes in ventricle volume. This method might be crucial when following inflammation over time in the animal model. In patients, contrast enhancements provide a semi-quantitative assessment that is typically enough to provide truthful lesion segmentation. However, this is even more challenging in EAE where lesions are less distinct, making segmentation prone to observer bias. The T₁ maps showed reduced T₁ values in regions of contrast enhancement typical for SJL mice, namely cerebellum, meninges and periventricular regions. This was most extensive in the cerebellum, which is a region with an expected largest lesion burden in SJL EAE mice. Taking advantage of the registration procedure, the corresponding ΔT_1 maps were calculated which show pronounced decreases of up to 70% in the measured T₁ value, indicating abundant disease activity. Therefore, it was demonstrated that T₁ mapping of EAE brains is a useful method to quantify gadolinium leakage as an indicator of BBB disruption and disease activity.

4.3.1. Limitations and future directions

ROIs of brain and cerebellum were manually defined for each animal. This approach, although rudimentary, was alleviated by the registration process. ROIs were only manually defined for the baseline images and then easily replicated to the entire series. To take these developments to the next level, the

registration pipeline could be extended to using registrations to a mouse brain atlas. This would perform a quasi-automatic brain segmentation, where the user's anatomical expertise would become of secondary importance. Future studies could also benefit from novel registration tools such as ANTx2,¹⁰⁶ especially tailored for animal studies, and which already includes the Allen mouse brain atlas.¹⁰⁷

Registration results would equally benefit of implementing brain extraction (namely skull-stripping) as a previous step. With less external structures to match to the template in the search for a common coordinate system, registration methods tend to perform better. However, skull-stripping should only be carried out when the study focuses solely on brain tissue.

Finally, it is worth mentioning that the proposed registration methods could be applied to other mouse models where macroscopic anatomical changes confound the subsequent image analysis or even to images acquired with other imaging modalities such as computed tomography (CT) or positron-emission tomography (PET) or even in multimodal longitudinal applications. These include but are not limited to cancer-related applications (e.g. to monitor tumour growth or contraction,¹⁰⁸ to compare images before and after performing surgical procedures or during the course of radiotherapy treatment), neuroimaging (e.g. stroke imaging,^{106,109} tissue loss monitoring in neurodegenerative diseases¹¹⁰) or orthopaedic imaging (e.g. preoperative planning of surgeries, following the course of disease in joint degeneration¹¹¹).

References

1. Hao D, Ai T, Goerner F, Hu X, Runge V, Tweedle M. MRI contrast agents: basic chemistry and safety. *Journal of Magnetic Resonance Imaging*. 2012;36(5):1060-1071.
2. Rohrer M, Bauer H, Mintorovich J, Requardt M, Weinmann H. Comparison of magnetic properties of MRI contrast media solutions at different magnetic field strengths. *Investigative Radiology*. 2005;40(11):715-724.
3. Lassmann H. Multiple Sclerosis Pathology. *Cold Spring Harbor Perspectives in Medicine*. 2018;8(3):a028936.
4. Ramos Delgado P, Millward J, Huelnhagen T, Reimann H, Niendorf T, Pohlmann A, Waiczies S. Quantitative assessment of gadolinium-enhancing lesion burden in experimental neuroinflammatory disease using T₁ mapping. Paper presented at: ESMRMB Online, 37th Annual Scientific Meeting; September 30-October 2 2020, 2020; Online.
5. Dendrou C, Fugger L, Friese M. Immunopathology of multiple sclerosis. *Nature Reviews Immunology*. 2015;15(9):545–558.
6. Glatigny S, Bettelli E. Experimental Autoimmune Encephalomyelitis (EAE) as Animal Models of Multiple Sclerosis (MS). *Cold Spring Harbor Perspectives in Medicine*. 2018;8(11):a028977.
7. Robinson A, Harp C, Noronha A, Miller S. The experimental autoimmune encephalomyelitis (EAE) model of MS: utility for understanding disease pathophysiology and treatment. In: Goodin D, ed. *Handbook of Clinical Neurology*. Vol 122. Amsterdam, The Netherlands: Elsevier BV; 2014:173-189.
8. Filippi M, Preziosa P, Banwell B, Barkhof F, Ciccarelli O, De Stefano N, Geurts J, Paul F, Reich D, Toosy A, Traboulsee A, Wattjes M, Yousry T, Gass A, Lubetzki C, Weinshenker B, Rocca M. Assessment of lesions on magnetic resonance imaging in multiple sclerosis: practical guidelines. *Brain*. 2019;142(7):1858-1875.
9. Sinnecker T, Kuchling J, Dusek P, Dörr J, Niendorf T, Paul F, Wuerfel J. Ultrahigh field MRI in clinical neuroimmunology: a potential contribution

to improved diagnostics and personalised disease management. *EPMA Journal*. 2015;6:16.

10. Nessler S, Boretius S, Stadelmann C, Bittner A, Merkler D, Hartung H, Michaelis T, Brück W, Frahm J, Sommer N, Hemmer B. Early MRI changes in a mouse model of multiple sclerosis are predictive of severe inflammatory tissue damage. *Brain*. 2007;130(8):2186-2198.
11. Waiczies H, Millward J, Lepore S, Infante-Duarte C, Pohlmann A, Niendorf T, Waiczies S. Identification of cellular infiltrates during early stages of brain inflammation with magnetic resonance microscopy. *PLoS One*. 2012;7(3):e32796.
12. Ku M, Waiczies S, Niendorf T, Pohlmann A. Assessment of blood brain barrier leakage with gadolinium-enhanced MRI. In: García Martín M, López Larrubia P, eds. *Preclinical MRI*. Vol 1718: Springer Protocols; 2018:395-408.
13. Stojanov D, Aracki-Trenkic A, Benedeto-Stojanov D. Gadolinium deposition within the dentate nucleus and globus pallidus after repeated administrations of gadolinium-based contrast agents-current status *Neuroradiology*. 2016;58(5):433-441.
14. McDonald R, McDonald J, Kallmes D, Jentoft M, Murray D, Thielen K, Williamson E, Eckel L. Intracranial gadolinium deposition after contrast-enhanced MR imaging. *Radiology*. 2015;275(3):772-782.
15. Weiskopf N, Edwards L, Helms G, Mohammadi S, Kirilina E. Quantitative magnetic resonance imaging of brain anatomy and in vivo histology. *Nature Reviews Physics*. 2021;3:570-588.
16. Niendorf T, Ji Y, Waiczies S. Fluorinated natural compounds and synthetic drugs. In: Flögel U, Ahrens E, eds. *Fluorine Magnetic Resonance Imaging*: Pan Stanford Publishing Pte. Ltd.; 2017:311-342.
17. Ruiz-Cabello J, Barnett B, Bottomley P, Bulte J. Fluorine (¹⁹F) MRS and MRI in biomedicine. *NMR in Biomedicine*. 2011;24(2):114-129.
18. Chen J, Lanza G, Wickline S. Quantitative magnetic resonance fluorine imaging: today and tomorrow. *Wiley Interdisciplinary Reviews in Nanomedicine and Nanobiotechnology*. 2015;2(4):431-440.
19. Kale S, Chen X, Henkelman R. Trading off SNR and resolution in MR images. *NMR in Biomedicine*. 2009;22(5):488-494.

20. Hennig J, Nauerth A, Friedburg H. RARE imaging: a fast imaging method for clinical MR. *Magnetic Resonance in Medicine*. 1986;3(6):823-833.
21. Mastropietro A, De Bernardi E, Breschi G, Zucca I, Cametti M, Soffientini C, de Curtis M, Terraneo G, Metrangolo P, Spreafico R, Resnati G, Baselli G. Optimization of Rapid Acquisition with Relaxation Enhancement (RARE) pulse sequence parameters for ¹⁹F-MRI Studies. *Journal of Magnetic Resonance Imaging*. 2014;40:162-170.
22. Faber C, Schmid F. Pulse sequence considerations and schemes. In: Flögel U, Ahrens E, eds. *Fluorine Magnetic Resonance Imaging*. Singapore: Pan Stanford Publishing Pte. Ltd.; 2017:3-27.
23. Niendorf T, Barth M, Kober F, Trattnig S. From ultrahigh to extreme field magnetic resonance: where physics, biology and medicine meet. *Magnetic Resonance Materials in Physics, Biology and Medicine*. 2016;29(3):309-311.
24. Ladd M. The quest for higher sensitivity in MRI through higher magnetic fields. *Zeitschrift für medizinische Physik*. 2018;28(1):1-3.
25. Waiczies S, Rosenberg J, Kuehne A, Starke L, Ramos Delgado P, Millward J, Prinz C, Periquito J, Pohlmann A, Waiczies H, Niendorf T. Fluorine-19 MRI at 21.1 T: enhanced spin-lattice relaxation of perfluoro-15-crown-5-ether and sensitivity as demonstrated in ex vivo murine neuroinflammation. *Magnetic Resonance Materials in Physics Biology and Medicine*. 2019;32(1):37-49.
26. Axel L, Hayes C. Surface coil magnetic resonance imaging. *Archives Internationales de Physiologie et de Biochimie*. 1985;93(5):11-18.
27. Kovacs H, Moskau D, Spraul M. Cryogenically cooled probes—a leap in NMR technology. *Progress in Nuclear Magnetic Resonance Spectroscopy*. 2005;46:131-155.
28. Baltés C, Radzwill N, Bosshard S, Marek D, Rudin M. Micro MRI of the mouse brain using a novel 400MHz cryogenic quadrature RF probe. *NMR in Biomedicine*. 2009;22:834-842.
29. Vaidya M, Collins C, Sodickson D, Brown R, Wiggins G, Lattanzi R. Dependence of B₁⁺ and B₁⁻ field patterns of surface coils on the electrical properties of the sample and the MR operating frequency. *Concepts in Magnetic Resonance Part B*. 2016;46B(1):25-40.

30. Keltner J, Carlson J, Roos M, Wong S, Wong T, Budinger T. Electromagnetic fields of surface coil *in vivo* NMR at high frequencies. *Magnetic Resonance in Medicine*. 1991;22(2):467-480.
31. Axel L, Constantini J, Listerud J. Intensity correction in surface-coil MR imaging. *American Journal of Roentgenology*. 1987;148(2):418-420.
32. Wicks D, Barker G, Tofts P. Correction of intensity nonuniformity in MR images of any orientation. *Magnetic resonance imaging*. 1993;11(2):183-196.
33. McVeigh E, Bronskill M, Henkelman R. Phase and sensitivity of receiver coils in magnetic resonance imaging. *Medical Physics*. 1986;13(6):806-814.
34. Baldanchani P, Pauly J, Spielman D. Designing adiabatic radio frequency pulses using the Shinnar–Le Roux algorithm. *Magnetic Resonance in Medicine*. 2010;64(3):843-851.
35. Zivkovic I, Teeuwisse W, Slobozhanyuk A, Nenasheva E, Webb A. High permittivity ceramics improve the transmit field and receive efficiency of a commercial extremity coil at 1.5 Tesla. *Journal of Magnetic Resonance*. 2019;299:59-65.
36. Ibrahim T, Lee R, Baertlein B, Abduljalil A, Zhu H, Robitaille P. Effect of RF coil excitation on field inhomogeneity at ultra high fields: a field optimized TEM resonator. *Magnetic Resonance Imaging*. 2001;19(10):1339-1347.
37. Lutti A, Hutton C, Finsterbusch J, Helms G, Weiskopf N. Optimization and validation of methods for mapping of the radiofrequency transmit field at 3T. *Magnetic Resonance in Medicine*. 2010;64(1):229-238.
38. Carinci F, Santoro D, von Samson-Himmelstjerna F, Lindel T, Dieringer M, Niendorf T. Characterization of phase-based methods used for transmission field uniformity mapping: a magnetic resonance study at 3.0T and 7.0T. *PLoS One*. 2013;8(3):e57982.
39. Hennig J. Echoes - How to Generate, Recognize, Use or Avoid them in MR-Imaging Sequences. Part II: Echoes in Imaging Sequences. *Concepts in Magnetic Resonance*. 1991;3(4):179-192.
40. Hennig J. Echoes—how to generate, recognize, use or avoid them in MR-imaging sequences. Part I: Fundamental and not so fundamental

- properties of spin echoes. *Concepts in Magnetic Resonance*. 1991;3(3):125-143.
41. Weigel M. Extended phase graphs: dephasing, RF pulses, and echoes - pure and simple. *Journal of Magnetic Resonance Imaging*. 2015;41(2):266-295.
 42. van Schie J, Lavini C, van Vliet L, Vos F. Feasibility of a fast method for B₁-inhomogeneity correction for FSPGR sequences. *Magnetic resonance imaging*. 2015;33(3):312-318.
 43. Vernikouskaya I, Pochert A, Lindén M, Rasche V. Quantitative ¹⁹F MRI of perfluoro-15-crown-5-ether using uniformity correction of the spin excitation and signal reception. *Magnetic Resonance Materials in Physics, Biology and Medicine*. 2019;32(1):25-36.
 44. Cooper M, Nguyen T, Spincemaille P, Prince M, Weinsaft J, Wang Y. Flip angle profile correction for T₁ and T₂ quantification with look-locker inversion recovery 2D SSFP imaging. *Magnetic Resonance in Medicine*. 2012;68(5):1579-1585.
 45. Wang J, Qiu M, Constable R. *In vivo* method for correcting transmit/receive nonuniformities with phased array coils. *Magnetic Resonance in Medicine*. 2005;53(3):666-674.
 46. Collewet G, Davenel A, Toussaint C, Akoka S. Correction of intensity nonuniformity in spin-echo T₁-weighted images. *Magnetic resonance imaging*. 2002;20(4):365-373.
 47. Meara S, Barker G. Evolution of the longitudinal magnetization for pulse sequences using a fast spin-echo readout: application to fluid-attenuated inversion-recovery and double inversion-recovery sequences. *Magnetic Resonance in Medicine*. 2005;54(1):241-245.
 48. Conturo T, Beth A, Arenstorf R, Price R. Simplified mathematical description of longitudinal recovery in multiple-echo sequences. *Magnetic Resonance in Medicine*. 1987;4(3):282-288.
 49. Robson D, Gatehouse P, Bydder M, Bydder G. Magnetic resonance: an introduction to ultrashort TE (UTE) imaging. *Journal of Computed Assisted Tomography*. 2003;27(6):825-846.
 50. Mansfield P. Multi-planar image formation using NMR spin echoes. *Journal of Physics C: Solid State Physics*. 1977;10(3):55-58.

51. Ramos Delgado P, Kuehne A, Periquito J, Millward J, Pohlmann A, Waiczies S, Niendorf T. B₁ Inhomogeneity Correction of RARE MRI with Transceive Surface Radiofrequency Probes *Magnetic Resonance in Medicine*. 2020;84(5):2684-2701.
52. Ramos Delgado P, Kuehne A, Aravina M, Millward J, Vázquez A, Starke L, Waiczies H, Pohlmann A, Niendorf T, Waiczies S. B₁ inhomogeneity correction of RARE MRI at low SNR: quantitative in vivo of ¹⁹F MRI of mouse neuroinflammation with a cryogenically-cooled transceive surface radiofrequency probe. *Magnetic Resonance in Medicine*. 2021;87(4):1952-1970.
53. Hoult D, Chen C, Sank V. Quadrature detection in the laboratory frame. *Magnetic Resonance in Medicine*. 1984;1(3):339-353.
54. Glover G, Hayes C, Pelc N, Edelstein W, Mueller O, Hart H, Hardy C, O'Donnell M, Barber W. Comparison of linear and circular polarization for magnetic resonance imaging. *Journal of Magnetic Resonance*. 1985;64(2):255-270.
55. Lepore S, Waiczies H, Hentschel J, Ji Y, Skodowski J, Pohlmann A, Millward J, Paul F, Wuerfel J, Niendorf T, Waiczies S. Enlargement of cerebral ventricles as an early indicator of encephalomyelitis. *PLoS One*. 2013;8(8):e72841.
56. Millward J, Ramos Delgado P, Smorodchenko A, Boehmert L, Periquito J, Reimann H, Prinz C, Els A, Scheel M, Bellmann-Strobl J, Waiczies H, Wuerfel J, Infante-Duarte C, Pohlmann A, Zipp F, Paul F, Niendorf T, Waiczies S. Transient enlargement of brain ventricles during relapsing-remitting multiple sclerosis and experimental autoimmune encephalomyelitis. *JCI Insight*. 2020;5(21):e140040.
57. Waiczies H, Lepore S, Drechsler S, Qadri F, Purfürst B, Sydow K, Dathe M, Kuehne A, Lindel T, Hoffman W, Pohlmann A, Niendorf T, Waiczies S. Visualizing brain inflammation with a shingled-leg radio-frequency head probe for ¹⁹F/¹H MRI. *Scientific Reports*. 2013;3:1280.
58. Waiczies S, Millward J, Starke L, Ramos Delgado P, Huelnhagen T, Prinz P, Marek D, Wecker D, Wissmann R, Koch S, Boehm-Sturm P, Waiczies H, Niendorf T, Pohlmann A. Enhanced fluorine-19 MRI sensitivity using a cryogenic radiofrequency probe: technical

- developments and *ex vivo* demonstration in a mouse model of neuroinflammation. *Scientific Reports*. 2017;7(1):9808.
59. Starke L, Niendorf T, Waiczies S. Data preparation protocol for low signal-to-noise ratio fluorine-19 MRI. In: Pohlmann A, Niendorf T, eds. *Preclinical MRI of the kidney: methods and protocols*: Springer US; 2021:711-722.
 60. Henkelman R. Measurement of signal intensities in the presence of noise in MR images. *Medical Physics*. 1985;12(232):232-233.
 61. Insko E, Bolinger L. Mapping of the radiofrequency field. *Journal of Magnetic Resonance*. 1993;103A(1):82-85.
 62. *Polyfitn* [computer program]. Version 1.3. File Exchange: The MathWorks, Inc.; 2016.
 63. Ibrahim T, Hue Y, Tang L. Understanding and manipulating the RF fields at high field MRI. *NMR in Biomedicine*. 2009;22(9):927-936.
 64. Pauly J, Nishimura D, Macovski A. A k-space analysis of small-tip-angle excitation. *Journal of Magnetic Resonance*. 1989;81(1):43-56.
 65. Manjón J, Coupé P, Martí-Bonmatí L, Collins D, Robles M. Adaptive non-local means denoising of MR images with spatially varying noise levels. *Journal of Magnetic Resonance Imaging*. 2010;31(1):192-203.
 66. Price R, Axel L, Morgan T, Newman R, Perman W, Schneiders N, Selikson M, Wood M, Thomas S. Quality assurance methods and phantoms for magnetic resonance imaging: report of AAPM nuclear magnetic resonance Task Group No. 1. *Medical Physics*. 1989;17(2):287-295.
 67. Zhang J. Modern Monte Carlo methods for efficient uncertainty quantification and propagation: A survey. *Wiley Interdisciplinary Reviews in Computational Statistics*. 2020;13(5):e1539.
 68. Kroese D, Rubinstein R. Monte Carlo methods. *Wiley Interdisciplinary Reviews in Computational Statistics*. 2012;4(1):48-58.
 69. *MIJ: Running ImageJ and Fiji within Matlab* [computer program]. Version 1.5.0.0. File Exchange: The MathWorks, Inc.; 2020.
 70. Avants B, Yushkevich P, Pluta J, Minkoff D, Korczykowski M, Detre J, Gee J. The Optimal Template Effect in Hippocampus Studies of Diseased Populations. *Neuroimage*. 2010;49(3).

71. Avants B, Tustison N, Song G, Cook P, Klein A, Gee J. A Reproducible Evaluation of ANTs Similarity Metric Performance in Brain Image Registration. *Neuroimage*. 2011;54(3):2033-2044.
72. Jacoby C, Temme S, Mayenfels F, Benoit N, Krafft M, Schubert R, Schrader J, Flögel U. Probing different perfluorocarbons for in vivo inflammation imaging by ¹⁹F MRI: image reconstruction, biological half-lives and sensitivity. *NMR in Biomedicine*. 2013;27(3):261-271.
73. Prinz C, Ramos Delgado P, Eigentler T, Starke L, Niendorf T, Waiczies S. Toward ¹⁹F magnetic resonance thermometry: spin–lattice and spin–spinrelaxation times and temperature dependence of fluorinated drugs at 9.4 T. *Magnetic Resonance Materials in Physics, Biology and Medicine*. 2018;32(1):51-61.
74. *Nhist function* [computer program]. Version 1.13.0.0. File Exchange: The MathWorks, Inc.; 2015.
75. Wang J, Mao W, Qiu M, Smith M, Constable R. Factors influencing flip angle mapping in MRI: RF pulse shape, slice-select gradients, off-resonance excitation, and B₀ inhomogeneities. *Magnetic Resonance in Medicine*. 2006;56(2):463-468.
76. Balezeau F, Eliat P, Cayamo A, Saint-Jalmes H. Mapping of low flip angles in magnetic resonance. *Physics in medicine and biology*. 2011;56(20):6635-6647.
77. Khalil A, Mueller S, Foddiss M, Mosch L, Lips J, Przesdzing I, Temme S, Flögel U, Dirnagl U, Boehm-Sturm P. Longitudinal ¹⁹F magnetic resonance imaging of brain oxygenation in a mouse model of vascular cognitive impairment using a cryogenic radiofrequency coil. *Magnetic Resonance Materials in Physics, Biology and Medicine*. 2019;32(1):105-114.
78. Bloch F. Nuclear induction. *Physical Review*. 1946;70(7-8):460-474.
79. Ma D, Gulani V, Seiberlich N, Liu K, Sunshine J, Duerk J, Griswold M. Magnetic resonance fingerprinting. *Nature*. 2013;495(7440):187-192.
80. Feinberg D, Mills C, Posin J, Ortendahl D, Hylton N, Crooks L, Watts J, Kaufman L, Arakawa M, Hoenninger J, Brant-Zawadzki M. Multiple spin-echo magnetic resonance imaging. *Radiology*. 1985;155:437-442.

81. Hosseinnezhadian S, Frass-Kriegl R, Goluch-Roat S, Pichler M, Siegf J, Vit M, Poirier-Quinot M, Darrasse L, Moser E, Ginefri J, Laistler E. A flexible 12-channel transceiver array of transmission line resonators for 7 T MRI. *Journal of Magnetic Resonance*. 2018;296:47-59.
82. Pinkerton R, Barberi E, Menon R. Transceive surface coil array for magnetic resonance imaging of the human brain at 4 T. *Magnetic Resonance in Medicine*. 2005;54(2):499-503.
83. Pinkerton R, Near J, Barberi E, Menon R, Bartha R. Transceive surface coil array for MRI of the human prostate at 4T. *Magnetic Resonance in Medicine*. 2007;57(2):455-458.
84. Graessl A, Renz W, Hezel F, Dieringer M, Winter L, Oezerdem C, Rieger J, Kellman P, Santoro D, Lindel T, Frauenrath T, Pfeiffer H, Niendorf T. Modular 32-channel transceiver coil array for cardiac MRI at 7.0T. *Magnetic Resonance in Medicine*. 2014;72(1):276-290.
85. Rietsch S, Pfaffenrot V, Bitz A, Orzada S, Brunheim S, Lazik-Palm A, Theysohn J, Ladd M, Quick H, Kraff O. An 8-channel transceiver 7-channel receive RF coil setup for high SNR ultrahigh-field MRI of the shoulder at 7T. *Medical Physics*. 2017;44(12):6195-6208.
86. He X, Ertürk M, Grant A, Wu X, Lagore R, DelaBarre L, Eryaman Y, Adriany G, Auerbach E, Van de Moortele P, Ugurbil K, Metzger G. First in-vivo human imaging at 10.5T: Imaging the body at 447 MHz. *Magnetic Resonance in Medicine*. 2019;51(2).
87. Ertürk M, Raaijmakers A, Adriany G, Ugurbil K, Metzger G. A 16-channel combined loop-dipole transceiver array for 7 Tesla body MRI. *Magnetic Resonance in Medicine*. 2017;77(2):884-894.
88. Weinberger O, Winter L, Dieringer M, Els A, Oezerdem C, Rieger J, Kuehne A, Cassara A, Pfeiffer H, Wetterling F, Niendorf T. Local multi-channel RF surface coil versus body RF coil transmission for cardiac magnetic resonance at 3 Tesla: which configuration is winning the game? *PLoS One*. 2016;11(9):e0161863.
89. Niendorf T, Paul K, Oezerdem C, Graessl A, Klix S, Huelnhagen T, Hezel F, Rieger J, Waiczies H, Frahm J, Nagel A, Oberacker E, Winter L. W(h)ither human cardiac and body magnetic resonance at ultrahigh

- fields? technical advances, practical considerations, applications, and clinical opportunities. *NMR in Biomedicine*. 2016;29(9):1173-1197.
90. Goette M, Lanza G, Caruthers S, Wickline S. Improved quantitative ¹⁹F MR molecular imaging with flip angle calibration and B₁-mapping compensation. *Journal of Magnetic Resonance Imaging*. 2015;42(2):488-494.
 91. Constantinides C, Maguire M, McNeill E, Carnicer R, Swider E, Srinivas M, Carr C, Schneider J. Fast, quantitative, murine cardiac ¹⁹F MRI/MRS of PFCE-labeled progenitor stem cells and macrophages at 9.4T. *PLoS One*. 2018;13(1):e0190558.
 92. Barkhof F. The clinico-radiological paradox in multiple sclerosis revisited. *Current Opinion in Neurology*. 2002;15(3):239-245.
 93. Wuerfel J, Tysiak E, Prozorovski T, Smyth M, Mueller S, Schnorr J, Taupitz M, Zipp F. Mouse model mimics multiple sclerosis in the clinico-radiological paradox. *European Journal of Neuroscience*. 2007;26(1):190-198.
 94. Zhou X, Liang Z, Cofer G, Beaulieu C, Suddarth S, Johnson G. Reduction of Ringing and Blurring Artifacts in Fast Spin-Echo Imaging. *Journal of Magnetic Resonance Imaging*. 1993;3(5):803-807.
 95. Mulkern R, Wong S, Winalski C, Jolesz F. Contrast manipulation and artifact assessment of 2D and 3D RARE sequences. *Magnetic Resonance Imaging*. 1990;8(5):557-566.
 96. Schulte R, Sacolick L, Deppe M, Janich M, Schwaiger M, Wild J, Wiesinger F. Transmit gain calibration for nonproton MR using the Bloch–Siegert shift. *NMR in Biomedicine*. 2010;24(9):1068-1072.
 97. Zhong J, Mills P, Hitchens T, Ahrens E. Accelerated fluorine-19 MRI cell tracking using compressed sensing. *Magnetic Resonance in Medicine*. 2013;69:1683-1690.
 98. Darçot E, Yerly J, Hilbert T, Colotti R, Najdenovska E, Kober T, Stuber M, van Heeswijk R. Compressed sensing with signal averaging for improved sensitivity and motion artifact reduction in fluorine-19 MRI. *NMR in Biomedicine*. 2021;34(1):e4418.

99. Zhou X. Adiabatic radiofrequency pulses. In: Bernstein M, King K, Zhou X, eds. *Handbook of MRI Pulse Sequences*: Elsevier Academic Press; 2004:177-212.
100. de Graaf R, Rothman D, Behar K. Adiabatic RARE imaging. *NMR in Biomedicine*. 2003;16(1):29-35.
101. Ahrens E, Helfer B, O'Hanlon C, Schirda C. Clinical cell therapy imaging using a perfluorocarbon tracer and fluorine-19 MRI. *Magnetic Resonance in Medicine*. 2014;72(6):1696-1701.
102. Amiri H, Srinivas M, Veltien A, van Uden M, de Vries I, Heerschap A. Cell tracking using (19)F magnetic resonance imaging: technical aspects and challenges towards clinical applications. *European Radiology*. 2015;25(3):726-735.
103. Chapelin F, Capitini C, Ahrens E. Fluorine-19 MRI for detection and quantification of immune cell therapy for cancer. *Journal for ImmunoTherapy of Cancer*. 2018;6:105.
104. Fox M, Gaudet J, Foster P. Fluorine-19 MRI Contrast Agents for Cell Tracking and Lung Imaging. *Magnetic Resonance Insights*. 2016;22(8 (Suppl.1)):53-67.
105. Ku M, Edes I, Bendix I, Pohlmann A, Waiczies H, Prozorovski T, Günther M, Martin C, Pagès G, Wolf S, Kettenmann H, Uckert W, Niendorf T, Waiczies S. ERK1 as a therapeutic target for dendritic cell vaccination against high-grade gliomas. *Molecular Cancer Therapeutics*. 2016;15(8):1975-1987.
106. Koch S, Mueller S, Foddiss M, Bienert T, von Elverfeldt D, Knab F, Farr T, Bernard R, Dopatka M, Rex A, Dirnagl U, Harms C, Boehm-Sturm P. Atlas registration for edema-corrected MRI lesion volume in mouse stroke models. *Journal of Cerebral Blood Flow & Metabolism*. 2019;39(2):313-323.
107. Lein E, Hawrylycz J, Ao N, Ayres M, Bensinger A, Bernard A, Boe A, Boguski M, Brockway K, Byrnes E, Chen L, Chen L, Chen T, Chin M, Chong J, Crook B, Czaplinska A, Dang C, Datta S, Dee N, Desaki A, Desta T, Diep E, Dolbeare T, Donelan M, Dong H, Dougherty J, Duncan B, Ebbert A, Eichele G, Estin L, Faber C, Facer B, Fields R, Fischer S, Fliss T, Frensley C, Gates S, Glattfelder K, Halverson K, Hart M,

- Hohmann J, Howell M, Jeung D, Johnson R, Karr P, Kawal R, Kidney J, Knapik R, Kuan C, Lake J, Laramée A, Kirk D, Lau C, Lemon T, Liang A, Liu Y, Luong L, Michaels J, Morgan J, Morgan R, Mortrud M, Mosqueda N, Ng L, Ng R, Orta G, Overly C, Pak T, Parry S, Pathak S, Pearson O, Puchalski R, Riley Y, Rockett H, Rowland S, Royall J, Ruiz M, Sarno N, Schaffnit K, Shapovalova N, Sivisay T, Slaughterbeck C, Smith S, Smith K, Smith B, Sodt A, Stewart N, Stumpf K, Sunkin S, Sutram M, Tam A, Teemer C, Thaller C, Thompson C, Varnam L, Visel A, Whitlock R, Wohnoutka P, Wolkey C, Wong V, Wood M, Yaylaoglu M, Young R, Youngstrom B, Yuan X, Zhang B, Zwingman T, Jones A. Genome-wide atlas of gene expression in the adult mouse brain. *Nature*. 2007;445:168-176.
- 108.** Pei L, Bakas S, Vossough A, Reza S, Davatzikos C, Iftekharuddin K. Longitudinal brain tumor segmentation prediction in MRI using feature and label fusion. *Biomedical Signal Processing and Control*. 2020;55:101648.
- 109.** Mulder I, Khmelinskii A, Dzyubachyk O, de Jong S, Rieff N, Wermer M, Hoehn M, Lelieveldt B, van den Maagdenberg A. Automated ischemic lesion segmentation in MRI mouse brain data after transient middle cerebral artery occlusion. *Frontiers in Neuroinformatics*. 2017;11(3).
- 110.** Klohs J, Politano A, Deistung A, Grandjean J, Drewek A, Dominietto M, Keist R, Schweser F, Reichenbach J, Nitsch R, Knuesel I, Rudin M. Longitudinal assessment of amyloid pathology in transgenic ArcA β mice using multi-parametric magnetic resonance imaging. *PLoS One*. 2013;8(6):e66097.
- 111.** Proulx S, Kwok E, You Z, Papuga M, Beck C, Shealy D, Richtlin C, Awad H, Boyce B, Xing L, Schwarz E. Longitudinal assessment of synovial, lymph node, and bone volumes in inflammatory arthritis in mice using in vivo MRI and micro-CT. *Arthritis & Rheumatology*. 2007;56(12):4024-4037.

Statutory Declaration

"I, Paula Ramos Delgado, by personally signing this document in lieu of an oath, hereby affirm that I prepared the submitted dissertation on the topic "Development of Fluorine-19 and Proton Magnetic Resonance Imaging and its Application in Neuroinflammation" / "Entwicklung von Fluor-19 und Protonen-Magnetresonanztomographie und ihre Anwendung bei Neuroentzündung", independently and without the support of third parties, and that I used no other sources and aids than those stated.

All parts which are based on the publications or presentations of other authors, either in letter or in spirit, are specified as such in accordance with the citing guidelines. The sections on methodology (in particular regarding practical work, laboratory regulations, statistical processing) and results (in particular regarding figures, charts and tables) are exclusively my responsibility.

Furthermore, I declare that I have correctly marked all of the data, the analyses, and the conclusions generated from data obtained in collaboration with other persons, and that I have correctly marked my own contribution and the contributions of other persons (cf. declaration of contribution). I have correctly marked all texts or parts of texts that were generated in collaboration with other persons.

My contributions to any publications to this dissertation correspond to those stated in the below joint declaration made together with the supervisor. All publications created within the scope of the dissertation comply with the guidelines of the ICMJE (International Committee of Medical Journal Editors; www.icmje.org) on authorship. In addition, I declare that I shall comply with the regulations of Charité – Universitätsmedizin Berlin on ensuring good scientific practice.

I declare that I have not yet submitted this dissertation in identical or similar form to another Faculty.

The significance of this statutory declaration and the consequences of a false statutory declaration under criminal law (Sections 156, 161 of the German

Criminal Code) are known to me.”

Date

Signature

Declaration of own contribution

Paula Ramos Delgado contributed the following to the publications:

Publication 1

Ramos Delgado P, Kuehne A, Periquito J, Millward JM, Pohlmann A, Waiczies S, Niendorf T. *B₁ Inhomogeneity Correction of RARE MRI with Transceive Surface Radiofrequency Probes*. *Magnetic Resonance in Medicine*, 2020; 84(5):2684-2701. DOI: 10.1002/mrm.28307

Contribution:

- Extensive literature research and understanding of the current state of the art
- Study conception and design
- Primary data acquisition
- Implementation, validation and comparison of three B₁ correction methods
- Data analysis and its critical interpretation
- Creation of all diagrams and figures
- Writing and revising the manuscript

Publication 2

Ramos Delgado P, Kuehne A, Aravina M, Millward JM, Vazquez A, Starke L, Waiczies H, Pohlmann A, Niendorf T, Waiczies S. B₁ Inhomogeneity Correction of RARE MRI at Low SNR: Quantitative In Vivo ¹⁹F-MRI of Mouse Neuroinflammation with a Cryogenically-cooled Transceive Surface Radiofrequency Probe. *Magnetic Resonance in Medicine*, 2021; 87(4):1952-1970. DOI: 10.1002/mrm.29094

Contribution:

- Extensive literature research and understanding of the current state of the art
- Study conception and design
- Setup design for combined anatomical and ¹⁹F-MR image acquisition using single-tuned RF probes
- Primary data acquisition
- Characterization of the MR properties of ¹⁹F-nanoparticles in the EAE brain during pathology
- Implementation and evaluation of the developed B₁ correction methods to quantify ¹⁹F images
- Data analysis and its critical interpretation
- Creation of all diagrams and figures
- Writing and revising the manuscript

Publication 3

Millward JM, **Ramos Delgado P**, Smorodchenko A, Boehmert L, Periquito J, Reimann HM, Prinz C, Els A, Scheel M, Bellmann-Strobl J, Waiczies H, Wuerfel J, Infante-Duarte C, Chien C, Kuchling J, Pohlmann A, Zipp F, Paul F, Niendorf T, Waiczies S. *Transient Enlargement Of Brain Ventricles During Relapsing-Remitting Multiple Sclerosis And Experimental Autoimmune Encephalomyelitis*. JCI Insight, 2020; 5(21):e140040. DOI: 10.1172/jci.insight.140040

Contribution:

- Extensive literature research and understanding of the current state of the art of registration techniques during large macroscopic anatomical changes
- Development of registration protocol for anatomical data with macroscopic changes associated with EAE pathology
- Design and implementation of a tool for manual brain segmentation
- Data analysis and its critical interpretation, including quantification of T₁ maps
- Prepared registered images for the figure draft (Figures 1 and 2)
- Assisted in writing and revising the manuscript

Signature, date and stamp of first supervising university professor / lecturer

Signature of doctoral candidate

Journal Data Filtered By: **Selected JCR Year: 2018** Selected Editions: SCIE,SSCI
 Selected Categories: **"RADIOLOGY, NUCLEAR MEDICINE and MEDICAL IMAGING"** Selected Category Scheme: WoS
Gesamtanzahl: 129 Journale

Rank	Full Journal Title	Total Cites	Journal Impact Factor	Eigenfactor Score
1	JACC-Cardiovascular Imaging	8,801	10.975	0.026160
2	MEDICAL IMAGE ANALYSIS	7,694	8.880	0.013370
3	IEEE TRANSACTIONS ON MEDICAL IMAGING	19,545	7.816	0.024990
4	RADIOLOGY	54,641	7.608	0.061300
5	JOURNAL OF NUCLEAR MEDICINE	27,551	7.354	0.037990
6	EUROPEAN JOURNAL OF NUCLEAR MEDICINE AND MOLECULAR IMAGING	15,406	7.182	0.024760
7	CLINICAL NUCLEAR MEDICINE	4,922	6.498	0.007680
8	INTERNATIONAL JOURNAL OF RADIATION ONCOLOGY BIOLOGY PHYSICS	45,833	6.203	0.046810
9	INVESTIGATIVE RADIOLOGY	6,563	6.091	0.011150
10	Circulation-Cardiovascular Imaging	5,456	5.813	0.018480
11	NEUROIMAGE	99,720	5.812	0.132720
12	ULTRASOUND IN OBSTETRICS & GYNECOLOGY	12,336	5.595	0.020140
13	European Heart Journal-Cardiovascular Imaging	5,498	5.260	0.021650
14	RADIOTHERAPY AND ONCOLOGY	17,873	5.252	0.027470
15	Photoacoustics	512	5.250	0.001330
16	JOURNAL OF CARDIOVASCULAR MAGNETIC RESONANCE	5,113	5.070	0.014020
17	ULTRASCHALL IN DER MEDIZIN	2,238	4.613	0.003700
18	HUMAN BRAIN MAPPING	22,040	4.554	0.043230
19	JOURNAL OF NUCLEAR CARDIOLOGY	3,711	4.112	0.004480
20	EUROPEAN RADIOLOGY	19,597	3.962	0.033870

1




Selected JCR Year: 2018; Selected Categories: "RADIOLOGY, NUCLEAR MEDICINE and MEDICAL IMAGING"

Rank	Full Journal Title	Total Cites	Journal Impact Factor	Eigenfactor Score
21	RADIOGRAPHICS	11,768	3.923	0.009170
22	Biomedical Optics Express	9,547	3.910	0.021750
23	MAGNETIC RESONANCE IN MEDICINE	32,648	3.858	0.034990
24	SEMINARS IN NUCLEAR MEDICINE	2,245	3.798	0.002710
25	Journal of the American College of Radiology	4,191	3.785	0.009760
26	JOURNAL OF MAGNETIC RESONANCE IMAGING	17,147	3.732	0.027800
27	KOREAN JOURNAL OF RADIOLOGY	2,687	3.730	0.004800
28	INTERNATIONAL JOURNAL OF HYPERTHERMIA	3,552	3.589	0.004020
29	EJNMMI Physics	394	3.475	0.001350
30	NMR IN BIOMEDICINE	7,511	3.414	0.014790
31	MOLECULAR IMAGING AND BIOLOGY	2,543	3.341	0.005360
32	Journal of Cardiovascular Computed Tomography	1,711	3.316	0.004430
33	COMPUTERIZED MEDICAL IMAGING AND GRAPHICS	2,464	3.298	0.002990
34	AMERICAN JOURNAL OF NEURORADIOLOGY	23,231	3.256	0.028010
35	MEDICAL PHYSICS	26,715	3.177	0.030870
36	AMERICAN JOURNAL OF ROENTGENOLOGY	33,633	3.161	0.028540
37	CANCER IMAGING	1,406	3.153	0.002220
38	Quantitative Imaging in Medicine and Surgery	1,072	3.074	0.002420
39	PHYSICS IN MEDICINE AND BIOLOGY	27,458	3.030	0.031970
40	EJNMMI Research	1,408	3.000	0.004320
41	EUROPEAN JOURNAL OF RADIOLOGY	12,871	2.948	0.019480
42	Radiation Oncology	5,669	2.895	0.012980

2

Selected JCR Year: 2018; Selected Categories: "RADIOLOGY, NUCLEAR MEDICINE and MEDICAL IMAGING"

B₁ inhomogeneity correction of RARE MRI with transceive surface radiofrequency probes

Paula Ramos Delgado^{1,2}  | Andre Kuehne³ | João S. Periquito^{1,2}  | Jason M. Millward¹ |
Andreas Pohlmann¹ | Sonia Waiczies¹  | Thoralf Niendorf^{1,2,3}

¹Berlin Ultrahigh Field Facility (B.U.F.F.), Max Delbrück Center for Molecular Medicine in the Helmholtz Association, Berlin, Germany

²Experimental and Clinical Research Center, a joint cooperation between the Charité Medical Faculty and the Max Delbrück Center for Molecular Medicine in the Helmholtz Association, Berlin, Germany

³MRLTOOLS GmbH, Berlin, Germany

Correspondence

Paula Ramos Delgado, Berlin Ultrahigh Field Facility (B.U.F.F.), Max Delbrück Center for Molecular Medicine, Robert-Rössle-Str. 10, 13125 Berlin, Germany.
Email: Paula.Ramos@mdc-berlin.de

Funding information

Deutsche Forschungsgemeinschaft. Grant/Award Number: DFG-PO1869, DFG-WA2804 and Projektnummer 394046635, SFB 1365, RENOPROTECTION

Purpose: The use of surface radiofrequency (RF) coils is common practice to boost sensitivity in (pre)clinical MRI. The number of transceive surface RF coils is rapidly growing due to the surge in cryogenically cooled RF technology and ultrahigh-field MRI. Consequently, there is an increasing need for effective correction of the excitation field (B_1^+) inhomogeneity inherent in these coils. Retrospective B_1 correction permits quantitative MRI, but this usually requires a pulse sequence-specific analytical signal intensity (SI) equation. Such an equation is not available for fast spin-echo (Rapid Acquisition with Relaxation Enhancement, RARE) MRI. Here we present, test, and validate retrospective B_1 correction methods for RARE.

Methods: We implemented the commonly used *sensitivity correction* and developed an empirical *model-based* method and a *hybrid combination* of both. Tests and validations were performed with a cryogenically cooled RF probe and a single-loop RF coil. Accuracy of SI quantification and T_1 contrast were evaluated after correction.

Results: The three described correction methods achieved dramatic improvements in B_1 homogeneity and significantly improved SI quantification and T_1 contrast, with mean SI errors reduced from >40% to >10% following correction in all cases. Upon correction, images of phantoms and mouse heads demonstrated homogeneity comparable to that of images acquired with a volume resonator. This was quantified by SI profile, SI ratio (error < 10%), and percentage of integral uniformity (PIU > 80% in vivo and ex vivo compared to PIU > 87% with the reference RF coil).

Conclusion: This work demonstrates the efficacy of three B_1 correction methods tailored for transceive surface RF probes and RARE MRI. The corrected images are suitable for quantification and show comparable results between the three methods, opening the way for T_1 measurements and X-nuclei quantification using surface

This is an open access article under the terms of the Creative Commons Attribution-NonCommercial License, which permits use, distribution and reproduction in any medium, provided the original work is properly cited and is not used for commercial purposes.

© 2020 The Authors. *Magnetic Resonance in Medicine* published by Wiley Periodicals LLC on behalf of International Society for Magnetic Resonance in Medicine

transceiver RF coils. This approach is applicable to other MR techniques for which no analytical SI exists.

KEYWORDS

B_1 correction, B_1 inhomogeneity, MRI, RARE, signal intensity equation, transceiver surface RF coils

1 | INTRODUCTION

The ability of MRI to provide high spatial resolution images within short acquisition times is governed by the sensitivity conundrum, which balances the constraints of signal-to-noise (SNR), image contrast, spatial resolution, and temporal resolution.¹⁻⁵ Numerous approaches have been developed to improve SNR per scan time from the development of novel software-driven approaches (eg, parallel imaging,^{6,7} compressed sensing⁸), to hardware improvements, including higher magnetic field strengths (B_0)⁹⁻¹¹ and the optimization of radiofrequency (RF) technology. The use of surface RF coils is common practice to boost sensitivity¹² in (pre)clinical MRI, predominantly with a receive-only RF coil design in combination with a volume RF coil used for excitation.¹³ The use of transceiver (transmit-receive, TxRx) surface RF coils is increasing, in particular in human MRI at ultrahigh fields¹⁴⁻²² where large volume body RF coils are not used for signal excitation and are not provided with ultrahigh field-MR scanners.

In preclinical research, the use of transceiver RF configurations has been dominated by cryogenically cooled RF probes (CRP) that provide significant SNR gains.²³⁻²⁵ CRPs are sometimes also available as decoupled Rx-only configurations in combination with a room-temperature (RT) volume resonator for RF excitation, but are not as common as the Tx/Rx configuration.²⁶ By reducing thermal noise in the receiver circuitry (RF probe and preamplifier), SNR can be enhanced by a factor of up to 3-4 compared to conventional RT RF coils.²³ The SNR gain of a CRP can be exploited to increase spatial resolution, to reduce scan time, or to lower detection limits, especially for X-nuclei MRI.

A constraint of TxRx surface RF coil technology is the strong intrinsic spatial gradient (inhomogeneity) in both excitation (B_1^+) field and coil sensitivity (B_1^-).^{12,13} Although the latter can be easily corrected,²⁷⁻³⁴ non-uniform B_1^+ fields induce significant spatial variations in the excitation flip angle (FA), with the effective FA decreasing with increasing distance from the RF coil surface. The resulting B_1^+ inhomogeneities are more pronounced at higher field strengths.^{35,36} This adverse effect reduces image homogeneity and affects the T_1 image contrast, representing a major challenge for applications for which absolute signal intensities are needed, such as T_1 mapping^{37,38} and quantification techniques in X-nuclei MRI.^{39,40}

Although partial mitigation of B_1^+ inhomogeneity can be achieved with adiabatic pulses,^{41,42} dielectric materials,⁴³⁻⁴⁶ or B_1^+ shimming,⁴⁷⁻⁴⁹ retrospective B_1^+ correction approaches

are most commonly used to achieve signal uniformity.⁵⁰⁻⁵⁶ First, the actual FA is measured using magnitude- or phase-based B_1^+ mapping techniques, such as the double angle method,^{57,58} the phase sensitive technique,⁵⁹ the actual FA method,⁶⁰ or any of their improvements.⁶¹⁻⁶³ Then, an analytical description of the signal intensity (SI) dependency on the FA for the RF pulse sequence (SI equation)⁵⁰⁻⁵⁴ or numerical simulations^{55,56} are used to perform the SI correction.

Retrospective B_1^+ correction has been successfully applied to gradient echo imaging techniques such as fast low angle shot^{50,51} or steady-state free precession,⁵⁴ which are inherently less sensitive to RF inhomogeneity⁶⁴ and for which SI equations are given.⁶⁵ Retrospective B_1^+ correction was also reported for spin-echo imaging methods.^{52,53} For fast spin-echo techniques such as Rapid Acquisition with Relaxation Enhancement (RARE)⁶⁶ there is no exact analytical SI equation.^{67,68} This extends to pulse sequences employing simultaneous multislice parallel imaging,⁶⁹ non-Cartesian trajectories,⁷⁰⁻⁷² variable FA 3D turbo spin-echo,⁷³ water-fat separation using Dixon approaches,⁷⁴ and hybrid imaging techniques like half-Fourier single shot turbo spin-echo/gradient and spin-echo/turboGRASE (HASTE/GRASE/TGSE).⁷⁵ Other complex techniques with no SI equation include those derived from ultrashort echo time⁷⁶ or echo-planar imaging (EPI).⁷⁷ As a consequence, retrospective B_1^+ correction for these MRI techniques demands novel solutions.

To address this need, we developed, implemented, and applied three B_1 correction approaches for RARE MRI with transceiver surface RF probes with the goal to reduce errors to less than 10% for SI quantification and for T_1 contrast. All three methods were applied and validated in test phantoms and mouse brains, in vivo and ex vivo. For performance evaluation, the corrected images were benchmarked against reference images obtained with a uniform TxRx volume resonator. The starting point was the commonly used *sensitivity correction*²⁷ that uses a uniform phantom image to correct for B_1^- inhomogeneities. This method does not take spatial FA variations and T_1 relaxation times into account. Given this limitation and the unavailability of an analytical SI equation for fast spin-echo imaging, we modelled the SI of RARE as a function of FA and T_1 based on empirical measurements obtained through MR experiments. This *model-based correction* uses the SI model to correct B_1^+ , followed by a B_1^- correction. We also implemented a *hybrid correction* using a combination of the *model-based* and *sensitivity correction* approaches. These methods are valuable not only for conventional ^1H -MRI when

accurate FAs are needed (eg, for well-defined T_1 contrasts), but also in X-nuclei MRI, for which absolute SI is essential for signal quantification.

2 | METHODS

The MR hardware, sample preparation, and measurements are summarized in Table 1.

2.1 | MR hardware

All experiments were performed on a 9.4 T small animal MR scanner (BioSpec 94/20, Bruker BioSpin, Ettlingen, Germany) operating at 400 MHz (^1H).

For creating reference images, we chose RF coils with approximately uniform excitation and reception fields:

- Small reference RF coil: in-house built volume resonator tailored for mouse head imaging⁷⁸ (inner diameter [ID] = 18.4 mm).
- Large reference RF coil: rat body linear volume resonator (Bruker BioSpin) with an ID = 72 mm.

The correction methods were applied, evaluated, and validated for 2 transceive surface RF coils:

- Cryocooled surface RF coil (CRP): 2-element transceive RF probe (CryoProbe[®], Bruker BioSpin) operating in quadrature mode with an ID = 20 mm and a saddle-shaped ceramic surface.
- RT surface RF coil: planar transceive single loop (ID = 20 mm) surface RF coil (Bruker BioSpin).

2.2 | Sample and animal preparation

To characterize the excitation and receive fields of the transceive surface RF coils (B_1 mapping), we used samples that ensured full field of view coverage and had low T_1 values ($T_1 \approx 300$ ms) to reduce the needed TR ($\text{TR} > 5 \cdot T_1$) in our measurements:

- Cylindrical uniform phantom with low T_1 : 15-mL tube (ID = 14.6 mm, length = 120 mm; Thermo Fisher Scientific, Waltham, Massachusetts) filled with a mixture of water and copper sulfate (Carl Roth GmbH & Co. KG, Karlsruhe, Germany).
- Rectangular uniform phantom with low T_1 : 50-mL cell culture flask ($(79.7 \times 42.6 \times 25)$ mm³; Fisher Scientific) filled with a doped solution of water.

Samples with different T_1 (NMR tubes, Thermo Fisher Scientific) filled with aqueous solutions of gadolinium (Magnevist[®] 0.5 mmol/ml; Bayer Vital, Leverkusen, Germany) at different concentrations (0–0.5 mM) yielding T_1 between 190 and 2871 ms were used to produce the RARE SI models.

The test phantoms used for correction and evaluation of the B_1 correction methods were:

- Cylindrical uniform phantom: containing water doped with gadolinium embedded in a 15-mL tube ($T_1 \approx 800$ ms).
- Ex vivo mouse: the central nervous system of a SJL/J female mouse, perfused with a phosphate-buffered saline (Biochrom GmbH, Berlin, Germany), fixed in paraformaldehyde (PFA; Santa Cruz Biotechnology, Inc., Dallas, Texas), and placed into a 15-mL tube filled with 4% PFA.
- In vivo mouse: a healthy SJL/J mouse anesthetized with 2.7% isoflurane and stabilized with 1.6% during scanning. Heart rate, respiration rate, and temperature were monitored and kept constant during the examinations.
- Rectangular uniform phantoms: four 50-mL cell culture flasks filled with solutions of two different ^1H -atom concentrations: 100% water, 50% water and 50% deuterium oxide (Sigma-Aldrich, Saint Louis, Missouri). Gadolinium was added to the mixtures to achieve two different T_1 values (490 and 1525 ms).

All animal experiments were approved by the Animal Welfare Department of the LAGeSo State Office of Health and Social Affairs in Berlin and in accordance with international guidelines on reduction of discomfort (86/609/EEC).

2.3 | MR measurements

To characterize the B_1 fields of both transceive surface RF coils we used:

- FA mapping: fast low angle shot (FLASH) measurements with nominal excitation FAs of $60^\circ/120^\circ$ (RT) and $60^\circ/120^\circ/240^\circ$ (CRP) with echo time/pulse repetition time (TE/TR) = 2.49/2000 ms, matrix = 128×128 , 3 slices with a gap of 0.5 mm and a thickness of 2 mm each, $\text{TA} = 1\text{h}30$. We used a field of view = (25×25) mm² for the CRP and field of view = (35×35) mm² for RT.
- B_1^- mapping: FLASH measurement with a nominal FA of 5° (same parameters as above).

B_1 field characterization can be performed prior to or after the image acquisition and does not entail extra acquisition time on the day of image acquisition, for example, in vivo scans.

TABLE 1 Detailed overview of measurements

Purpose	MR protocol	RF coil type	RF coil	Sample(s)	Acq. time
Test images	T_1 w-RARE (with flipback)	Surface TxRx	CRP	Cylindrical uniform phantom	60 min
				Ex vivo mouse	60 min
				In vivo mouse	30 min
Validation images	T_1 w-RARE (with and w/o flipback)	Surface TxRx	RT	Rectangular uniform phantoms	30 min
Sensitivity correction					
Uniform phantom images	T_1 w-RARE (with and w/o flipback)	Surface TxRx	CRP	Cylindrical uniform phantom with low T_1	60 min
			RT	Rectangular uniform phantom with low T_1	30 min
Model-based correction					
Mapping of FA and B_1	FLASH	Surface TxRx	CRP	Cylindrical uniform phantom with low T_1	90 min per FA
			RT	Rectangular uniform phantom with low T_1	30 min per FA
RARE SI modelling	T_1 w-RARE (with and w/o flipback)	Volume TxRx	Small reference RF coil	Samples with different T_1	5 m 40 s per FA
T_1 mapping for modelling	RARE with variable TR	Volume TxRx	Small reference RF coil	Samples with different T_1	90 min
T_1 mapping for test images	RARE with variable TR	Volume TxRx	Small reference RF coil	Cylindrical uniform phantom	100 min
				Ex vivo mouse	30 min
				In vivo mouse	55 min
T_1 mapping for validation images	RARE with variable TR	Volume TxRx	Large reference RF coil	Rectangular uniform phantoms	30 min
Hybrid correction					
Mapping of FA and B_1	FLASH	Surface TxRx	CRP	Cylindrical uniform phantom with low T_1	90 min per FA
			RT	Rectangular uniform phantom with low T_1	30 min per FA
RARE SI modelling	T_1 w-RARE (with and w/o flipback)	Volume TxRx	Small reference RF coil	Samples with different T_1	5 m 40 s per FA
T_1 mapping for modeling	RARE with variable TR	Volume TxRx	Small reference RF coil	Samples with different T_1	90 min
T_1 mapping for test images	RARE with variable TR	Volume TxRx	Small reference RF coil	Cylindrical uniform phantom	100 min
				Ex vivo mouse	30 min
				In vivo mouse	55 min
T_1 mapping for validation images	RARE with variable TR	Volume TxRx	Large reference RF coil	Rectangular uniform phantoms	30 min
T_1 mapping uniform phantom	RARE with variable TR	Volume TxRx	Small reference RF coil	Cylindrical uniform phantom with low T_1	100 min
T_1 mapping uniform phantom	RARE with variable TR	Volume TxRx	Large reference RF coil	Rectangular uniform phantom with low T_1	30 min

CRP, cryogenically cooled radiofrequency probes; FA, flip angle; FLASH, fast low angle shot; RARE, Rapid Acquisition with Relaxation Enhancement; RT, room temperature; TxRx, transmit-receive.

To compute the models, we performed RARE measurements both with and without flipback and studied the effect of the extra pulse (which restores longitudinal magnetization, improving SNR) on the SI:

- T_1 -weighted (T_1 w-) RARE scans ($TE/TR = 2.49/1000$ ms, echo train length (ETL) = 8, receiver bandwidth = 50 kHz, centric phase encoding, field of view = (25×25) mm², matrix = 128×128 , 3 slices of 2 mm thickness,

TA = 5m40s). Thirty-five reference RF powers were used to vary the excitation FA in 5° increments, between 5° and 160° (flipback) and between 5° and 110° (without flipback).

- T₁ maps of all phantoms (RARE with variable TR (120-15 000 ms); ETL = 2, linear phase encoding, other parameters same as RARE scan).

T₁w-RARE images were acquired using the same parameters as above with flipback (CRP) and with/without flipback (RT) for validation purposes. Corresponding T₁ maps for all samples were measured using RARE with TR ranging from 150 to 14500 ms.

All reference RF power adjustments were performed on a 2-mm slice located parallel and close to the RF coil surface.

RARE modeling can be equally performed prior to or after the image acquisition and does not entail extra acquisition time on the day of image acquisition, for example, in vivo scans.

This straight-forward method only requires a uniform phantom image to correct for the B₁⁻ inhomogeneities.^{27,28} The following steps were performed (Figure 1A):

- MRI study. Images (sample and uniform phantom) were acquired.
- Correction factor computation. We normalized and calculated the inverse of the uniform phantom image.
- Sensitivity correction. We multiplied the uncorrected image by the estimated correction factor to correct for the B₁⁻ inhomogeneities.

This method requires neither the characterization of the transceive RF coil used, nor the calculation of a RARE SI model and it is, therefore, directly applicable after image acquisition with little post-processing.

2.4 | Approach 1: Sensitivity correction

All post-processing was performed using customized software developed in MATLAB (MathWorks Inc., Natick, Massachusetts).

2.5 | Approach 2: Model-based correction

Figure 2 shows the workflow of the model-based correction, consisting of the following steps, starting with the quantification of the B₁ inhomogeneities:

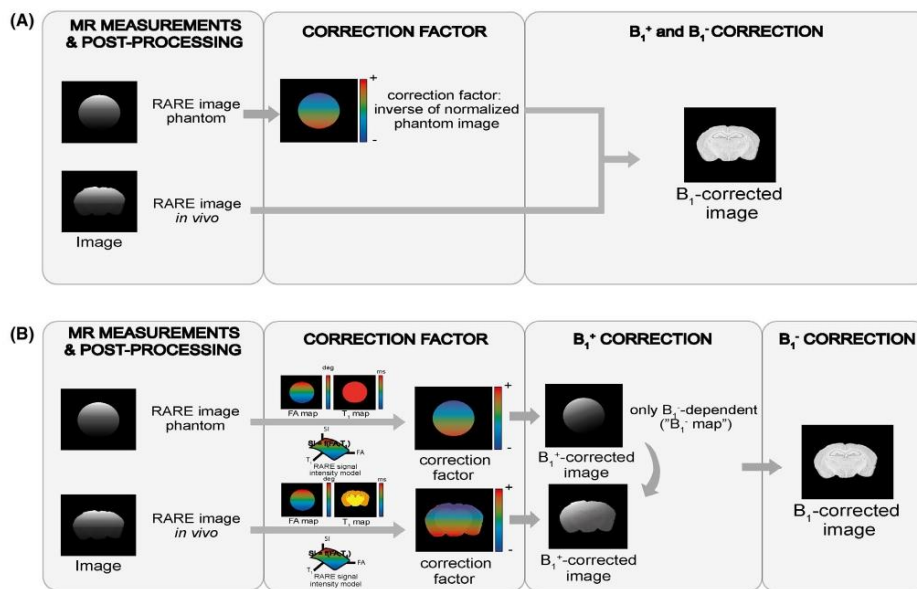


FIGURE 1 Workflows of (A) sensitivity correction and (B) hybrid B₁ correction. The sensitivity correction merely requires dividing the sample image by that of a normalized uniform phantom. The hybrid method combined the model-based approach to perform a B₁⁺ correction on the sample image and a uniform phantom image. The latter is then used to perform a B₁⁻ correction using the sensitivity correction method

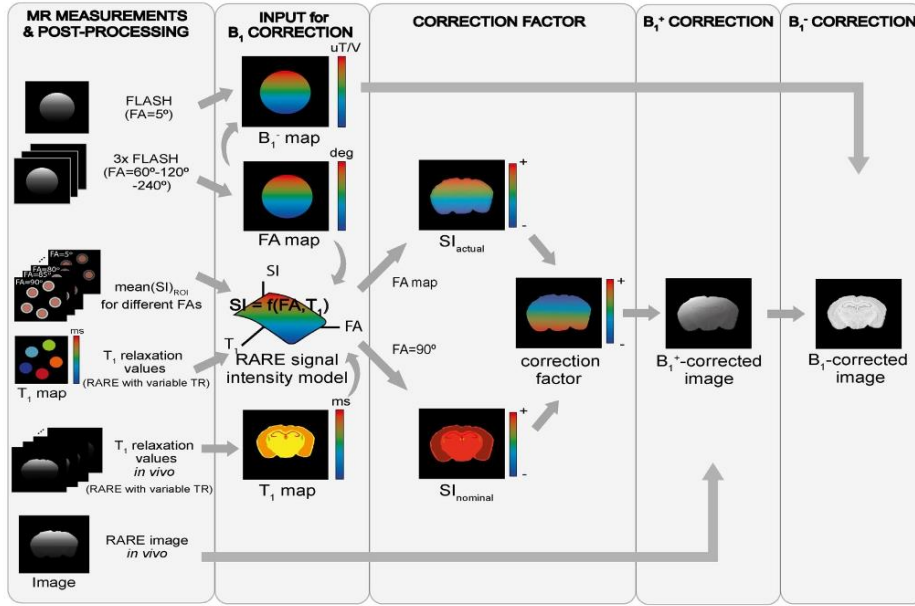


FIGURE 2 Workflow of model-based B_1 correction. The necessary images and maps to be acquired are described in MR Measurements & Post-processing column. Then the flip angle (FA) and sensitivity (B_1^-) maps were calculated using the double angle method and the low FA approximation, respectively. The Rapid Acquisition with Relaxation Enhancement (RARE) signal intensity model was derived from a 2D fit of the signal intensities measured for different FAs and T_1 relaxation times using a volume resonator. The B_1^+ correction factor was computed pixel-wise for the actual FA and T_1 using the RARE signal intensity model. Applying this correction factor and the B_1^- map derived correction factor yielded the final B_1 corrected image

- RF coil characterization. *FA maps* were calculated using the double angle method.^{57,58} To increase the SNR distal to the CRP we added a measurement at a higher FA and merged the 60°/120° and 120°/240° maps using an SNR cutoff. All maps were denoised using a polynomial fitting tool (*polyfit*,⁷⁹ 10th-order polynomials).

The *transmit field* (B_1^+) maps were computed using:

$$FA = \gamma \cdot B_1^+ \cdot \tau$$

with γ being the gyromagnetic ratio ($\gamma = 267.522 \cdot 10^6 \text{ rad s}^{-1} \text{ T}^{-1}$ for ^1H) and τ the pulse length of a rectangular RF pulse. Because calculated RF pulses were used, each one has a complex shape tailored to the sequence parameters. We therefore approximated the RF pulse length τ using the product of the RF pulse duration, the area under the RF pulse (S_{int}), and the related voltage (V):

$$B_1^+ = \frac{FA \cdot \pi/180}{\gamma \cdot t_p \cdot S_{\text{int}} \cdot V}$$

- The *RF coil sensitivity maps* (B_1^-) were calculated using the low FA approximation^{80,81}:

$$SI_{\text{lowFA}} \propto |B_1^+| \cdot |B_1^-|$$

where SI_{lowFA} was the 5° fast low angle shot measurement. The low FA image and B_1^+ map were normalized by their respective maximum values and B_1^- calculated as:

$$B_1^- / \max(B_1^-) \propto \frac{B_1^+ / \max(B_1^+)}{SI_{\text{lowFA}} / \max(SI_{\text{lowFA}})}$$

Ultimately, the B_1^- map was denoised using a 10th-order polynomial fit.

- Modeling of the RARE SI equation. The relationship between SI, FA, and T_1 was estimated using experimental data and a fitting tool:

Data analysis: Images were denoised using a spatially adaptive non local means filter,⁸² and T_1 maps computed

by fitting $S = S_0(1 - \exp(-TR/T_1))$ to the SIs using in-house developed software in MATLAB. We assumed $SI(FA = 0^\circ) = 0$ for all T_1 . For each T_1 sample, a circular region of interest (ROI) was drawn to extract average SI and T_1 values from the images and maps respectively.

RARE modeling: To model the $SI = f(FA, T_1)$ relationship a 7th-order 2D polynomial was fitted to the experimental data using MATLAB's *polyfitn*⁷⁹ function. This was the lowest polynomial order that gave an $R^2 > 0.99$ and a faithful representation of the measured data.

- MRI study. Images and corresponding T_1 maps of the test samples were acquired.
- Retrospective correction. All images and maps ($B_1^+/B_1^-/T_1$) were spatially aligned, either by careful slice planning or by image registration.

The B_1^+ -correction factor (f_{corr}) was calculated as the modeled RARE SI for a perfect 90° excitation ($SI_{nominal}$) divided by the modeled RARE SI for the actual excitation FA (SI_{actual}) obtained from the FA map:

$$f_{corr} = \frac{SI_{nominal}}{SI_{actual}}$$

Applying this correction factor yielded a B_1^+ -corrected image:

$$image_{B_1+corr} = image \cdot f_{corr}$$

In the few cases where the algorithm produced negative values (low-SNR regions), the correction factor was set to zero.

Dividing this B_1^+ -corrected image by the B_1^- map produced the final B_1 -corrected image:

$$image_{corr} = image_{B_1+corr} / B_1^-$$

2.6 | Approach 3: Hybrid correction

This method combines the sensitivity and model-based correction (workflow in Figure 1B), and involves:

- RF coil characterization (as in *Model-based Correction*).
- Modeling of the RARE SI equation (as in *Model-based Correction*).
- MRI study. Images and T_1 maps of the samples and of a uniform phantom were measured.
- Model-based B_1^+ correction (as in *Model-based Correction*) was performed on the sample and uniform phantom image.

- B_1^- correction (as in *Sensitivity Correction*). The inverse of the B_1^+ -corrected uniform phantom image was applied as the B_1^- correction factor to the B_1^+ -corrected sample image.

Both the model-based and the hybrid correction methods need a prior/posterior characterization of the transceive RF coil used and the calculation of a RARE SI model. The post-processing needed is rather simple in both cases.

2.7 | Correction method evaluation and validation

The presented B_1 correction techniques were validated using the following methods:

2.7.1 | Central profile plots

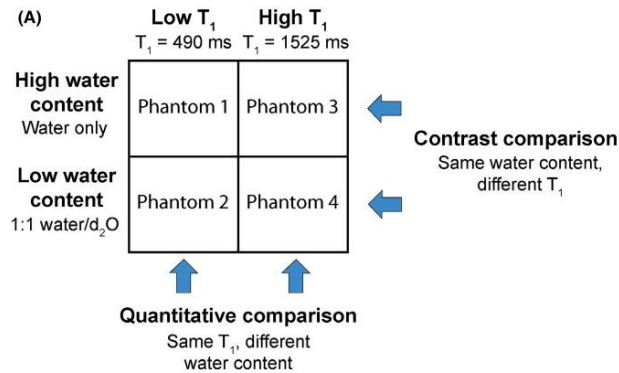
The SI profile along a central line perpendicular to the RF coil surface was plotted against distance to the RF coil surface. Seven pixels across the width of the line were averaged, and the SIs were normalized to [0,1] to allow a better comparison. A quantitative comparison was performed by calculating the root-mean-square-error (RMSE) between each profile and the reference. Each profile was scaled to minimize the RMSE against the reference, in order to compensate for the arbitrary scaling and to provide a fair comparison.

2.7.2 | Image homogeneity assessment

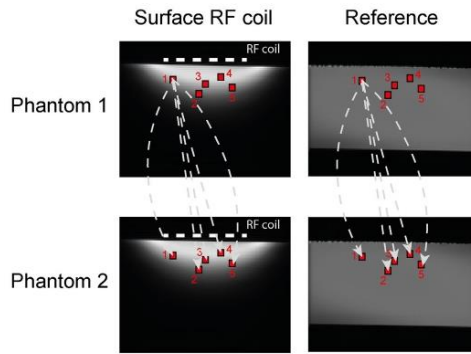
To quantitatively assess the uniformity of the corrected images, the *percentage of integral uniformity* (PIU)⁸³ was computed for several ROIs of different sizes. A PIU of 100% represents perfect image homogeneity. In the uniform phantom, we defined 5 internally tangential circular regions of interest (ROIs) with increasing diameter on the central vertical line. For the brain images (ex vivo, in vivo), we manually outlined the cortex and basal ganglia/thalamus (left and right), achieving 3 ROIs.

2.7.3 | T_1 -contrast and quantification performance

We used the experimental setup (Figure 3A) to compare substances with different water content (100% or 50%, respectively) and different T_1 relaxation times (490 or 1525 ms, respectively). All acquired images with and without flipback were corrected using the three B_1 correction methods. Five ROIs were drawn at



(B) Quantitative comparison for low T₁ (example):



pseudo-randomized positions (Figure 3B) on all sets of images (three corrections, original and reference) for all flasks. For each of the flask image pairs described in Figure 3A, mean SI ratios were calculated using all possible ROI combinations for all sets. Relative ratio errors were computed:

$$\text{Ratio error} = \frac{\text{abs}(\overline{\text{SI}}_{\text{reference}} - \overline{\text{SI}}_{\text{corrected}})}{\overline{\text{SI}}_{\text{reference}}} * 100(\%)$$

With $\overline{\text{SI}}_{\text{reference}}$ being the mean SI ratio computed using all ROI combinations on the reference image pairs, and $\overline{\text{SI}}_{\text{corrected}}$ being that achieved using the corrected image pairs. Finally, the mean error and mean SD were calculated. An example of the workflow is shown in Figure 3B.

Statistical analysis. A nonparametric 1-way analysis of variance Friedman repeated measures test was performed (mean errors on the original data did not have a Gaussian distribution) followed by Dunn's test where all corrections were compared to the original data (*P* values < .05 were considered

FIGURE 3 Illustrations of validation methods. (A) To evaluate the performance of the correction methods (sensitivity, model based, and hybrid), 4 phantoms with different water content and T₁ relaxation times were prepared. The quantitative assessment compared flasks with different water content for both low and high T₁ values. Similarly, contrast was evaluated by comparing phantoms with different T₁ values at low and high water content. (B) shows the region of interest (ROI) placement and depicts for one selected ROI the ratios that were calculated. In this manner we calculated the ratios for all possible ROI combinations in the corrected, original and reference images. The mean relative errors of these ratios with regard to those obtained in the reference served as quantitative measure for the validation

significant). All statistical assessments were performed using GraphPad Prism 5 (GraphPad Software, La Jolla, California).

3 | RESULTS

3.1 | RF coil characterization

The maps of the receive field (B_1^-) (Figure 4A) and transmit field (B_1^+ , here as FA) relative to a 90° excitation FA (Figure 4B) demonstrate the spatially varying sensitivity and FA for the CRP. A closer look at the vertical midline profile reveals a strong deviation from the target of FA = 90° (nominal FA) with increasing distance from the surface of the CRP (Figure 4C). These field maps show the typical inhomogeneity inherent to transceive surface RF coils, which was very similar in the B_1^+ and B_1^- maps and FA profiles for the single loop RF coil (Figure 4D-F). The minor deviation of the FA profiles at 20-30 mm from the coil surface (in gray) reflects a mathematical artifact of the polynomial fit at low-SNR regions

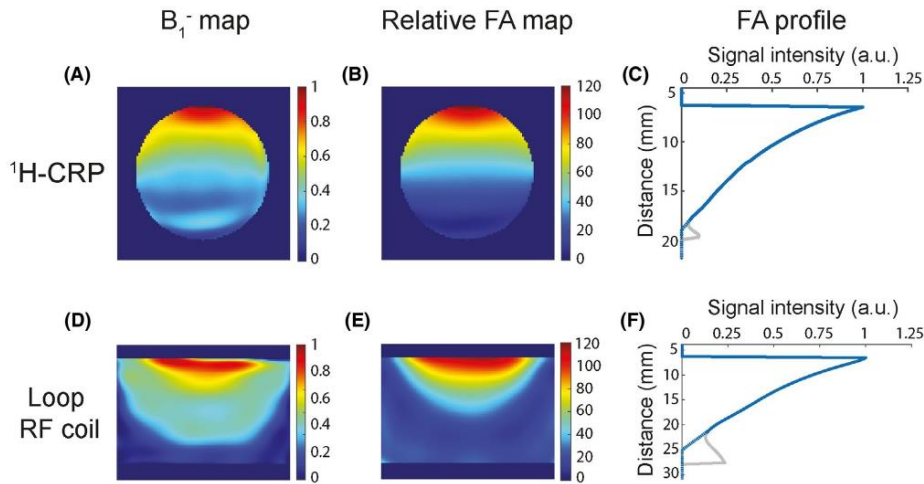


FIGURE 4 Sensitivity maps and transmission fields of the two transceive (TxRx) surface radiofrequency (RF) coils used for testing and validation. (A,D) Axial view of the computed sensitivity (B_1^+) maps for a uniform phantom placed close to the RF coil surface. (B,E) Corresponding flip angle (FA) maps relative to a 90° excitation. (C,F) Normalized central profile plots of the FA along the vertical axis, which reveal a strong decay with increasing distance to the RF coil surfaces. The gray lines depict the true calculated data misestimated by the polynomial fit at low signal-to-noise ratio regions far away from the RF coil surface; the assumed true value is shown by the blue dotted lines

far from the RF coil surface. The assumed correct value is depicted by the dashed blue line.

3.2 | Modeling of the RARE SI equation

The RARE SI dependency on FA and T_1 ($SI = f(FA, T_1)$) was modeled by fitting a polynomial to the experimental data acquired with these parameters, either incorporating a flip-back pulse to restore longitudinal magnetization and hence improve SNR (Figure 5A-C), or excluding flipback to allow natural relaxation (Figure 5D-F). The fitted 3D-surfaces are shown in Figure 5A,D. Two-dimensional projections of the RARE models show the relationships between SI and T_1 for several FA values (Figure 5B,E) and between SI and FA for several T_1 values (Figure 5C,F). As expected, the fitted SI data predicts lower SI with increasing T_1 and maximal SI for FAs around 90° . The surface fits modeled the experimental data well ($R^2 = 0.997$ in both cases).

3.3 | Correction method evaluation and validation

We acquired T_1 maps (needed for B_1^+ correction) and reference images of a uniform phantom, an ex vivo mouse phantom, and an in vivo mouse brain using a volume resonator

(Figure 6A-B). The original uncorrected CRP images show the strong spatial SI gradient typical of transceive surface RF coils (Figure 6C). The results obtained with the three B_1 correction methods are shown in Figure 6D-F. The strong spatial SI gradient present in the CRP images was removed by all B_1 correction methods, yielding a uniform SI throughout the entire field of view for all investigated samples, including the in vivo mouse head. With the *sensitivity* and *model-based corrections* we observed an overshoot in SI in some regions, particularly distal to the CRP. This was due to a combination of increasing inaccuracies in the FA and SI data at low SNR. This overshoot in SI was resolved by combining both methods in the hybrid correction approach.

3.3.1 | Central profile plots (CRP)

To quantitatively assess the correction of the image inhomogeneity, we plotted normalized vertical SI profiles (Figure 7A-C). For all three approaches, the corrected SI profiles showed close correspondence with the reference RF coil (plotted as a surface in green). From these profiles one can determine how far away from the RF coil it is still viable to perform B_1 correction. This depends on the specific scanning parameters and the dimensions of the RF coil; here this distance was approximately 17 mm (for a nominal FA of 90° , an actual FA of up to 8° could be

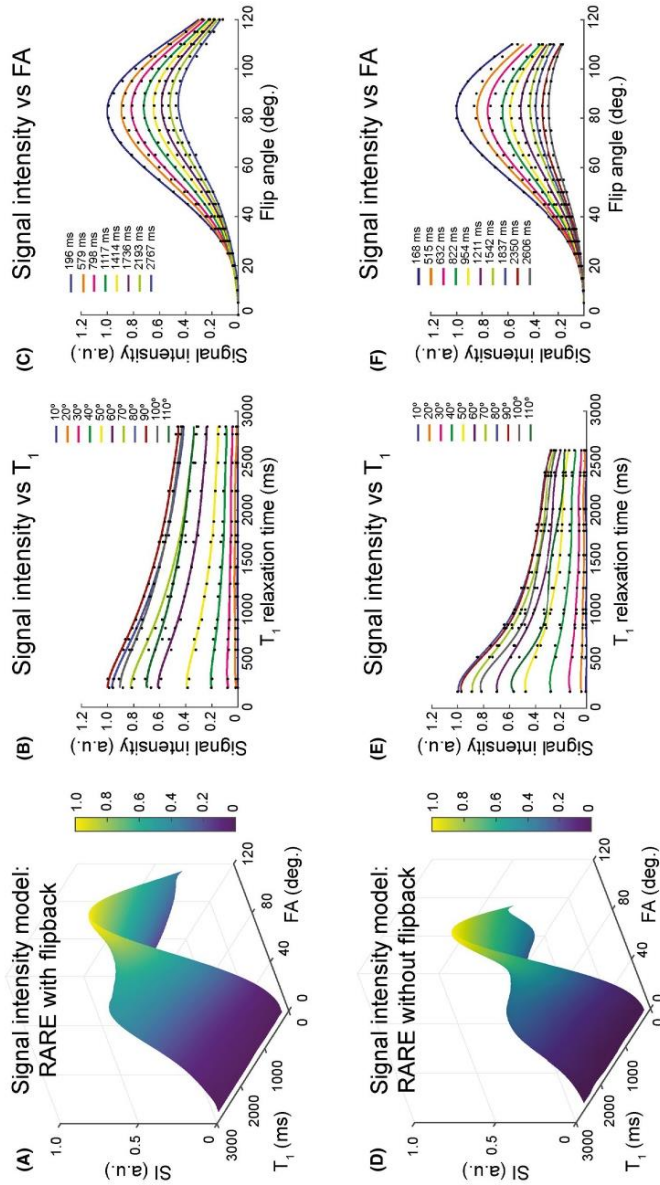


FIGURE 5 Signal intensity (SI) models for Rapid Acquisition with Relaxation Enhancement (RARE) with and without flipback. (A,D) 3D-plots of the modelled RARE signal intensity (SI) as a function of the T₁ relaxation time and flip angle (FA) with and without flipback, respectively (R² = 0.997 for both). (B,E) show the SI vs FA projection in both models, whereas (C,F) depict the SI vs T₁ projection. Selected FA and T₁ values are plotted to demonstrate the fidelity of the experimental data and the model. Each colored line depicts a different T₁ and FA, respectively. The dots represent the measured data points

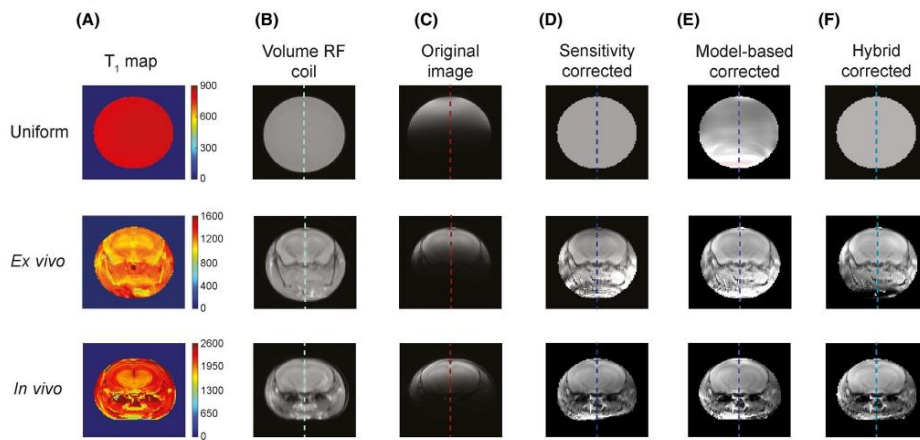


FIGURE 6 B_1 correction for cryogenically cooled radiofrequency probes (CRP) images of a uniform phantom, an ex vivo phantom and a living mouse. From left to right, the columns show (A) the acquired T_1 map (reference coil), (B) the reference image, (C) the original CRP image, (D-F) the corrected images. A comparison of the original images with the reference images demonstrates the need of B_1 correction. Quantification is severely hampered by the adverse signal intensity gradient. The corrected images show a remarkably improved homogeneity. All three correction methods performed well, with only slight differences between the results. Masks containing minor errors in the correction are overlaid and shown in light red

corrected). For our experimental setup, the region beyond 17 mm showed increasing inaccuracies in the field maps and SI measurements, leading to unacceptable errors in all corrected images.

Quantitative examination revealed that all correction methods considerably reduced the RMSE computed on the profiles to a maximum of 0.18 (uniform), 0.12 (ex vivo) and 0.26 (in vivo), with respect to the reference. For the uniform phantom, the *sensitivity* and *hybrid approaches* performed equally well (0.11). For the ex vivo phantom the *sensitivity* and *model-based correction* performed similarly (0.11). In vivo, the *sensitivity correction* achieved the best result (0.21). In comparison, the uncorrected profiles revealed an average RMSE of 0.53 ± 0.07 for all test phantoms.

3.3.2 | Image homogeneity assessment (CRP)

For the uniform phantom, we found the calculated PIU (Figure 7D-F) to be 95.7% within the largest ROI using the volume resonator, indicating no significant inhomogeneities across the image, as expected. Conversely, a PIU of 0.9% was obtained within the same ROI on the uncorrected image. The PIU degradation scaled with increasing ROI diameter. After correction, the *model-based approach* showed a PIU of 65% on the fourth ROI (up to a distance of 16.2 mm from the RF coil surface). Beyond that distance, the observed overshoots

confounded the PIU, which decreased to 0% in the largest ROI.

For the mouse brain images the PIUs showed the expected high homogeneity for the reference RF coil: ex vivo $87.0 \pm 4.4\%$ and in vivo $87.7 \pm 9.1\%$. The original surface RF coil images displayed substantial inhomogeneities: averages of $35.4 \pm 9.2\%$ ex vivo and $33.2 \pm 11.8\%$ in vivo. A significant improvement in image homogeneity was achieved with all three correction methods, both in vivo and ex vivo. The *model-based method* performed best on average ($85.0 \pm 3.8\%$ ex vivo and $80.5 \pm 11.3\%$ in vivo), closely followed by the *hybrid* ($81.6 \pm 6.9\%$ ex vivo and $79.7 \pm 11.2\%$ in vivo) and *sensitivity* ($80.8 \pm 5.7\%$ ex vivo and $76.5 \pm 10.3\%$ in vivo) corrections.

3.3.3 | T_1 -contrast and quantification performance (RT)

We studied the errors in SI ratios between several fixed locations for all four phantoms, comparing original (uncorrected) RARE images and their three corrections, relative to the ground truth (reference images). These validation assessments were performed for RARE without flipback (Figure 8) and with flipback (Figure 9). The box plots (whiskers at 5-95 percentile) depict the mean errors for quantification at low and high T_1 relaxation times, and for T_1 contrast measurements with low and high proton

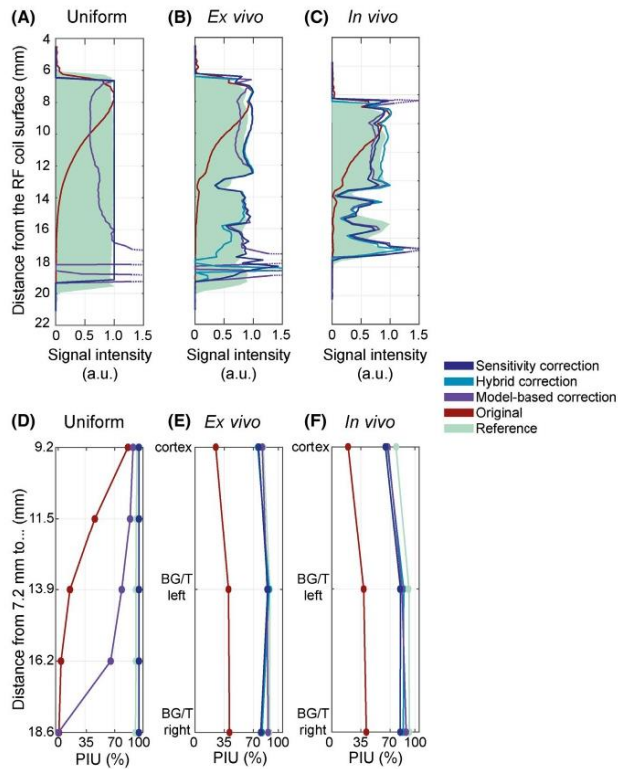


FIGURE 7 Normalized signal intensity profiles perpendicular to the radiofrequency (RF) coil surface and percentage of integral uniformities (PIU) for the exemplary images shown in Figure 5: (A-D) uniform phantom, (B-E) ex vivo, and (C-F) in vivo, using 5 internally tangent circular regions of interest (ROIs) with increasing diameter (uniform) or anatomical regions (ex vivo, in vivo: cortex and basal ganglia/thalamus, BG/T). The corrected profiles demonstrate a striking increase in image homogeneity and show the same trends as those of the reference coil. In all three phantoms the calculated root-mean-square-errors (RMSEs) of the corrected profiles reveal a high resemblance to the reference. The PIU plots indicate a significant improvement in image homogeneity after correction

density. Errors below 10% (dashed line) were considered acceptable.

Correction of RARE MR images without flipback (Figure 8): All correction methods reduced the errors to less than 10% for both quantification and contrast, contrary to uncorrected images that showed substantial errors (41-45%) and variabilities (37-42%). None of the calculated mean errors reached a value >8.3% after correction.

The *sensitivity correction* performed best when calculating water content proportions at low T_1 values ($5.0 \pm 2.9\%$), followed closely by the *hybrid* ($6.0 \pm 2.7\%$) and *model-based* ($6.6 \pm 4.5\%$) methods. All three methods behaved similarly for higher T_1 values, with mean errors of approximately 8% (*sensitivity* $8.1 \pm 2.9\%$, *model-based* $8.3 \pm 5.9\%$, *hybrid* $8.1 \pm 3.3\%$). All correction methods improved quantification significantly (P value < .0001) when compared to the original data.

When measuring T_1 contrast, the *hybrid method* performed best for both water content phantoms ($2.4 \pm 1.7\%$ high, $4.7 \pm 3.8\%$ low). The *sensitivity correction* method performed better than the *model-based method* for the high water content phantom ($3.5 \pm 2.5\%$ vs. $6.2 \pm 5.5\%$). However, for the low water content comparison,

the *model-based correction* method performed better than the *sensitivity correction* ($5.2 \pm 3.9\%$ vs. $6.1 \pm 3.1\%$). Similarly, the three described correction methods significantly improved T_1 contrast, when compared to the original data (P value < .0001).

Correction of RARE MR images with flipback (Figure 9): In general, all correction methods performed worse when flipback was enabled in RARE measurements, compared to RARE without flipback. The errors without correction were comparable to the case without the flipback option (40-58%). Their variabilities, however, were spread along a wider range (40-62%).

For quantification, the correction methods performed worse at low T_1 relaxation times (overall about 10%: *sensitivity* $11.0 \pm 7.6\%$, *model-based* $10.7 \pm 7.9\%$, *hybrid* $12.2 \pm 8.6\%$) than at higher ones (*sensitivity* $4.8 \pm 4.0\%$, *model-based* $11.4 \pm 10.1\%$, *hybrid* $7.2 \pm 6.0\%$). All correction methods significantly improved quantification when compared to the original data (P < .0001).

T_1 contrast accuracy was considerably reduced when using flipback during the measurements, with errors approaching 20-30% for high water content. The *sensitivity correction*

RARE without flipback

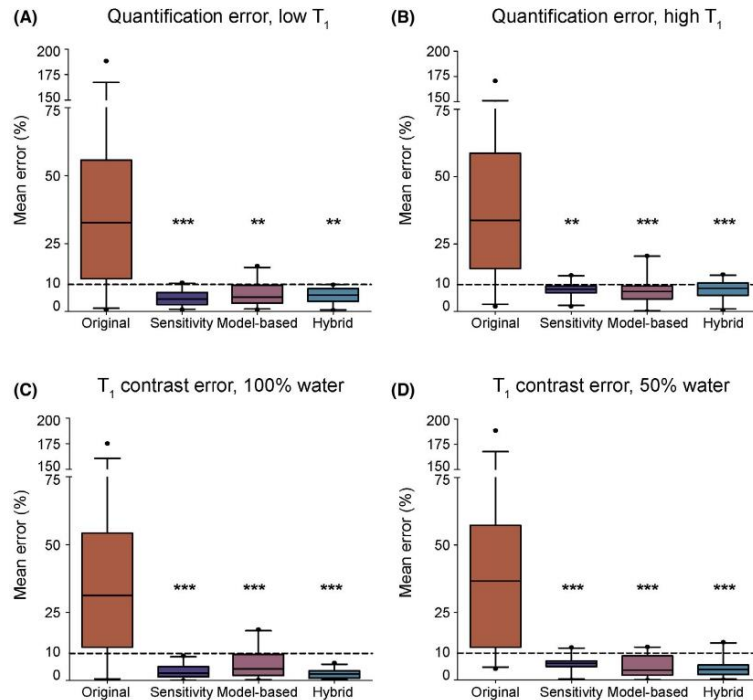


FIGURE 8 Assessment of quantification and contrast accuracy for Rapid Acquisition with Relaxation Enhancement (RARE) without flipback. Box plot of relative quantification and contrast errors for the original uncorrected images and those corrected with each of the three B₁ correction methods. All B₁ correction methods reduced the median error from well above 25% to below 10% (dashed line). Whiskers represent the 5 and 95 percentiles. Asterisks indicate statistically significant differences compared to the uncorrected images

method ($19.5 \pm 9.7\%$) performed marginally better than the *model-based* ($28.9 \pm 19.4\%$) and *hybrid* ($28.4 \pm 14.5\%$) methods. For higher water content the errors were smaller (8–15%). Similarly, the *sensitivity correction* method ($8.3 \pm 5.0\%$) performed slightly better than the other two (*model-based* $15.2 \pm 13.2\%$, *hybrid* $15.2 \pm 8.7\%$). Only the *sensitivity method* significantly improved T₁ contrast (P value = .0002 and .0003 for high and low proton density, respectively).

4 | DISCUSSION

Several methods have been described in the literature to correct B₁ inhomogeneities. These methods are especially crucial for images acquired with transceive surface RF coils. The current study extends this work by demonstrating the feasibility

and efficacy of B₁ field inhomogeneity correction methods for RARE MRI, for which an analytical SI equation is not available. Our phantom results showed a substantial improvement in image homogeneity after B₁ correction using the methods we investigated. We also establish the feasibility of these approaches for samples with more complex structures (ex vivo and in vivo mouse) and in time-constrained scenarios (in vivo). These results demonstrate that images derived from the correction procedures are suitable for accurate T₁ contrast and SI quantification purposes, thus opening the way for parametric T₁ mapping and X-nuclei quantification using surface transceiver RF coils/probes. Compared to previously developed correction methods,^{50–54} the approaches presented and evaluated here are applicable to MR imaging techniques for which no analytical SI equation exists, including but not limited to echo-planar imaging and ultrashort echo time imaging techniques.

RARE with flipback

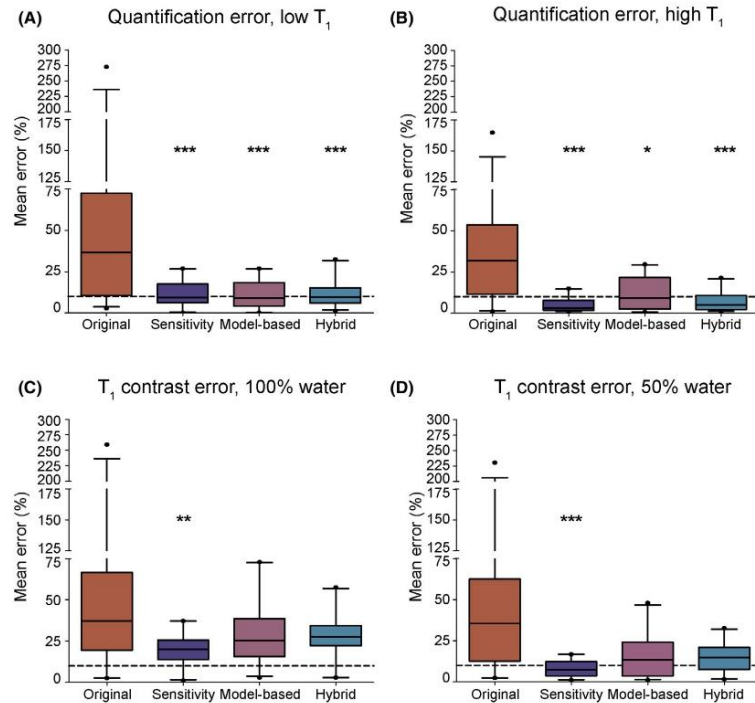


FIGURE 9 Assessment of quantification and contrast accuracy for Rapid Acquisition with Relaxation Enhancement (RARE) with active flipback. Box plot of relative quantification and contrast errors for the original uncorrected images and those corrected with each of the three B_1 correction methods. B_1 correction reduced the median quantification error from well above 25% to below 10% (dashed line) but achieved only a modest improvement in the T_1 contrast error. Whiskers represent the 5 and 95 percentiles. Asterisks indicate statistically significant differences compared to the uncorrected images

The *sensitivity correction* method is well established in the literature²⁷ for correction of sensitivity-related inhomogeneities in a RF coil setup where a volume resonator is used for transmission and a surface RF coil (with or without cryo-cooled technology) for MR signal detection. We demonstrate here that this method is also effective for correction of B_1^+ inhomogeneities. The sensitivity correction method includes an inherently linear B_1^+ correction, because all images are the product of the transmission and reception capabilities of an RF coil. This concept is supported by the quasi-linear trends shown in our SI model for SI vs. T_1 relaxation time, and the linear trends present for the majority of the SI vs. FA range (e.g. between 30°-70° and between 90°-140°).

The two novel B_1 correction methods (*model-based*, *hybrid*) we propose use an empirical SI model of the RF

pulse sequence. The correction workflow involves using the calculated SI model to adjust the SI to that of the nominal FA, based on the actual FA and T_1 . This rectifies the inhomogeneities related to RF transmission (B_1^+), whereas those related to the RF coil sensitivity (B_1^-) are addressed in a separate step using a previously calculated B_1^- map (*model-based*) or using a B_1^+ -corrected uniform phantom (*hybrid*).

Homogeneity was first assessed calculating the PIU and central SI profiles in the corrected and reference images. These tests revealed a high homogeneity, maintained when comparing the ex vivo phantom to the in vivo situation (difference in mean below 5%). A clear difference was found in the profile comparison (RMSE = 0.12 vs 0.26, ex vivo and in vivo respectively), which might be related to a change in animal position when transferring the animal from $^1\text{H-CRP}$ to reference RF coil. These differences might be also caused

by motion (eg, due to misalignment of the FA map, worse B_0 shimming, etc.). Although the option motion averaging was used, it might not have been enough to compensate for bulk motion. Because we were using a RARE-based imaging sequence where the blood signal in large vessels is inherently suppressed due to the use of a spin-echo train, we do not believe the changes in performance to be related to blood flow.⁸⁴

Assessing the accuracy of SI quantification and T_1 contrast measurements yielded different results for RARE with and without flipback that drives the equilibrium regimen. Without the driven equilibrium regimen all correction methods reduced the errors to less than 10% for both quantification and T_1 contrast, and produced statistically significant improvements compared to the original data. For the driven equilibrium regimen, the errors in the original data were more pronounced, which translated into higher SI quantification and T_1 contrast errors after correction. For all three B_1 correction methods, errors were around 10% for quantification, but the accuracy of T_1 contrast was considerably reduced, with errors up to 20-30% (for high water content). Only the *sensitivity method* improved T_1 contrast significantly.

When flipback was inactive, all three methods performed similarly for SI quantification purposes, and yielded improved performance for the low T_1 mode. This can be attributed to the reduced T_1 -weighting at the repetition times used, so that less correction was needed. The *sensitivity correction* method performed slightly better than the other two for SI quantification purposes. The simplicity of this approach makes it preferable for absolute SI quantification. Conversely, our results showed that the *hybrid correction* provides more accuracy when T_1 contrast is essential (eg, for contrast-enhanced imaging in inflammatory disease).

Overall, the *hybrid method* performed better than the *model-based* one. Because the only difference between them is the sensitivity profile calculation, we conclude that the simple *sensitivity correction* performs better than the low FA approximation when computing a B_1^+ map from measurements. The minor artifacts produced at regions distal to the coil are caused by inaccuracies in the FA information associated with low SNR.

The described *model-based approach* is fundamentally limited by SNR constraints at larger distances from the RF coil, and by the accuracy of the B_1 and T_1 maps and the polynomial fit. Determining the distance until which a meaningful correction can be achieved is challenging, since it depends on the conditions and scanning parameters used (eg, coil dimensions, SNR, acquisition time). Hence, this distance should be determined by each user, for each specific setup: (1) calculate the central profile plots for each correction and (2) determine at what distance from the coil the corrected profile still follows that of the reference volume RF coil. This will not require extra time, because T_1 mapping with the reference RF coil is anyway required for the B_1 correction.

Accurate knowledge of T_1 and FA is crucial for the precise correction of the B_1 inhomogeneities using the *model-based* and *hybrid methods*. For our workflow, we selected readily-available MR imaging protocols (eg, double angle mapping, RARE with variable TR). Limitations are related to the inherent instability associated with the FA and T_1 mapping techniques, the lack of an established gold standard, and substantial variability among the different methods. FA mapping depends on the slice excitation profile, B_0 homogeneity and other factors,⁶¹ which produce additional uncertainties. Moreover, FA mapping techniques are usually imprecise for low FAs,⁸⁵ increasing the FA error at large distances from the RF coil.

T_1 mapping is equally challenging and subject to many sources of error. Fundamentally dependent on the FA, it is usually performed using volume resonators or a combination of RF coils for transmit-receive (volume for transmit, surface for receive) to attenuate the effects of B_1^+ inhomogeneity. A caveat of these methods (*model-based* and *hybrid*) is the need to acquire a T_1 map with each image (in order to consider the T_1 contrast of tissues) when removing the field inhomogeneities in ^1H images. Although T_1 mapping is feasible using a cryocooled RF probe,⁸⁶ we invested the extra time and used a volume resonator to reduce T_1 map errors.

An alternative to calculate the signal evolution (SI model) would be to use extended phase graph⁸⁷ or Bloch⁸⁸ simulations. Equally, magnetic resonance fingerprinting⁸⁹ could be used not only to create the model but also to acquire a T_1 and B_1 map altogether by changing FA and TR, reducing the amount of scan time needed and producing a tailored correction ("real" B_1 map of the phantom/mouse). To our knowledge there are no magnetic resonance fingerprinting-RARE techniques available to date and the development of such MR sequences was out of the scope of this study.

When considering SNR, it is important to bear in mind that these correction methods entail multiplication by a position-dependent matrix of correction factors. Thus, both the signal and the noise will be increased; furthermore, this effect will be different for each image pixel. Therefore, SNR calculations must be performed on the original uncorrected images.

The B_1 correction methods presented here have widespread implications. We demonstrated that these methods are not only useful for the specific case of cryogenically cooled RF probes, frequently used to boost SNR in preclinical MRI,^{24,40,90} but are also generally applicable for transceive surface RF coils like single-loop RF coils. We demonstrated the applicability of the correction methods in conventional ^1H brain imaging; however, these methods can also be applied to moving organs, for example, cardiovascular research, as long as the calculated reference power is correct and the maps and images are acquired using a trigger and spatially aligned. These approaches are also highly relevant for quantitative MR of X-nuclei, where absolute SI is important._{ENREF_39,40} For the low-SNR scenarios that are

prevalent in X-nuclei imaging, the procedures that are used to validate the correction methods described in this manuscript (eg, PIU, central profile plots) might not be entirely valid. In these cases, we suggest performing error propagation simulations associated with inaccuracies due to the low SNR or to simply use the sensitivity correction method.

Interestingly, all correction methods we studied here greatly improved SI quantification and image contrast, with only minor differences in performance of the three approaches. The best results were obtained with the *hybrid correction*, but contrary to expectations, even the straightforward *sensitivity correction* performed well. Therefore, one could recommend this last method due to its simplicity. These B_1 correction methods permit quantitative SI and T_1 contrast measurements with transceiver surface RF coils, using MRI techniques for which analytical SI equations do not exist. This circumvents a key limitation and offers a new approach for correcting B_1 inhomogeneity that may be applied for a broad range of biomedical research applications.

ACKNOWLEDGMENTS

This work was funded in part (Thoralf Niendorf, Sonia Waiczies, Andreas Pohlmann) by the German Research Foundation (Gefördert durch die Deutsche Forschungsgemeinschaft [DFG], Projektnummer 394046635, SFB 1365, *RENOPROTECTION*) and to S.W. (DFG-WA2804) and A.P. (DFG-PO1869). The authors wish to thank David Alsop (Harvard Medical School and Beth Israel Deaconess Medical Center, Boston, MA, USA), David Norris (Radboud University, Nijmegen, The Netherlands and Erwin L. Hahn Institute for Magnetic Resonance Imaging, Essen, Germany), and Jürgen Hennig (University Medical Center Freiburg, Germany) for helpful discussion, and Victoria Prochnov (Max-Delbrück Center for Molecular Medicine in the Helmholtz Association, Berlin, Germany) for her assistance with the in vivo experiments.

CONFLICT OF INTEREST

Andre Kuehne is an employee of MRI.TOOLS GmbH, Berlin, Germany. Thoralf Niendorf is founder and chief executive officer of MRI.TOOLS GmbH, Berlin, Germany. All other authors declare no conflict of interest.

DATA AVAILABILITY STATEMENT

The code and data that support the findings of this study are openly available in GitHub at <https://github.com/pramosdelgado/B1correction-toolkit>.

ORCID

Paula Ramos Delgado  <https://orcid.org/0000-0003-2009-3024>
 João S. Periquito  <https://orcid.org/0000-0003-3702-9264>
 Sonia Waiczies  <https://orcid.org/0000-0002-9916-9572>

REFERENCES

- Constable R, Henkelman R. Contrast, resolution, and detectability in MR imaging. *J Comput Assist Tomogr*. 1991;15:297-303.
- Fuderer M. The information content of MR images. *IEEE Trans Med Imaging*. 1988;7:368-380.
- Redpath T. Signal-to-noise ratio in MRI. *Br J Radiol*. 1998;71:704-707.
- Portnoy S, Kale S, Feintuch A, Tardif C, Pike G, Henkelman R. Information content of SNR/resolution trade-offs in three-dimensional magnetic resonance imaging. *Med Phys*. 2009;36:1442-1451.
- Kale S, Chen X, Henkelman R. Trading off SNR and resolution in MR images. *NMR Biomed*. 2009;22:488-494.
- Griswold MA, Jakob PM, Heidemann RM, et al. Generalized auto-calibrating partially parallel acquisitions (GRAPPA). *Magn Reson Med*. 2002;47:1202-1210.
- Pruessmann K, Weiger M, Scheidegger M, Boesiger P. SENSE: Sensitivity encoding for fast MRI. *Magn Reson Med*. 1999;42:952-962.
- Lustig M, Donoho D, Pauly J. Sparse MRI: The application of compressed sensing for rapid MR imaging. *Magn Reson Med*. 2007;58:1182-1195.
- Niendorf T, Barth M, Kober F, Trattnig S. From ultrahigh to extreme field magnetic resonance: Where physics, biology and medicine meet. *Magn Reson Mater Phys, Biol Med*. 2016;29:309-311.
- Ladd M. The quest for higher sensitivity in MRI through higher magnetic fields. *Zeitschrift für medizinische Physik*. 2018;28:1-3.
- Moser E, Laistler E, Schmitt F, Kontaxis G. Ultra-high field NMR and MRI—The role of magnet technology to increase sensitivity and specificity. *Front Phys*. 2017;5:33. <https://doi.org/10.3389/fphy.2017.0003333>.
- Axel L, Hayes C. Surface coil magnetic resonance imaging. *Archives Internationales de Physiologie et de Biochimie*. 1985;93:11-18.
- Crowley M, Evelhoch J, Ackermann J. The surface-coil NMR receiver in the presence of homogeneous B_1 excitation. *J Magn Reson*. 1985;64:20-31.
- Hosseinzhadian S, Frass-Kriegel R, Goluch-Roat S, et al. A flexible 12-channel transceiver array of transmission line resonators for 7 T MRI. *J Magn Reson*. 2018;296:47-59.
- Pinkerton R, Barberi E, Menon R. Transceive surface coil array for magnetic resonance imaging of the human brain at 4 T. *Magn Reson Med*. 2005;54:499-503.
- Pinkerton R, Near J, Barberi E, Menon R, Bartha R. Transceive surface coil array for MRI of the human prostate at 4T. *Magn Reson Med*. 2007;57:455-458.
- Graessl A, Renz W, Hezel F, et al. Modular 32-channel transceiver coil array for cardiac MRI at 7.0T. *Magn Reson Med*. 2014;72:276-290.
- Rietsch SHG, Pfaffenrot V, Bitz AK, et al. An 8-channel transceiver 7-channel receive RF coil setup for high SNR ultrahigh-field MRI of the shoulder at 7T. *Med Phys*. 2017;44:6195-6208.
- He X, Ertürk MA, Grant A, et al. First in-vivo human imaging at 10.5T: Imaging the body at 447 MHz. *Magn Reson Med*. 2020;84:289-303. <https://doi.org/10.1002/mrm.28131>.
- Ertürk M, Raaijmakers A, Adriany G, Ugurbil K, Metzger G. A 16-channel combined loop-dipole transceiver array for 7 Tesla body MRI. *Magn Reson Med*. 2017;77:884-894.

21. Weinberger O, Winter L, Dieringer MA, et al. Local multi-channel RF surface coil versus body RF coil transmission for cardiac magnetic resonance at 3 Tesla: Which configuration is winning the game? *PLoS ONE*. 2016;11:e0161863.
22. Niendorf T, Paul K, Oezerdem C, et al. W(h)ither human cardiac and body magnetic resonance at ultrahigh fields? Technical advances, practical considerations, applications, and clinical opportunities. *NMR Biomed*. 2016;29:1173-1197.
23. Kovacs H, Moskau D, Spraul M. Cryogenically cooled probes—A leap in NMR technology. *Prog Nucl Magn Reson Spectrosc*. 2005;46:131-155.
24. Baltes C, Radzwill N, Bosshard S, Marek D, Rudin M. Micro MRI of the mouse brain using a novel 400MHz cryogenic quadrature RF probe. *NMR Biomed*. 2009;22:834-842.
25. Niendorf T, Pohlmann A, Reimann HM, et al. Advancing cardiovascular, neurovascular, and renal magnetic resonance imaging in small rodents using cryogenic radiofrequency coil technology. *Front Pharmacol*. 2015;12:255.
26. Carvalho V, Hertanu A, Grélard A, et al. MRI assessment of multiple dipolar relaxation time (T_{1D}) components in biological tissues interpreted with a generalized inhomogeneous magnetization transfer (ihMT) model. *J Magn Reson*. 2020;311:106668.
27. Axel L, Constantini J, Listerud J. Intensity correction in surface-coil MR imaging. *Am J Roentgenol*. 1987;148:418-420.
28. Wicks D, Barker G, Tofts P. Correction of intensity nonuniformity in MR images of any orientation. *Magn Reson Imaging*. 1993;11:183-196.
29. McVeigh E, Bronskill M, Henkelman R. Phase and sensitivity of receiver coils in magnetic resonance imaging. *Med Phys*. 1986;13:806-814.
30. Tincher M, Meyer C, Gupta R, Williams D. Polynomial modeling and reduction of RF body coil spatial inhomogeneity in MRI. *IEEE Trans Med Imaging*. 1993;12:361-365.
31. Meyer CR, Bland PH, Pipe J. Retrospective correction of intensity inhomogeneities in MRI. *IEEE Trans Med Imaging*. 1995;14:36-41.
32. Haselgrove J, Prammer M. An algorithm for compensation of surface-coil images for sensitivity of the surface coil. *Magn Reson Imaging*. 1986;4:469-472.
33. Moyher S, Vigneron D, Nelson S. Surface coil MR imaging of the human brain with an analytic reception profile correction. *J Magn Reson Imaging*. 1995;5:139-144.
34. Narayana P, Brey W, Kulkarny M, Sievenpiper C. Compensation for surface coil sensitivity variation in magnetic resonance imaging. *Magn Reson Imaging*. 1988;6:271-274.
35. Vaidya M, Collins C, Sodickson D, Brown R, Wiggins G, Lattanzi R. Dependence of B_1^+ and B_1^- field patterns of surface coils on the electrical properties of the sample and the MR operating frequency. *Concept Magn Reson B*. 2016;46B:25-40.
36. Keltner J, Carlson J, Roos M, Wong S, Wong T, Budinger T. Electromagnetic fields of surface coil *in vivo* NMR at high frequencies. *Magn Reson Med*. 1991;22:467-480.
37. Boulant N. T_1 and T_2 effects during radio-frequency pulses in spoiled gradient echo sequences. *J Magn Reson*. 2009;197:213-218.
38. Dieringer MA, Deimling M, Santoro D, et al. Rapid parametric mapping of the longitudinal relaxation time T_1 using two-dimensional variable flip angle magnetic resonance imaging at 1.5 Tesla, 3 Tesla, and 7 Tesla. *PLoS ONE*. 2014;9:e91318.
39. Lommen J, Konstantin S, Krämer P, Schad L. Enhancing the quantification of tissue sodium content by MRI: Time-efficient sodium B_1 mapping at clinical field strengths. *NMR Biomed*. 2015;29:129-136.
40. Waiczies S, Millward JM, Starke L, et al. Enhanced fluorine-19 MRI sensitivity using a cryogenic radiofrequency probe: Technical developments and *ex vivo* demonstration in a mouse model of neuroinflammation. *Sci Rep*. 2017;7:9808.
41. de Graaf R, Nicolay K. Adiabatic rf pulses: Applications to *in vivo* NMR. *Magn Reson Med*. 1998;40:690-696.
42. Baldanchani P, Pauly J, Spielman D. Designing adiabatic radio frequency pulses using the Shinnar-Le Roux algorithm. *Magn Reson Med*. 2010;64:843-851.
43. Zivkovic I, Teeuwisse W, Slobozhanyuk A, Nenasheva E, Webb A. High permittivity ceramics improve the transmit field and receive efficiency of a commercial extremity coil at 1.5 Tesla. *J Magn Reson*. 2019;299:59-65.
44. Brink W, van der Jagt A, Versluis M, Verbiest B, Webb A. High permittivity dielectric pads improve high spatial resolution magnetic resonance imaging of the inner ear at 7 T. *Invest Radiol*. 2014;49:271-277.
45. O'Brien K, Magill A, Delacoste J, et al. Dielectric pads and low- B_1^+ adiabatic pulses: Complementary techniques to optimize structural T_1 w whole-brain MP2RAGE scans at 7 Tesla. *J Magn Reson Imaging*. 2014;40:804-812.
46. O'Reilly T, Webb A, Brink W. Practical improvements in the design of high permittivity pads for dielectric shimming in neuroimaging at 7 T. *J Magn Reson*. 2016;270:108-114.
47. van der Bergen B, van der Berg C, Bartels L, Lagendijk J. 7 T body MRI: B_1 shimming with simultaneous SAR reduction. *Phys Med Biol*. 2007;52:5429-5441.
48. Winkler S, Rutt B. Practical methods for improving B_1^+ homogeneity in 3 Tesla breast imaging. *J Magn Reson Imaging*. 2015;41:992-999.
49. Yang QX, Mao W, Wang J, et al. Manipulation of image intensity distribution at 7.0 T: Passive RF shimming and focusing with dielectric materials. *J Magn Reson Imaging*. 2006;24:197-202.
50. Vernikouskaya I, Pochert A, Lindén M, Rasche V. Quantitative ^{19}F MRI of perfluoro-15-crown-5-ether using uniformity correction of the spin excitation and signal reception. *Magn Reson Mater Phys, Biol Med*. 2019;32:25-36.
51. van Schie J, Lavini C, van Vliet L, Vos F. Feasibility of a fast method for B_1 -inhomogeneity correction for FSPGR sequences. *Magn Reson Imaging*. 2015;33:312-318.
52. Wang J, Qiu M, Constable R. *In vivo* method for correcting transmit/receive nonuniformities with phased array coils. *Magn Reson Med*. 2005;53:666-674.
53. Collewet G, Davenel A, Toussaint C, Akoka S. Correction of intensity nonuniformity in spin-echo T_1 -weighted images. *Magn Reson Imaging*. 2002;20:365-373.
54. Cooper M, Nguyen T, Spincemaille P, Prince M, Weinsaft J, Wang Y. Flip angle profile correction for T_1 and T_2 quantification with look-locker inversion recovery 2D SSFP imaging. *Magn Reson Med*. 2012;68:1579-1585.
55. Ma D, Coppo S, Chen Y, et al. Slice profile and B_1 corrections in 2D magnetic resonance fingerprinting. *Magn Reson Med*. 2017;78:1781-1789.
56. Deoni S. Correction of main and transmit magnetic field (B_0 and B_1) inhomogeneity effects in multicomponent-driven equilibrium single-pulse observation of T_1 and T_2 . *Magn Reson Med*. 2011;65:1021-1035.

57. Insko E, Bolinger L. Mapping of the radiofrequency field. *J Magn Reson*. 1993;103A:82-85.
58. Akoka S, Franconi F, Seguin F, Le Pape A. Radiofrequency map of an NMR coil by imaging. *Magn Reson Imaging*. 1993;11:437-441.
59. Morrell G. A phase-sensitive method of flip angle mapping. *Magn Reson Med*. 2008;60:889-894.
60. Yarnykh V. Actual flip-angle imaging in the pulsed steady state: A method for rapid three-dimensional mapping of the transmitted radiofrequency field. *Magn Reson Med*. 2007;57:192-200.
61. Wang J, Mao W, Qiu M, Smith M, Constable R. Factors influencing flip angle mapping in MRI: RF pulse shape, slice-select gradients, off-resonance excitation, and B_0 inhomogeneities. *Magn Reson Med*. 2006;56:463-468.
62. Stollberger R, Wach P. Imaging of the active B1 field in vivo. *Magn Reson Med*. 1996;35:246-251.
63. Cunningham C, Pauly J, Nayak K. Saturated double-angle method for rapid B_1^+ mapping. *Magn Reson Med*. 2006;55:1326-1333.
64. Wang D, Heberlein K, LaConte S, Hu X. Inherent insensitivity to RF inhomogeneity in FLASH imaging. *Magn Reson Med*. 2004;52:927-931.
65. Bernstein M. Gradient echo. In: Bernstein M, King K, Zhou X, eds. *Handbook of MRI Pulse Sequences*. Burlington, MA, San Diego, CA and London: Elsevier Academic Press; 2004:579-605.
66. Hennig J, Nauwerth A, Friedburg H. RARE imaging: A fast imaging method for clinical MR. *Magn Reson Med*. 1986;3:823-833.
67. Conturo T, Beth A, Arenstorff R, Price R. Simplified mathematical description of longitudinal recovery in multiple-echo sequences. *Magn Reson Med*. 1987;4:282-288.
68. Meara S, Barker G. Evolution of the longitudinal magnetization for pulse sequences using a fast spin-echo readout: Application to fluid-attenuated inversion-recovery and double inversion-recovery sequences. *Magn Reson Med*. 2005;54:241-245.
69. Breuer F, Blaimer M, Heidemann R, Mueller M, Griswold M, Jakob P. Controlled aliasing in parallel imaging results in higher acceleration (CAIPIRINHA) for multi-slice imaging. *Magn Reson Med*. 2005;53:684-691.
70. Skare S, Holdsworth S, Lilja A, Bammer R. Image domain propelled fast spin echo. *Magn Reson Imaging*. 2013;31:385-395.
71. Zhou X, Liang Z, Gewalt S, Cofer G, Lauterbur P, Johnson G. A fast spin echo technique with circular sampling. *Magn Reson Med*. 1998;39:23-27.
72. Altbach MI, Outwater EK, Trouard TP, et al. Radial fast spin-echo method for T_2 -weighted imaging and T_2 mapping of the liver. *J Magn Reson Imaging*. 2002;16:179-189.
73. Busse RF, Brau ACS, Vu A, et al. Effects of refocusing flip angle modulation and view ordering in 3D fast spin echo. *Magn Reson Med*. 2008;60:640-649.
74. Reeder SB, Pineda AR, Wen Z, et al. Iterative decomposition of water and fat with echo asymmetry and least-squares estimation (IDEAL): Application with fast spin-echo imaging. *Magn Reson Med*. 2005;54:636-644.
75. Oshio K, Feinberg D. GRASE (Gradient- and Spin Echo) imaging: A novel fast MRI technique. *Magn Reson Med*. 1991;20:344-349.
76. Robson D, Gatehouse P, Bydder M, Bydder G. Magnetic resonance: An introduction to ultrashort TE (UTE) imaging. *J Comput Assist Tomogr*. 2003;27:825-846.
77. Mansfield P. Multi-planar image formation using NMR spin echoes. *J Phys C: Solid State Phys*. 1977;10:55-58.
78. Waiczies H, Lepore S, Drechsler S, et al. Visualizing brain inflammation with a shingled-leg radio-frequency head probe for $^{19}\text{F}/^1\text{H}$ MRI. *Sci Rep*. 2013;3:1280.
79. *Polyfitn* [computer program]. Version 1.3. File Exchange. Natick, MA: The MathWorks, Inc. 2016.
80. Ibrahim T, Hue Y, Tang L. Understanding and manipulating the RF fields at high field MRI. *NMR Biomed*. 2009;22:927-936.
81. Pauly J, Nishimura D, Macovski A. A k-space analysis of small-tip-angle excitation. *J Magn Reson*. 1989;81:43-56.
82. Manjón J, Coupé P, Martí-Bonmati L, Collins D, Robles M. Adaptive non-local means denoising of MR images with spatially varying noise levels. *J Magn Reson Imaging*. 2010;31:192-203.
83. Price R, Axel L, Morgan T, et al. Quality assurance methods and phantoms for magnetic resonance imaging: Report of AAPM nuclear magnetic resonance task group No. 1. *Med Phys*. 1990;17:287-295.
84. Feinberg DA, Mills CM, Posin JP, et al. Multiple spin-echo magnetic resonance imaging. *Radiology*. 1985;155:437-442.
85. Balezeau F, Eliat P, Cayamo A, Saint-Jalmes H. Mapping of low flip angles in magnetic resonance. *Phys Med Biol*. 2011;56:6635-6647.
86. Khalil AA, Mueller S, Foddiss M, et al. Longitudinal ^{19}F magnetic resonance imaging of brain oxygenation in a mouse model of vascular cognitive impairment using a cryogenic radiofrequency coil. *Magn Reson Mater Phys, Biol Med*. 2019;32:105-114.
87. Weigel M. Extended phase graphs: Dephasing, RF pulses, and echoes—Pure and simple. *J Magn Reson Imaging*. 2015;41:266-295.
88. Bloch F. Nuclear induction. *Phys Rev*. 1946;70:460-474.
89. Ma D, Gulani V, Seiberlich N, et al. Magnetic resonance fingerprinting. *Nature*. 2013;495:187-192.
90. Ratering D, Baltes C, Nordmeyer-Massner J, Marek D, Rudin M. Performance of a 200-MHz cryogenic RF probe designed for MRI and MRS of the murine brain. *Magn Reson Med*. 2008;59:1440-1447.

How to cite this article: Delgado PR, Kuehne A, Periquito JS, et al. B_1 inhomogeneity correction of RARE MRI with transceive surface radiofrequency probes. *Magn Reson Med*. 2020;84:2684–2701. <https://doi.org/10.1002/mrm.28307>

Journal Data Filtered By: **Selected JCR Year: 2020** Selected Editions: SCIE,SSCI
 Selected Categories: **"RADIOLOGY, NUCLEAR MEDICINE and MEDICAL IMAGING"** Selected Category Scheme: WoS
Gesamtanzahl: 134 Journale

Rank	Full Journal Title	Total Cites	Journal Impact Factor	Eigenfactor Score
1	JACC-Cardiovascular Imaging	14,398	14.805	0.032190
2	RADIOLOGY	72,249	11.105	0.053000
3	JOURNAL OF NUCLEAR MEDICINE	32,949	10.057	0.032490
4	IEEE TRANSACTIONS ON MEDICAL IMAGING	27,030	10.048	0.033600
5	EUROPEAN JOURNAL OF NUCLEAR MEDICINE AND MOLECULAR IMAGING	20,634	9.236	0.024430
6	MEDICAL IMAGE ANALYSIS	11,568	8.545	0.018360
7	Photoacoustics	1,093	8.484	0.001780
8	CLINICAL NUCLEAR MEDICINE	6,344	7.794	0.006990
9	Circulation-Cardiovascular Imaging	7,640	7.792	0.015510
10	ULTRASOUND IN OBSTETRICS & GYNECOLOGY	18,164	7.299	0.018820
11	INTERNATIONAL JOURNAL OF RADIATION ONCOLOGY BIOLOGY PHYSICS	50,525	7.038	0.039410
12	European Heart Journal-Cardiovascular Imaging	8,423	6.875	0.020790
13	NEUROIMAGE	119,618	6.556	0.105820
14	ULTRASCHALL IN DER MEDIZIN	2,911	6.548	0.003340
15	RADIOTHERAPY AND ONCOLOGY	22,462	6.280	0.024940
16	INVESTIGATIVE RADIOLOGY	7,700	6.016	0.007870
17	JOURNAL OF NUCLEAR CARDIOLOGY	5,882	5.952	0.005390
18	SEMINARS IN RADIATION ONCOLOGY	2,837	5.934	0.002710
19	Journal of the American College of Radiology	6,584	5.532	0.013810
20	JOURNAL OF CARDIOVASCULAR MAGNETIC RESONANCE	6,935	5.364	0.010460

Selected JCR Year: 2020; Selected Categories: "RADIOLOGY, NUCLEAR MEDICINE and MEDICAL IMAGING"












1

Rank	Full Journal Title	Total Cites	Journal Impact Factor	Eigenfactor Score
21	RADIOGRAPHICS	16,021	5.333	0.012160
22	EUROPEAN RADIOLOGY	29,642	5.315	0.035390
23	Insights into Imaging	3,147	5.231	0.005200
24	HUMAN BRAIN MAPPING	27,538	5.038	0.035480
25	Zeitschrift für Medizinische Physik	781	4.820	0.001270
26	JOURNAL OF MAGNETIC RESONANCE IMAGING	21,238	4.813	0.023350
27	COMPUTERIZED MEDICAL IMAGING AND GRAPHICS	3,232	4.790	0.003470
28	MAGNETIC RESONANCE IN MEDICINE	38,556	4.668	0.027450
29	Molecular Imaging	1,323	4.488	0.001050
30	SEMINARS IN NUCLEAR MEDICINE	2,729	4.446	0.002640
31	Journal of Cardiovascular Computed Tomography	2,352	4.309	0.004610
32	MEDICAL PHYSICS	30,918	4.071	0.025740
33	JOURNAL OF DIGITAL IMAGING	3,680	4.056	0.004420
34	NMR IN BIOMEDICINE	8,939	4.044	0.009700
35	Diagnostic and Interventional Imaging	2,437	4.026	0.003290
36	AMERICAN JOURNAL OF ROENTGENOLOGY	39,721	3.959	0.024610
37	INTERNATIONAL JOURNAL OF HYPERTHERMIA	6,199	3.914	0.006060
38	CANCER IMAGING	2,143	3.909	0.002280
39	Quantitative Imaging in Medicine and Surgery	2,318	3.837	0.003810
40	AMERICAN JOURNAL OF NEURORADIOLOGY	27,423	3.825	0.024030
41	Biomedical Optics Express	12,803	3.732	0.021630
42	Ultrasonography	887	3.675	0.001650

2

Selected JCR Year: 2020; Selected Categories: "RADIOLOGY, NUCLEAR MEDICINE and MEDICAL IMAGING"

B₁ inhomogeneity correction of RARE MRI at low SNR: Quantitative in vivo ¹⁹F MRI of mouse neuroinflammation with a cryogenically-cooled transceive surface radiofrequency probe

Paula Ramos Delgado^{1,2}   | Andre Kuehne³  | Mariya Aravina¹  |
Jason M. Millward¹  | Alonso Vázquez³  | Ludger Starke¹  |
Helmar Waiczies³  | Andreas Pohlmann¹  | Thoralf Niendorf^{1,2,3}  |
Sonia Waiczies¹ 

¹Max-Delbrück-Center for Molecular Medicine in the Helmholtz Association (MDC), Berlin Ultrahigh Field Facility, Berlin, Germany

²Experimental and Clinical Research Center, a cooperation between the Max-Delbrück-Center for Molecular Medicine in the Helmholtz Association and the Charité–Universitätsmedizin Berlin, Berlin, Germany

³MRI.TOOLS, Berlin, Germany

Correspondence

Paula Ramos Delgado, Berlin Ultrahigh Field Facility, Max Delbrück Center for Molecular Medicine in the Helmholtz Association, Robert-Rössle-Str. 10, 13125 Berlin, Germany.
Email: Paula.Ramos@mdc-berlin.de

Funding information

The German Research Foundation (Deutsche Forschungsgemeinschaft [DFG]); Grant/Award Nos. DFG-PO1869, DFG-WA2804, and Projektnummer 394046635, SFB 1365, RENOPROTECTION

Purpose: Low SNR in fluorine-19 (¹⁹F) MRI benefits from cryogenically-cooled transceive surface RF probes (CRPs), but strong B₁ inhomogeneities hinder quantification. Rapid acquisition with refocused echoes (RARE) is an SNR-efficient method for MRI of neuroinflammation with perfluorinated compounds but lacks an analytical signal intensity equation to retrospectively correct B₁ inhomogeneity. Here, a workflow was proposed and validated to correct and quantify ¹⁹F-MR signals from the inflamed mouse brain using a ¹⁹F-CRP.

Methods: In vivo ¹⁹F-MR images were acquired in a neuroinflammation mouse model with a quadrature ¹⁹F-CRP using an imaging setup including 3D-printed components to acquire co-localized anatomical and ¹⁹F images. *Model-based corrections* were validated on a uniform ¹⁹F phantom and in the neuroinflammatory model. Corrected ¹⁹F-MR images were benchmarked against reference images and overlaid on in vivo ¹H-MR images. Computed concentration uncertainty maps using Monte Carlo simulations served as a measure of performance of the B₁ corrections.

Results: Our study reports on the first quantitative in vivo ¹⁹F-MR images of an inflamed mouse brain using a ¹⁹F-CRP, including in vivo T₁ calculations for ¹⁹F-nanoparticles during pathology and B₁ corrections for ¹⁹F-signal quantification. *Model-based corrections* markedly improved ¹⁹F-signal quantification from errors > 50% to < 10% in a uniform phantom (*p* < 0.001). Concentration uncertainty maps ex vivo and in vivo yielded uncertainties that were generally < 25%.

This is an open access article under the terms of the Creative Commons Attribution-NonCommercial License, which permits use, distribution and reproduction in any medium, provided the original work is properly cited and is not used for commercial purposes.

© 2021 The Authors. *Magnetic Resonance in Medicine* published by Wiley Periodicals LLC on behalf of International Society for Magnetic Resonance in Medicine.

Monte Carlo simulations prescribed SNR ≥ 10.1 to reduce uncertainties $< 10\%$, and SNR ≥ 4.25 to achieve uncertainties $< 25\%$.

Conclusion: Our *model-based correction* method facilitated ^{19}F signal quantification in the inflamed mouse brain when using the SNR-boosting ^{19}F -CRP technology, paving the way for future low-SNR ^{19}F -MRI applications in vivo.

KEYWORDS

^{19}F -MRI, B_1 correction, inflammation, RARE, transceive surface RF probe

1 | INTRODUCTION

Fluorine-19 (^{19}F) MRI shows promise in several biomedical applications.^{1–3} However, ^{19}F -MRI suffers from low SNR due to the very limited availability of ^{19}F nuclei in vivo. Consequently, ^{19}F -MRI is constrained by long measurements. One SNR-boosting strategy has been to implement sensitivity-promoting surface RF coil technologies.⁴ Cryogenically cooled transceive surface RF probes (CRPs) have introduced a paradigm shift in preclinical imaging, providing substantial SNR gains compared with room-temperature RF coils.^{5–10} Further increases in SNR have been achieved with quadrature configurations, which provide a $\sqrt{2}$ SNR gain and better transversal B_1 homogeneity compared with linear polarized RF coils.^{11–13}

Quadrature CRPs are typically single-tuned for X-nuclei,⁸ since dual-tunable capabilities would require electromagnetic decoupling between coil elements,^{14–16} degrading signal sensitivity. This adds extra post-processing challenges when locating quantified ^{19}F signals in vivo. Moreover, the low-SNR and sparse nature of ^{19}F prevents the MR system from performing reference power adjustments without an external ^{19}F reference.

The greatest challenge of transceive surface RF probes like the ^{19}F -CRP is their strong B_1 inhomogeneities,^{4,17} which hamper T_1 contrast and signal quantification, as the measured ^{19}F signal depends on the number of ^{19}F atoms per pixel, their distance from the probe surface, and relaxation times. Inhomogeneities in the excitation field (B_1^+) are typically corrected retrospectively using signal-intensity (SI) equations of corresponding RF pulse sequences. This is possible for gradient-echo or spin-echo techniques,^{18–20} but the SNR-efficient rapid acquisition with refocused echoes (RARE) technique lacks an exact SI equation.^{21,22} We previously implemented three B_1 correction methods (*model-based*, *hybrid*, and *sensitivity*) for RARE ^1H -MRI and transceive surface RF probes, considerably increasing image homogeneity and significantly reducing errors in signal quantification and T_1 contrast.²³

The low SNR, signal sparsity, and lack of a priori location of the ^{19}F signal constrain the reliability of signal

quantification, even after B_1 correction. A procedure that evaluates the quality of the SI correction and quantification per image voxel is thus crucial. This is particularly relevant when monitoring and quantifying inflammation e.g., in the animal model of multiple sclerosis (MS), experimental autoimmune encephalomyelitis (EAE)^{24,25} using ^{19}F -nanoparticles (NPs).

Here, we implemented and validated our B_1 correction approaches²³ to correct ^{19}F -MR images from a single-tuned quadrature ^{19}F -CRP after estimating in vivo T_1 of ^{19}F -NPs in the EAE brain using a volume resonator. We performed Monte Carlo SNR simulations to estimate the associated concentration uncertainty. We also established a workflow using 3D-printed add-ons to facilitate in vivo localization of ^{19}F -MR images from the ^{19}F -CRP on anatomical images acquired from a ^1H volume resonator. This workflow and correction method delivered the first quantitative in vivo ^{19}F -MR images of an inflamed EAE mouse brain using a ^{19}F -CRP. These results will be pivotal to drive future ^{19}F research using transceive surface RF technologies to quantify inflammation or ^{19}F -compounds in in vivo studies.

2 | METHODS

2.1 | Magnetic resonance hardware

All experiments were carried out on a 9.4T small animal MR scanner (BioSpec 94/20; Bruker BioSpin, Ettlingen, Germany).

^{19}F images were acquired using a ^{19}F cryogenically-cooled transceive surface RF probe (^{19}F -CRP CryoProbe; Bruker BioSpin)¹⁷ for mouse head imaging (inner diameter [ID] = 20 mm), composed of two elements operating in quadrature mode. Anatomical images were measured using a 72-mm (ID) linear volume resonator (Bruker BioSpin). T_1 measurements of ^{19}F -NPs in EAE brains and reference ^{19}F images were acquired using a small-diameter (ID = 18.4 mm) mouse head $^1\text{H}/^{19}\text{F}$ volume resonator.²⁶

2.2 | Anatomical and ^{19}F -MRI setup

Given the lacking ^1H channel, an imaging setup including 3D-printed components was devised to acquire colocalized anatomical and ^{19}F -CRP images.

2.2.1 | Animal bed modification

The standard animal bed uses a lever that elevates the bed, lifting the mouse head closer to the ^{19}F -CRP. This feature hampers position reproducibility. To ensure spatial alignment of both ^{19}F -CRP and anatomical images, a 3D-printed

blocking component (Y-axis blocker) was designed to eliminate movement in the Y-axis (Figure 1A). Additionally, a new head holder was designed and 3D-printed to place the mouse head closer to the CRP surface (Figure 1A).

2.2.2 | ^1H -MRI setup

The 72-mm-volume resonator was positioned around the center tube holding the ^{19}F -CRP. Anatomical images were acquired after a CRP replica (dummy), inserted from the back of the scanner, was kept in place while the animal bed was inserted from the front.

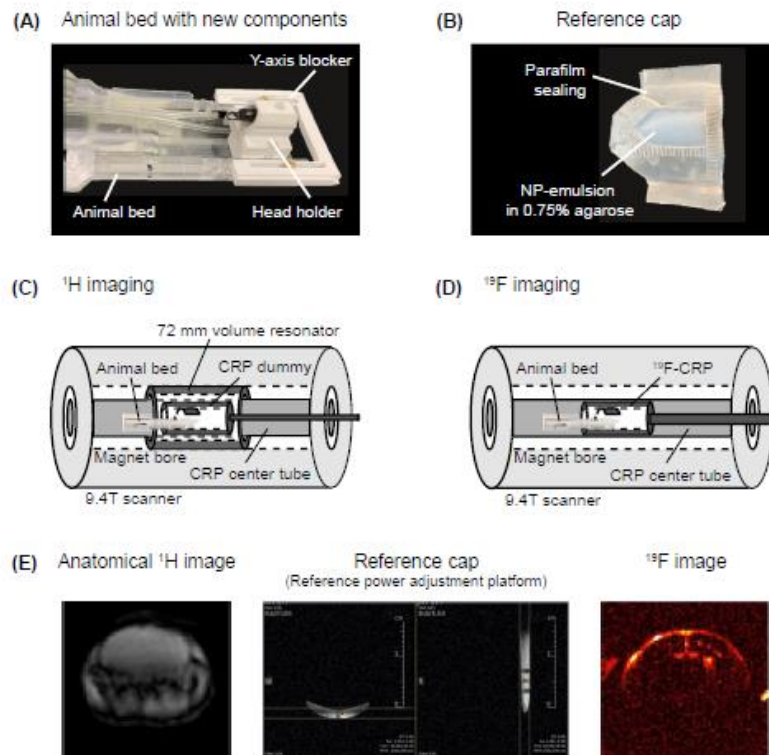


FIGURE 1 Anatomical and fluorine-19 (^{19}F) imaging setup designed for a single-tuned cooled transceive surface RF probe (CRP). (A) Close-up view of the animal bed provided by the vendor with a custom-designed component that eliminates mobility in the y-axis (y-axis blocker) and a new head holder to bring the animal's head closer to the surface of the CRP. (B) Reference cap containing ^{19}F -loaded nanoparticles (NPs) to perform ^{19}F -CRP reference power adjustments and as reference for quantification. (C,D) $^1\text{H}/^{19}\text{F}$ imaging setups. (E) For exemplary in vivo images, anatomical images and slice planning are performed using a 72-mm volume resonator and a CRP dummy. Afterward, reference power calibrations are carried out using the reference cap, and ^{19}F images are acquired using the ^{19}F -CRP

2.2.3 | ^{19}F -MRI setup

Both animal bed and dummy were removed and the ^1H -volume resonator was retracted toward the back of the scanner. The ^{19}F -CRP was mounted as instructed by the vendor.

A ^{19}F -NP reference cap (section 2.3) was placed over the mouse head to perform ^{19}F -CRP reference power adjustments and to acquire images for quantification (Figure 1B). Afterward, it was removed to acquire in vivo ^{19}F images (Figure 1C–E).

2.3 | Sample and animal preparation

Table 1 summarizes all MR measurements, RF coils, and samples used.

Perfluoro-15-crown-5-ether (1200 mM PFCE; Fluorochem, Hadfield, United Kingdom; $f \approx 376.629$ MHz) nanoparticles were prepared as described.^{27,28}

To characterize ^{19}F -CRP B_1 fields, B_1 maps and RARE images were used as follows:

- Low- T_1 uniform phantom: 15-mL tube (ID = 14.6 mm, length = 120 mm, wall thickness = 0.8 mm; Fischer Scientific, Waltham, MA, USA) with 33.3% 2,2,2-trifluoroethanol (Carl Roth & Co., Karlsruhe, Germany; $f \approx 376.633$ MHz) in water with 0.08 mM of gadolinium (Magnevist 0.5 mmol/ml; BayerVital, Leverkusen, Germany) yielding $T_1 \approx 300$ ms.
- High- ^{19}F concentration reference cap (Figure 1B): homogeneous mixture of 60 mM NPs in 1 mL 0.75% agarose (dimensions 20×15 mm²; thickness ≈ 1.5 mm) sealed within PARAFILM (thickness = 0.14 mm; Sigma-Aldrich, St. Louis, MO, USA).

Both sets of maps were acquired separately to consider tube thickness (0.8 mm). This accounts for more than half the number of pixels of the reference cap.

Phantoms and mice were used to evaluate the performance of the B_1 correction methods as follows:

- Test uniform phantom: 15-mL tube containing 0.2 mM of 2,2,2-trifluoroethanol in water. To achieve $T_1 \approx 1870$ ms (in vivo PFCE-NPs T_1 ; see section 3), 0.006 mM gadolinium was used.
- In vivo and ex vivo mice: EAE was induced in female SJL/J mice as described.²⁶ Animals were weighed and scored (0–5) daily for disease signs. Intravenous injections of ^{19}F -NPs (10 μmol PFCE in 200 μL) were administered daily from day 5 following EAE induction until the experiment end. Respiration and temperature

were monitored during measurements. All animal experiments were approved by the Animal Welfare Department of the LAGeSo in Berlin and in accordance with international guidelines (86/609/EEC).

In vivo ^{19}F -NPs T_1 for *model-based corrections* was calculated in $n = 3$ EAE mice using a combination of ketamine-xylazine (initial dose 400 μL , followed by 100–200 μL injections administered intraperitoneally every 45 minutes until the end of the MR examination) to avoid confounding ^{19}F signal. Ex vivo T_1 of PFCE-NPs was computed on $n = 3$ ex vivo phantoms prepared as described subsequently.

In vivo ^1H and ^{19}F images were acquired on another $n = 3$ EAE mice from which $n = 2$ animals are shown. These were anesthetized with isoflurane (2% initial dose, 0.5%–1% maintenance). ^1H - and ^{19}F -MRI of an ex vivo phantom containing the central nervous system (CNS) of a EAE mouse perfused/fixed as described⁸ and embedded in a 15-mL tube filled with 4% paraformaldehyde (Santa Cruz Biotechnology, Dallas, TX, USA) were also performed.

- A reference cap (24 mM NP emulsion) was prepared as described previously for ^{19}F -CRP adjustments and signal quantification of in vivo and ex vivo mice. A similar construction of smaller dimensions (10×5) mm³ was prepared to fit within the volume resonator.

2.4 | Magnetic resonance experiments

^{19}F -CRP reference power calibrations were performed on a 1-mm slice parallel and close to the probe surface. All images were acquired as repetitions in axial and sagittal orientation. Noise scans (number of excitations [NEX] = 1 and reference power = 0 W) were acquired after each RARE image for SNR map computation.

2.4.1 | ^{19}F -CRP B_1 field characterization

The B_1 fields of the ^{19}F -CRP were characterized.²³ Separate sets of maps were determined using the low- T_1 uniform phantom and the high- ^{19}F concentration reference cap as follows:

- Flip angle (FA) mapping: FLASH measurements with TE/TR = 2.16/3000 ms, FOV = (25 \times 25) mm², matrix = 96 \times 96, 5 slices (gap/thickness = 0.5/2 mm), 1 hour per orientation; FA = 60°/120°/240° (uniform phantom) and FA = 60°/120° (reference cap).
- B_1 mapping: FLASH measurements with parameters as described previously and FA = 5° in both cases.

TABLE 1 Detailed overview of measurements, RF coils, and samples used

Purpose	MR protocol	RF coil	Nucleus	Sample(s)	Acquisition time ^a
Acquired images (¹³ F-CRP, anatomical, and references):					
Test images and corresponding anatomical images	FLASH	72-mm linear volume resonator	¹ H	Ex vivo mouse phantom	30 minutes per orientation
	RARE	CRP	¹⁹ F	In vivo mice	15 minutes per orientation
	RARE	CRP	¹⁹ F	24-mM ref. cap (ex vivo, in vivo)	15 minutes per orientation
				Test uniform phantom	3 seconds
				Ex vivo phantom	6 hours per orientation
				In vivo mice	45 minutes per orientation
Reference images for comparison and corresponding anatomical images	FLASH	¹ H/ ¹⁹ F-volume resonator	¹ H	Ex vivo mouse phantom	30 minutes per orientation
	RARE	¹ H/ ¹⁹ F-volume resonator	¹⁹ F	24-mM ref. cap (ex vivo only)	30 minutes per orientation
	RARE	¹ H/ ¹⁹ F-volume resonator	¹⁹ F	Test uniform phantom	1 hour
T ₁ mapping for uniform phantom	RARE with variable TR	¹ H/ ¹⁹ F-volume resonator	¹⁹ F	Ex vivo phantom	6 hours per orientation
				Test uniform phantom	24 minutes
T ₁ values of PFCE-loaded NPs	Non-localized MRS PRESS	¹ H/ ¹⁹ F-volume resonator	¹⁹ F	24-mM and 60-mM ref. caps	35 minutes
				Ex vivo phantoms (n = 3)	30 minutes
				In vivo mice (n = 3)	1 hour 8 minutes
Sensitivity correction:					
Uniform phantom images	RARE	CRP	¹⁹ F	Low-T ₁ uniform phantom	1 hour per orientation
Model-based correction:					
FA and B ₁ mapping	FLASH	CRP	¹⁹ F	Low-T ₁ uniform phantom	1 hour per FA and orientation
	FLASH	CRP	¹⁹ F	Highly fluorinated ref. cap	1 hour per FA and orientation

Abbreviation: CRP, cryogenically-coded transverse surface RF probe; FA, flip angle; NPs, nanoparticles; ref., reference.

^aIndicative values: Scan times may vary when using different scan parameters (e.g., spatial resolution, echo train length, TR).

For the *sensitivity correction method*, RARE images of the low- T_1 uniform phantom were acquired (TE/TR = 4.62/1000 ms, same geometry, echo train length (ETL) = 32, bandwidth = 50 kHz, centric encoding with flipback, 1 hour per orientation). All ^{19}F -RARE images were measured using these scan parameters with varying acquisition times.

2.4.2 | T_1 relaxation times (reference, ex vivo, in vivo) of PFCE-NPs

Due to the inherent ^{19}F characteristics (low SNR, signal sparsity, lack of an a priori known location), determining in vivo T_1 with T_1 mapping was unfeasible. We applied MRS techniques using the $^1\text{H}/^{19}\text{F}$ volume resonator as follows:

- Non-localized spectroscopy (block pulse, 10 TRs [250–10 000 ms], number of acquisitions [NA] = 64, acquisition time [TA] = 35 minutes) to compute T_1 values of the two reference caps (24 mM, 60 mM).
- Localized spectroscopy (PRESS) to compute T_1 values in the brain after ^{19}F -NP administration in ex vivo phantoms ($n = 3$, 12 TRs [250–15 000 ms], NA = 64, TA = 32 minutes) and in vivo mice ($n = 3$, 8 TRs [412.5–13 000 ms], NA = 128, TA = 1 hour 8 minutes). A default B_0 field map was measured before each experiment to optimize shim adjustment (MAPSHIM) computed on ^1H using a 3D cuboid shape fitting the mouse brain.

2.4.3 | Uniform phantom MR measurements

A ^{19}F -MR image of the test uniform phantom was acquired with the ^{19}F -CRP (RARE: same parameters, 3 seconds, axial orientation) to assess B_1 correction performance in low SNR scenarios far from the probe surface. A reference ^{19}F image (RARE: same parameters, 1 hour) and a T_1 map (RARE with variable TR [250–10 000 ms], ETL = 2, linear phase encoding, other parameters same as RARE scan, 24 minutes) were acquired with the $^1\text{H}/^{19}\text{F}$ volume resonator for comparison.

2.4.4 | Ex vivo and in vivo MR measurements

Slice planning and anatomical images (FLASH: TE/TR = 3/120 ms, same FOV, matrix = 256×256 , TA = 30/15 minutes per orientation ex vivo and in vivo, respectively) were acquired with the 72-mm volume resonator.

^{19}F -MR images were measured with the ^{19}F -CRP with (RARE: same parameters, 15 minutes per orientation both ex vivo and in vivo) and without (RARE: same parameters,

6 hours/45 minutes per orientation ex vivo and in vivo, respectively) reference cap.

Reference images were acquired with the $^1\text{H}/^{19}\text{F}$ volume resonator in ex vivo phantoms: reference cap (^{19}F RARE: same parameters, 30 minutes per orientation) and phantoms (^{19}F RARE: same parameters, 6 hours per orientation; ^1H FLASH: same parameters, 1 hour per orientation).

2.5 | Data analysis

Data analysis was performed using *MATLAB* (The MathWorks, Natick, MA, USA).

2.5.1 | MRI data preprocessing

All data followed the same pre-processing workflow:

1. Complex averaging over smaller subsets of the total number of repetitions to mimic different scan times followed by a sum-of-squares (SoS) combination of the two channels (^{19}F -CRP):
 - Uniform phantom: one subset of a 3-second acquisition.
 - Ex vivo phantoms: four subsets corresponding to 15-minute and 1-3-6-hour acquisitions. Same with $^1\text{H}/^{19}\text{F}$ volume resonator for comparison.
 - In vivo mice: three subsets corresponding to 15-30-45 minutes.
 - Reference caps: one subset corresponding to the total scan time.
2. Noise bias correction:²⁹
 - ^{19}F -CRP: noncentral χ distribution²³ using a lookup table for $n = 2$ channels.³⁰
 - Volume resonator: Rician distribution²³ using a lookup table for $n = 1$ channels.³⁰
3. Thresholding (SNR cutoff = 3.5) and removal of isolated groups of < 3 connected pixels.

2.5.2 | ^{19}F -CRP B_1 field characterization and RARE SI model computation

The B_1 maps were computed and denoised as detailed²³ (10th-order and 8th-order polynomials for the low- T_1 uniform phantom and the high- ^{19}F concentration reference cap, respectively).

The RARE SI model was calculated as a function of FA and T_1 relaxation value ($\text{SI} = f(\text{FA}, T_1)$) using extended phase graphs^{31–33} (EPGs). This algorithm provides a tool that depicts the magnetization response and allows computing echo intensities in multi-pulse MR sequences.

RARE scans with the same MR parameters as above were simulated for 20 equispaced T_1 values (150–2050 ms) and 32 excitation FAs (5° – 160° in 5° steps). Finally, an 8th-degree polynomial was fitted²³ to the simulated data for faster computation of results for arbitrary FAs and T_1 values, which did not introduce any oscillations or error within the desired parameter space ($R^2 = 1.0$, root-mean-square-error (RMSE) = 5.5×10^{-4}).

2.5.3 | T_1 relaxation times (reference, ex vivo, in vivo) of PFCE-NPs

PFCE-NPs typically show a single peak at $f \approx 376.629$ MHz. A Lorentzian line-broadening (factor = 70) and automatic phase correction (TopSpin 2.1) were applied. To compute T_1 values from MRS data, peak values were fitted as SI vs. TR datapoints on an exponential growth. Mean values and SDs were computed. T_1 values were used to correct B_1^+ using the *model-based method*.

2.5.4 | B_1 correction methods

The B_1 of ^{19}F -CRP images was corrected using the *sensitivity* (uniform phantom) and *model-based* (reference caps, phantoms, and in vivo mice) methods.²³ All post-processing was performed using software openly available on Github (pramosdelgado/B1correction-toolkit).

2.5.5 | ^{19}F signal quantification

The 24-mM reference cap was used as reference to determine absolute ^{19}F concentrations as follows:

$$c_{\text{sample}} = \frac{\overline{SI}_{\text{sample}} \times c_{\text{ref}}}{SI_{\text{ref}}} \quad (1)$$

where $\overline{SI}_{\text{sample}}$ and SI_{ref} are the SIs for the sample and the reference, respectively, and c_{sample} and c_{ref} are the corresponding concentrations. To compute SI_{ref} , a square-shaped region of interest (ROI; 3×3 pixels) was selected in a B_1 -corrected homogeneous region, in the center of the reference cap.

2.6 | Monte Carlo SNR simulations to estimate the ^{19}F concentration uncertainty

Given the sparse nature of ^{19}F images and the spatially varying B_1 fields of the ^{19}F -CRP, we computed concentration uncertainty maps after B_1 correction as follows (Figure 2):

Step 1. Monte Carlo SNR simulations^{34,35} (1000 iterations) were performed using measured (T_1 values) and synthetic data (SI computed using the simulated RARE SI model). Simulation parameters (Table 2) were defined to mimic realistic excitation FAs, B_1^- -values, and SNRs within the sample. Shorter parameter ranges were chosen for the reference cap after inspection of the central region of the FA, B_1^- , and SNR maps obtained (section 2.5.5). This was crucial to reduce matrix size and avoid memory problems.

Step 2. Noise levels for the prescribed SNR values were fixed for a 90° excitation and $B_1^- = 1$ using a “reverse model-based correction” (inverse steps of the *model-based correction*²³).

Step 3. For each combination of reference and sample FA, B_1^- and T_1 values, the CRP SI (for reference and sample) was calculated and separated into two channels. For each Monte Carlo iteration, complex Gaussian noise was added to both channels, and a SoS reconstruction was computed to simulate a noncentral χ distribution. A noise bias correction was performed as described, followed by a *model-based correction*. Finally, the concentration was estimated using equation (1). The mean SNR and mean and SD of the corrected SI throughout the 1000 iterations were determined for both reference and sample, along with the mean and SD of the concentration. Since the Monte Carlo samples conformed to a Gaussian distribution of mean ≈ 1 (section 3), the corresponding uncertainties in corrected SI and concentration were defined as $\text{SD} \times 100$ (%).

Step 4. To compute the uncertainty map of an acquired ^{19}F image, measured data (FA, B_1^- , and SNR maps, T_1 value) were fed to the corresponding Monte Carlo uncertainty model. The uncertainties were interpolated pixel-wise using a simple linear regression after logarithmically transforming the SNR and uncertainty data and eliminating SNR values < 1 .

2.7 | Correction method evaluation and validation

B_1 correction methods were validated using the following methods on the uniform phantom:

2.7.1 | Central profile plots of uniform phantoms

We quantified the improvement in image homogeneity by plotting normalized vertical SI profiles of original, corrected, and reference images against the distance from the CRP surface.

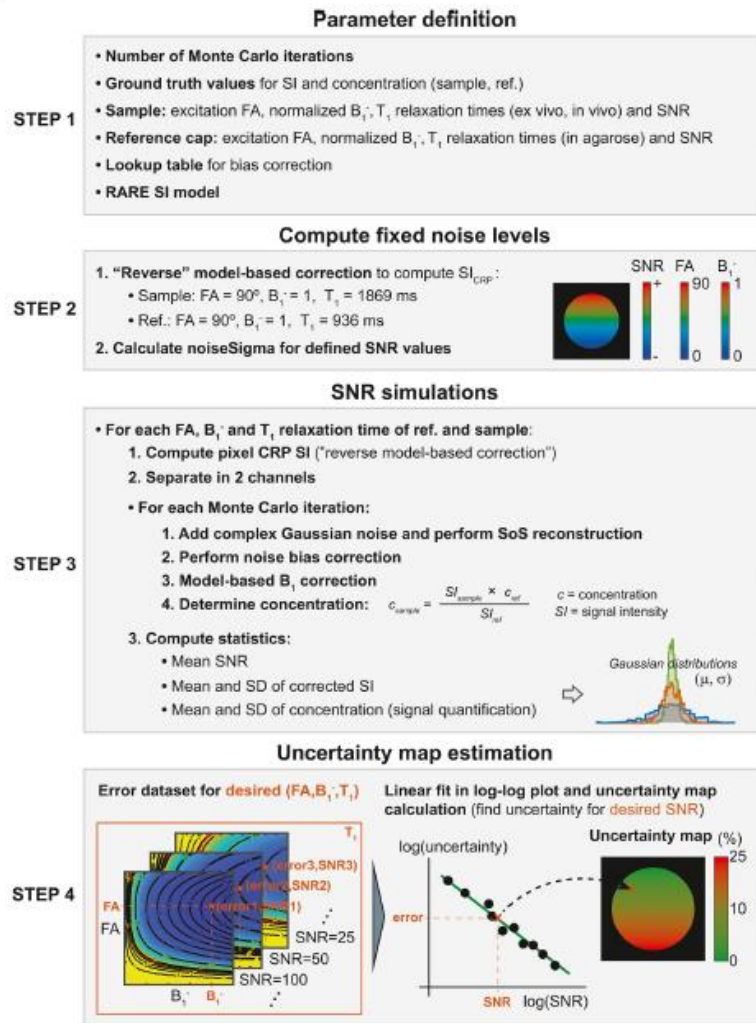


FIGURE 2 Monte Carlo SNR simulation and uncertainty map estimation workflow using measured and synthetic data. After determining the noise levels for the defined SNR values, Monte Carlo simulations are performed for each flip angle (FA), B_1^- , and T_1 relaxation time of the sample and reference by adding noise, computing a noise bias correction, and calculating a model-based B_1^- correction. Concentration was also estimated. Statistics including mean SNR, mean and SD of corrected signal intensity (SI), and mean and SD of the concentration were computed after each run. These simulations are then used to derive uncertainty maps for the measured data using the FA, B_1^- , T_1 , and SNR measured at each pixel using a linear regression in a log-log plot (error vs. SNR). Abbreviations: Ref., reference; SoS, sum-of-squares

TABLE 2 Summary of simulation parameters for Monte Carlo SNR simulations

Parameters	Initialization values	Ranges and steps	Number of elements
Ground-truth data			
Ground-truth SI sample	1	–	1
Ground-truth SI reference cap	1	–	1
Ground-truth concentration reference cap	1	–	1
Sample data			
Excitation FA (relative to 90°)	5°–130°	1° steps	126
Normalized B ₁	0–1	0.01 steps	101
SNR values (fixed at 90° excitation)	0–1500	0–10 in 0.5 steps 11–25 in 1.0 steps 27.5–100 in 2.5 steps 105–500 in 5 steps 510–1500 in 10 steps	246
T ₁ values	936 ms, 818 ms, 1869 ms	–	3
Reference cap data			
Excitation FA (relative to 90°)	50°–60°	5° steps	3
Normalized B ₁	0.8–0.7	0.05-steps	3
SNR value (fixed at 90° excitation)	500	–	1
T ₁ values	936 ms	–	1

2.7.2 | Image homogeneity assessment

The percentage of integral uniformity (PIU)³⁶ was computed for three internally tangential circular ROIs with increasing diameter placed on the central vertical line filling the region with signal.

2.7.3 | Quantification performance

Ten ROIs were placed at pseudo-randomized positions (Figure 5B) on original, corrected, and reference images. Mean absolute percentage errors (MAPEs) were computed relative to the reference (volume resonator) images, as follows:

$$MAPE = \frac{|\overline{SI}_{reference} - \overline{SI}_{corrected}|}{\overline{SI}_{reference}} \times 100 (\%)$$

where $\overline{SI}_{reference}$ and $\overline{SI}_{corrected}$ are the mean SI in reference and corrected images.

A value was calculated for the original image and the three corrections summing over an increasing number of ROIs (top to bottom), with increasing distances from the CRP surface and decreasing SNR. Corrections were classified as excellent (MAPE ≤ 10%, green), good

(10% < MAPE ≤ 25%, orange), or unacceptable (MAPE > 25%, red).

2.7.4 | Statistics

Normality was assessed using the D'Agostino-Pearson test. Because none of the MAPEs on original or corrected data conformed to a Gaussian distribution, a Friedman non-parametric one-way repeated-measures ANOVA test was used followed by Dunn's post-hoc test, in which all corrections were compared to original data (*p*-values < 0.001 were considered significant). The statistical analysis was performed using *GraphPad Prism 5* (GraphPad Software, La Jolla, CA, USA).

3 | RESULTS

3.1 | ¹⁹F-CRP B₁-field characterization and RARE SI model

The sensitivity maps (Figure 3A,D) and the FA maps (relative to an excitation FA = 90°, Figure 3B,E) of the ¹⁹F-CRP revealed a strong decline with increasing distance from the RF probe surface, in both axial and sagittal orientations.

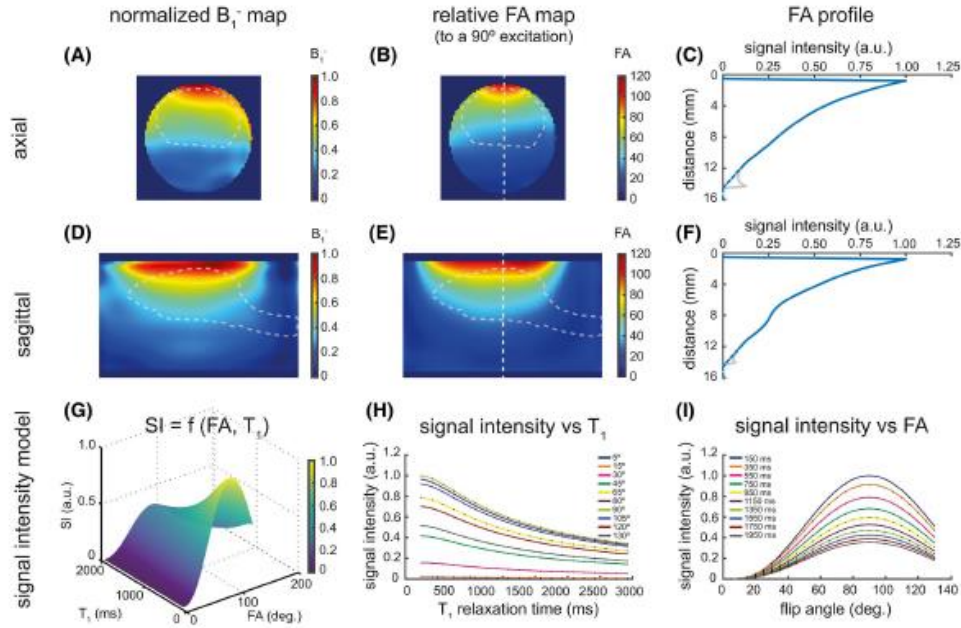


FIGURE 3 B_1 field maps of the quadrature ^{19}F cryogenically-cooled transceive surface RF probe (^{19}F -CRP) and SI model used. (A–E) B_1 and relative FA maps to a 90° excitation FA in axial (A,B) and sagittal (D,E) orientation. The expected position of the mouse brain relative to the ^{19}F -CRP is outlined as a dashed gray line. (C,F) Corresponding normalized central vertical profiles. The gray line depicts the artifact miscalculated by the polynomial fit at low-SNR regions far away from the RF probe surface. The physically correct value is depicted using blue dotted lines. The simulated 3D SI model (G) shows the dependency of the rapid acquisition with refocused echoes (RARE) SI on the T_1 relaxation time and FA. H,I, The 2D-projections of SI vs. T_1 and SI vs. FA, respectively

The B_1^+ inhomogeneity is clearly depicted in Figure 3C (axial) and Figure 3F (sagittal), which show the normalized central vertical profile lines. The maximum distance until which there is signal above the detection threshold ($\text{SNR} > 3.5$) is, in this case, approximately 14.6 mm from the CRP surface.

Figure 3G shows the 3D view of the RARE SI model simulated using EPG simulations. The SI was modeled as a function of FA and T_1 . The SI demonstrates a lower SI with increasing T_1 (Figure 3H) and maximal SI for FA = 90° (Figure 3I). When using EPG simulations, the *hybrid* and *sensitivity methods* yielded the same results up to a constant factor (Supporting Information). Therefore, we only used the *sensitivity* and *model-based correction* moving forward.

3.2 | T_1 relaxation times (reference, ex vivo, in vivo) of PFCE-loaded NPs

Calculated T_1 values for PFCE-NPs in agarose (reference caps, 935.9 ± 10.0 ms) using non-localized MRS agreed

with previously published values at 9.4 T.^{37,38} T_1 values of ^{19}F -NPs in inflammatory lesions in the brain (PRESS) were 818.1 ± 13.4 ms (ex vivo) and 1868.7 ± 43.9 ms (in vivo). This indicated an effective reduction of 117.8 ms in T_1 for ex vivo compared to the reference caps, and an increase of nearly 1 second in T_1 in vivo measurements. Exemplary spectra are shown in Supporting Information Figure S1.

3.3 | Monte Carlo SNR simulations to estimate the ^{19}F concentration uncertainty

Figure 4A–C shows the concentration uncertainty (uncertainty = $\text{SD} \times 100$ [%]) for all FAs/ B_1^+ and three SNR values fixed for FA = 90° , $B_1^+ = 1$, and $T_1 = 1869$ ms (in vivo). For the reference, representative values (FA = 60° , $B_1^+ = 0.8$) were used. The level of uncertainty increases with decreasing FAs and B_1^+ . This trend is more pronounced for regions farther away from the RF probe surface. The contour lines represent SNR values. The green and red

isolines depict the border of the regions where uncertainty $\leq 10\%$ and $\leq 25\%$, respectively. These borders occur at $\text{SNR} \approx 10.1$ and $\text{SNR} \approx 4.25$, respectively, independent of the FA/B_1^- and SNR combination.

We studied the linear dependence of the SD of both corrected SI and concentration on SNR for exemplary data ($\text{FA} = 90^\circ$, $B_1^- = 1.0$, in vivo T_1) using the *model-based method* (Figure 4D, linear fit, dashed orange line). The corrected SI of the sample (blue dots) demonstrated a linear trend throughout the SNR range. The concentration SD (green boxes) was linearly dependent on the sample SNR until an $\text{SNR} \approx 160$ ($\text{SD} = 7 \times 10^{-3}$), after which it asymptotically approached a constant value of approximately 3.5×10^{-3} (uncertainty = 0.35%) due to small but non-negligible errors in the B_1^- -corrected data.

Finally, Figure 4E shows histograms and error bars³⁹ of the concentration calculated over the 1000 iterations corresponding to the three depicted example points ($\text{FA} = 70^\circ$, $B_1^- = 0.8/0.4/0.2$ as colored crosses on Figure 4C). The concentration samples exhibited a Gaussian shape with mean ≈ 1 ($\mu_1 = 1.0003$, $\mu_2 = 0.9964$, $\mu_3 = 0.9834$) and increasing SD ($\sigma_1 = 0.0564$, $\sigma_2 = 0.1199$, $\sigma_3 = 0.2529$) with decreasing SNR, as expected. This demonstrated that the model recovered SIs without introducing bias. Randomness was propagated such that the variability of the corrected SI (i.e., its SD) increased with decreasing SNR.

3.4 | Uniform phantom MR measurements

3.4.1 | Corrected images

B_1^- correction performance was assessed in a low-SNR scenario at regions far from the probe surface using a low-concentration uniform phantom and a short acquisition. The SNR map is shown in Figure 5A. The original image shows a steep SI decay away from the RF probe surface, typical of transceive surface RF coils (Figure 5B). Compared with the reference image, B_1^- -corrected images (Figure 5C,D) yielded uniform SIs over the FOV (Figure 5E). A ghosting artifact due to fast RARE imaging is present in the uniform phantom image used for the *sensitivity method*, and in the test uniform phantom, producing an overshoot in the sensitivity-corrected image far from the probe surface.

3.4.2 | Central profile plots

Corrected SI profiles demonstrated close correspondence with the reference RF coil (green area) up to a distance of approximately 6–7 mm from the CRP surface for our

specific scanning parameters, dimensions of the RF coil, and SNR (Figure 5F).

3.4.3 | Image homogeneity assessment

The calculated PIU in the reference image was 91.4% within the largest ROI (distance from CRP surface = 7.8 mm), indicating no substantial inhomogeneities across the image. In contrast, a PIU of 13.6% was computed for the original image within the same ROI. Corrections yielded improved PIUs (56.7% for *model-based* and 32.4% for *sensitivity corrections*). In general, PIU degrades with increasing distance from the RF probe, where acquired image artifacts prevail (Figure 5H).

3.4.4 | Quantification performance and statistics

According to our MAPE classification, only the *model-based correction* provided excellent results for SNRs between 38 and 7 (Figure 5G; ROIs = 1–7, distance = 2.1–6.3 mm). Uncorrected images showed high errors within this SNR range (84.7 \pm 85.8%). Within this region (distance = 2.1–6.3 mm), the *model-based correction* performed best (7.7 \pm 4.7%), followed by the *sensitivity correction*, which yielded good results (12.2 \pm 8.2%). Both corrections provided equally good results (*model-based* 16.2 \pm 16.5%, *sensitivity* 19.7 \pm 16.6%) up to the eighth ROI (distance = 2.1–6.5 mm), in contrast to uncorrected images (89.9 \pm 95.6%). When considering all ROIs (distance = 2.1–7.6 mm), only the *model-based correction* (19.7 \pm 18.9%) yielded good results. In this case, the *sensitivity correction* provided unacceptable results (35.5 \pm 33.3%), but was still lower than the MAPE of uncorrected images (105.8 \pm 125.9%). Figure 5G also shows similarities between the proposed ranges using simulations (uncertainty $\leq 10\%$ when $\text{SNR} \geq 10.1$ and uncertainty $\leq 25\%$ when $\text{SNR} \geq 4.25$) and experimental results.

The *model-based correction* performed best overall, significantly reducing quantification errors compared with original mean errors (both B_1^- correction methods $p < 0.001$; Figure 5I). Therefore, this method was used for further B_1^- corrections.

3.5 | Ex vivo MR measurements

Concentration maps of the ex vivo EAE phantom were computed for different measurement times (15 minutes [NEX = 300], 1, 3, and 6 hours [NEX = 1200/3600/7200]) using the 24-mM reference cap in images acquired with the reference

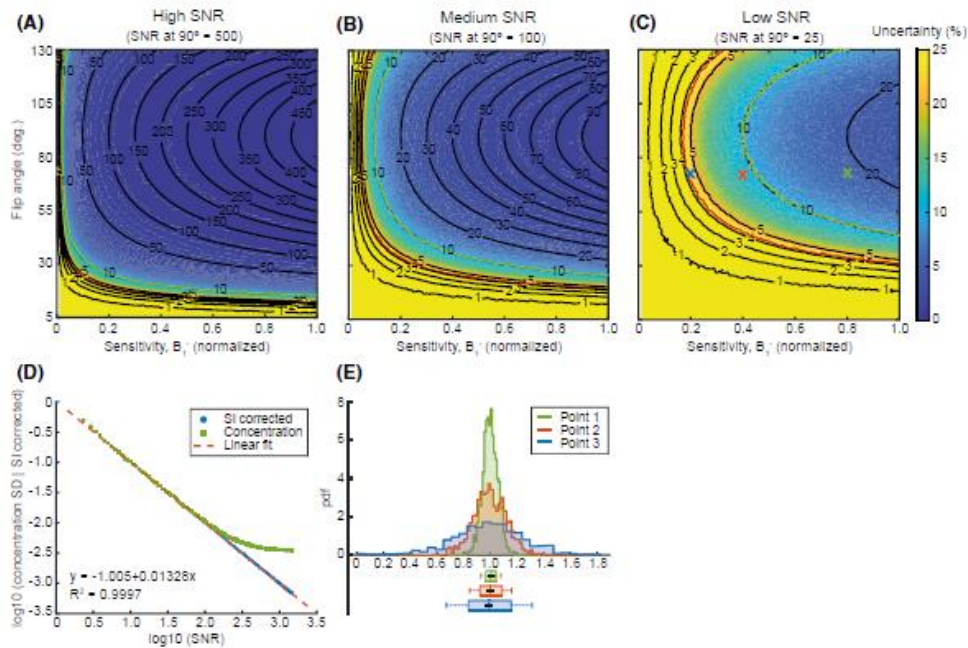


FIGURE 4 The SNR simulation results corresponding to a *model-based correction* for $T_1 = 1869$ ms (in vivo mouse) for SNR = 1000 (A), SNR = 500 (B), and SNR = 25 (C), fixed for a 90° excitation and $b_1^- = 1$. The contour lines represent equal SNR values (in black), and uncertainties of $\leq 10\%$ (in green) and $\leq 25\%$ (in red). (D) Linear dependence on the SD of the corrected SI and SNR, and quasi-linear dependence on the SD of the concentration and SNR (log-log plot). (E) Histogram from the Monte Carlo samples for the three points depicted in (C). In all three cases, the distributions exhibit a Gaussian distribution of mean ≈ 1 and increasing SDs (uncertainties) with decreasing SNR

volume resonator (Figure 6A) and original ^{19}F -CRP images (Figure 6B). Qualitative comparison of the reference images after 3 hours and original CRP images after 15 minutes revealed distinct similarities, demonstrating the remarkable SNR capabilities of the CRP. However, the ^{19}F signal at the lymph nodes, indicating accumulation of ^{19}F -labeled inflammatory cells (white arrows) in reference images was absent in the ^{19}F -CRP images, as the lymph nodes are located too far away from the CRP surface to be detected.

Assessment of the ^{19}F concentration shown by original CRP images and corresponding *model-based* B_1 -corrected images (Figure 6D) demonstrated that correction considerably improved the concentration estimation, compared with reference images (ground truth). The SNR maps from original CRP images showed the expected increase of SNR with scan time (Figure 6C), translating to fewer uncertainties in concentration (Figure 6E). Overall, the uncertainty maps indicated the reliability of the B_1 -corrected concentration maps, with most

pixels being green (uncertainty $\leq 10\%$) or orange ($10\% <$ uncertainty $\leq 25\%$). Images corresponding to the axial orientation are shown in Supporting Information Figure S2.

3.6 | In vivo MR measurements

We studied the performance of the *model-based correction* in a typically time-constrained and low-SNR in vivo EAE ^{19}F -MRI experiment.

The first animal shown (Figure 7) exhibited severe clinical symptoms (score = 2.5), whereas the second (Figure 8) presented moderate clinical symptoms (score = 1.5). Images were acquired in axial and sagittal orientations for 15, 30, and 45 minutes (NEX = 300/600/900). Images corresponding to the axial orientation are shown in Supporting Information Figures S3 and S4.

Concentration maps of uncorrected images of mouse 1 (Figure 7A) showed an overestimation of ^{19}F

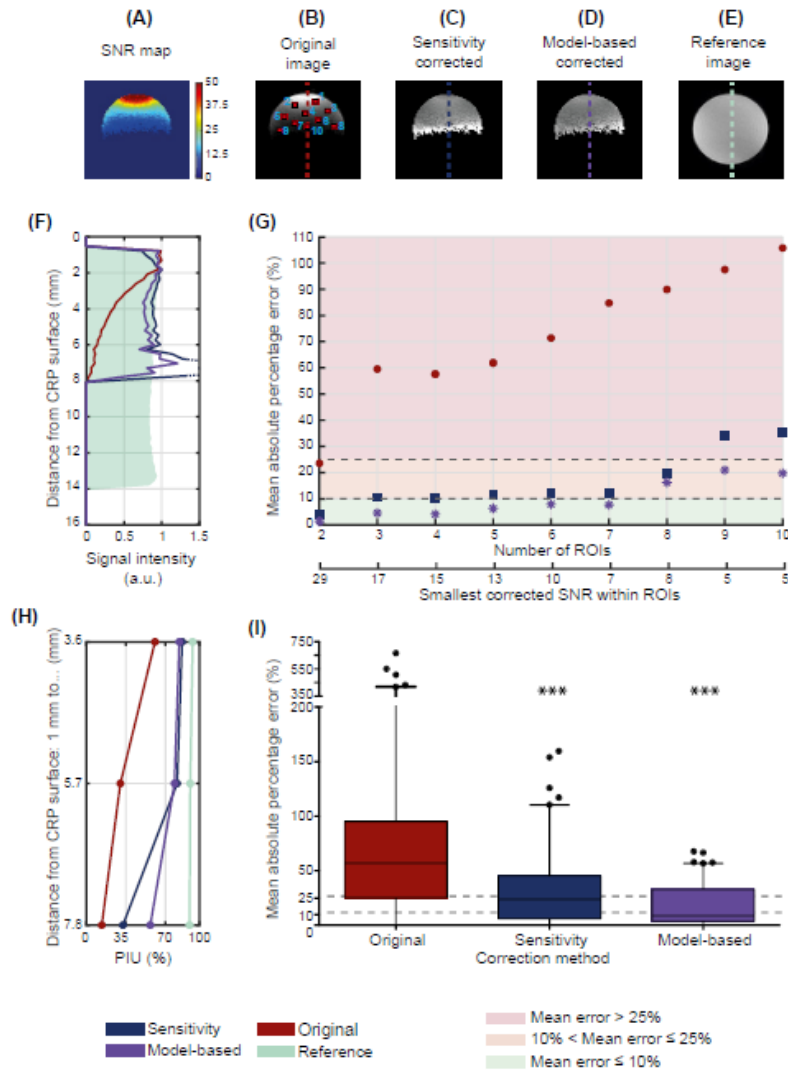


FIGURE 5 Uniform phantom validation. (A) SNR map, (B) original (C,D) corrected, and (E) reference images, respectively. The original image includes the placement of the 10 regions of interest (ROIs) selected for error calculations. (F) Normalized SI profiles perpendicular to the RF coil surface. (G) Mean absolute percentage error (MAPE) of original and corrected images for an increasing number of ROIs demonstrates a remarkable reduction in errors after B_1 correction compared to original images. The *model-based correction* provides quantitatively good results in regions far from the RF probe. (H) Percentage of integral uniformity (PIU) of corrected images shows a quantitative improvement in homogeneity in comparison with original images. (I) Statistical assessment of SI accuracy. Whiskers represent the 5th and 95th percentiles. Asterisks indicate statistical significance compared to uncorrected images

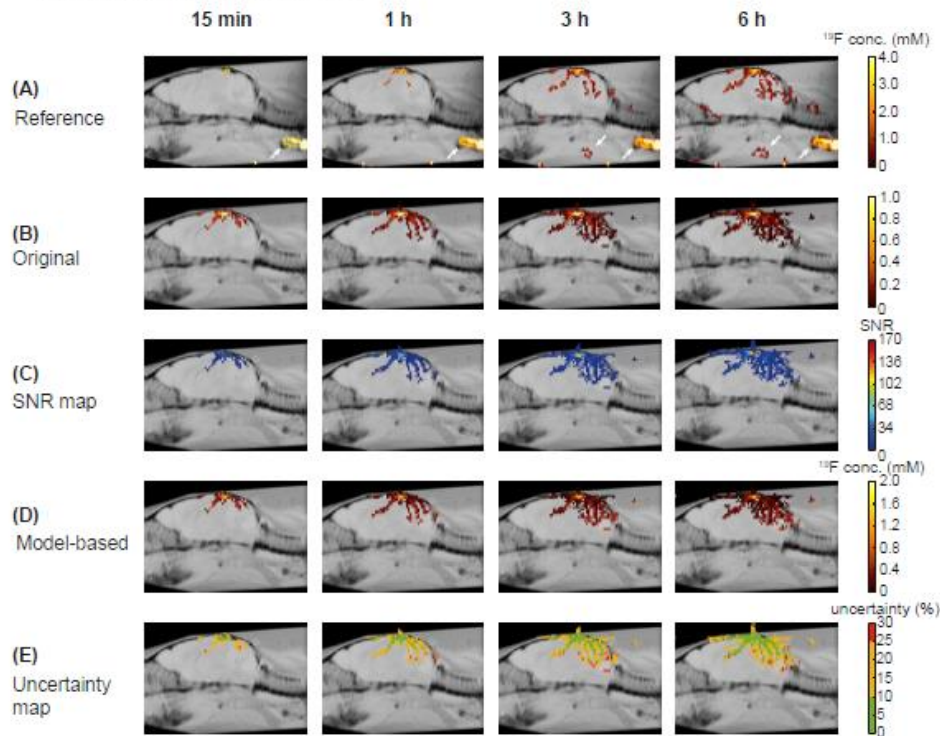


FIGURE 6 Ex vivo phantom validation. Sagittal views of an ex vivo experimental autoimmune encephalomyelitis (EAE) mouse (score = 2.0) for increasing scan times (15 minutes, 1 hour, 3 hours, and 6 hours). Reference images (A) show impressive ^{19}F signal in the lymph nodes, not visible with the ^{19}F -CRP (B), since they are located too far away from the CRP surface to be detected. Distinct similarities when comparing CRP images after 15 minutes and those acquired with the volume resonator after 3 hours demonstrate the remarkable SNR capabilities of the CRP. (C) The SNR maps for the CRP images. (D) After performing the B_1 correction, images show concentration values closer to the reference obtained with the volume resonator. (E) Uncertainty maps reveal the reliability of the B_1 -corrected concentration maps, with most pixels indicating green (uncertainty $\leq 10\%$) and orange ($10\% < \text{uncertainty} \leq 25\%$) values

concentrations in regions close to the RF probe surface, which correspond to meningeal inflammatory cell infiltration, common in EAE. White arrows indicate external signals (i.e., in ears and other adjacent tissues), which are not corrected when located outside of the FA/B_1 maps. The SNR maps (Figure 7B) correlate with the original concentration maps.

Following the *model-based B_1 correction*, concentration maps (Figure 7C) showed reduced ^{19}F concentration in regions close to the RF probe and increased ^{19}F concentration in regions with high SNR far from the CRP surface. The reliability of the correction is represented by the concentration uncertainty maps that mostly show values with $10 < \text{uncertainty} \leq 25\%$ (orange pixels) and $\leq 10\%$ (green pixels) especially at higher SNR (Figure 7D).

Compared to mouse 1, mouse 2 presented with more ^{19}F signal, even though its disease score was less severe. This is evident from the original concentration maps (Figure 8A) and corresponding SNR maps (Figure 8B). Mouse 2 exhibited meningeal inflammation, visible as a thin layer of ^{19}F signal with an SNR ranging from 3.6 to 49.5 and ^{19}F concentrations ranging from 0.1 to 1.7 mM, as well as inflammatory cell accumulation in deeper regions of the brain. After applying the *model-based correction* (Figure 8C), concentration maps showed an expected reduction in ^{19}F concentration in the meninges and an increase in features far from the CRP surface. Corresponding concentration uncertainty maps (Figure 8D) demonstrate the reliability of the B_1 corrections, with most pixels being orange ($10\% < \text{uncertainty} \leq 25\%$) and green (uncertainty $\leq 10\%$), especially at higher SNR.

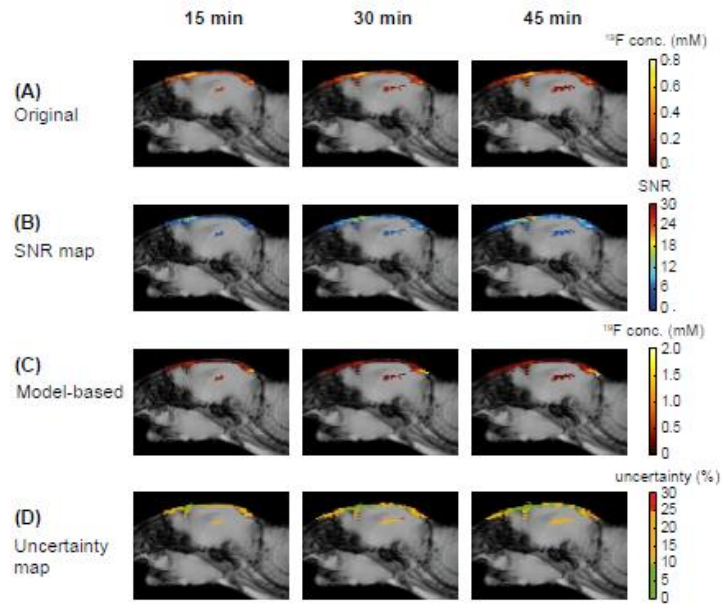


FIGURE 7 In vivo EAE mouse 1 (score = 2.5) in sagittal orientation. Concentration maps of original images (A) show an initial overestimation of the ^{19}F concentration in regions close to the RF probe surface (e.g., meninges), which partly correspond to regions with high SNR (B). (C) B_1 -corrected images present an adjustment in scale, where ^{19}F concentration not only depends on the distance to the CRP surface and SNR (heavily dependent on B_1^+ and B_1^-) but on the ^{19}F -NPs accumulated per pixel. (D) The reliability of the B_1 -corrected concentration maps is presented by the uncertainty maps, which show green (uncertainty $\leq 10\%$) and orange ($10\% < \text{uncertainty} \leq 25\%$) values for most pixels

4 | DISCUSSION

The potential of ^{19}F -MR has long been recognized.^{1,40,41} However, low in vivo ^{19}F concentrations demand SNR-enhancing strategies. Transceive surface RF probes such as the ^{19}F -CRP maximize SNR⁸ but their inhomogeneous B_1 field hampers quantification. To date, efforts in B_1 field correction for ^{19}F -MRI have been scarce, and usually limited to less complex imaging techniques.^{10,19,42,43}

This study builds on our previous work on B_1 correction methods tailored for ^1H transceive surface RF probes and SNR-efficient RARE imaging,²³ to enable ^{19}F signal quantification in low SNR time-constrained scenarios. Low-concentration uniform phantom images showed considerable increase in homogeneity after B_1 correction even in low-SNR regions distal from the coil. Ex vivo concentration maps using reference caps demonstrated substantial improvement in concentration estimation, compared with reference images. We established a method to determine concentration error after B_1 correction using Monte Carlo SNR simulations and an acquisition workflow to

co-localize ^{19}F -CRP images with anatomical images from an external volume resonator. Furthermore, first in vivo ^{19}F -nanoparticle T_1 values were determined in EAE brains to compute *model-based corrections*. Successful implementation ultimately yielded the first quantitative in vivo ^{19}F -MR images of inflamed EAE brains using a ^{19}F -CRP.

Interestingly, differences in T_1 were observed for PFCE-NPs in reference caps, ex vivo, and in vivo. This is in agreement with previous studies showing significant changes in T_1 relaxation as a result of variations in temperature or chemical environment (e.g., pH, different tissue types).^{38,44}

By introducing EPG simulations, here we reduced the burden of our previous strategy of preparing and scanning several samples with different T_1 to compute the RARE SI model.²³ This also improved the accuracy of the model by essentially eliminating possible imprecisions introduced by measurements, especially at low FAs where SIs corresponding to different T_1 s are closer to each other. We found using EPG simulations that the *hybrid* and *sensitivity methods* yielded the same results, up to a constant factor. Imperfections originating from a measured model

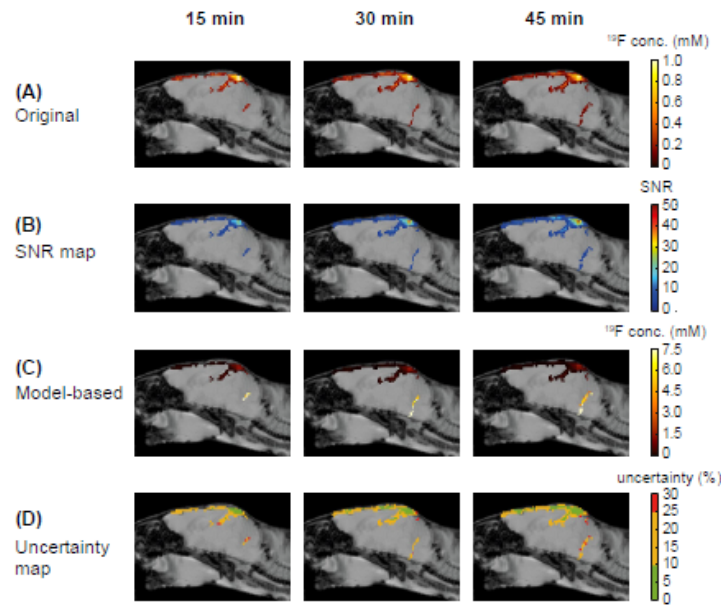


FIGURE 8 In vivo EAE mouse 2 (score = 1.5) in sagittal orientation. (A) Concentration maps of original images present signals in the meninges as well as in deeper regions of the brain, indicating increased inflammatory cell accumulation. (B) The SNR maps show high SNR at pixels at the top of the mouse head and a reduced SNR in regions distant to the RF probe. (C) After applying the *model-based B_1 correction*, concentration maps show an expected reduction in ^{19}F concentration in the meninges and an increase in pixels far from the CRP surface. (D) Corresponding uncertainty maps demonstrate the reliability of the B_1 -corrected concentration maps, with most pixels indicating green (uncertainty $\leq 10\%$) and orange ($10\% < \text{uncertainty} \leq 25\%$) values

instead of EPG simulations disturb the symmetry underlying this degeneracy, leading to slight differences between the *hybrid* and *sensitivity methods*. This demonstrates that simulations have a clear advantage, which we expect would also be true for other MR sequences lacking closed-form SI equations.

The use of higher ETLs to further improve SNR through signal averaging produced ghosting artifacts in uniform phantoms (in test images, but also images used for *sensitivity correction*) in regions where ^{19}F signal was lower. This effect has been widely recognized^{45,46} and produced an abnormal increase of signal with the *sensitivity method* in regions adjacent to the artifact, which could not be removed even when changing the phase-encoding direction. The *model-based correction* was affected to a lesser extent (test images still showed ghosting artifacts), since this correction uses FA and B_1^- maps computed with FLASH images. This was observed when correcting the uniform phantom in which the *model-based correction* yielded MAPEs lower than 25% for all ROIs, and calculated PIUs were equally higher than those achieved with the *sensitivity method*.

Therefore, we conclude that the *model-based correction method* is more robust than the *sensitivity method*, which poses some constraints in MR scanning parameters.

Furthermore, the uniform phantom was prepared with ^{19}F concentration (0.2 mM) and SNR (range 50 to 0) comparable to those achieved in EAE mice administered with PFCE-NPs (maximum ^{19}F concentration 2 mM, SNR between 50 and 0 in all cases). Because in transceive surface RF probes the SNR is much higher when close to the RF probe, the B_1 correction approach and uncertainty propagation model were assessed in realistic scenarios and validated for low SNRs far away from the RF probe (Figure 5F–I).

Reference caps placed above the phantoms or mouse heads were developed to allow for reference power calibrations. Little extra time was needed to acquire separate reference images to compute ^{19}F concentrations. Furthermore, individual B_1 maps were measured to correct more pixels in the reference caps, since the wall thickness of the 15-mL tube (0.8 mm) excluded more than half of the pixels of the reference. Corrections of the reference caps were nevertheless of poorer quality, with B_1 inhomogeneities at the sides.

This was expected due to the large gradient close to the probe surface. Also, reference power adjustments may not be reliable in the close slices, further demonstrating that FA calibration is non-trivial and could be improved.^{42,47}

Reliable B_1 correction is indispensable for robustly quantifying the ^{19}F signal when using the ^{19}F -CRP in studies using ^{19}F -NPs to measure the inflammatory burden in EAE in vivo. In this study we presented two EAE animals with discrepancies between ^{19}F signal and clinical score: the animal with lower clinical severity showed more ^{19}F signal. This reflects the clinico-radiological paradox, well described in MS⁴⁸ and EAE,⁴⁹ whereby clinical status and radiological findings diverge, underscoring the urgent need to establish more quantitative MRI methods to assess disease severity objectively, such as that presented in the current study.

We performed Monte Carlo SNR simulations to estimate SI quantification uncertainties. Simulations were designed to include a wide SNR range (Table 2), taking into account the typically low SNR values for ^{19}F (SNR = 0–10 in 0.5 steps) as well as higher SNRs (SNR up to 1500). We found that concentration uncertainty maps yielded a linear dependence of the uncertainty on SNR, with constant regions ($\leq 10\%$ with SNR ≥ 10.1 and $\leq 25\%$ when SNR ≥ 4.25). This is consistent with the results previously demonstrated for ^1H imaging, in which SNR was not limited. These SNR requirements are highly relevant for the experimental implementation of our approach and aim to guide other researchers to balance scan time with the uncertainty of the quantification of low-SNR ^{19}F RARE-MRI applications.

To examine the accuracy of B_1 -corrected ex vivo concentration maps, these were compared to those obtained with a volume resonator. Despite the best efforts to select an identical anatomical position with both volume resonators, minor differences in ^1H might cause slight changes in the visible ^{19}F signal. Nevertheless, there was overall good agreement in ^{19}F features and corresponding concentrations, confirmed by the computed uncertainty maps. In vivo error concentration maps showed positive results even when SNR values achieved were significantly lower than ex vivo, due to reduced scan times. Future studies using 3D-RARE combined with accelerated acquisition could help further improve concentration errors.^{50,51} Moreover, adiabatic pulses could be an interesting addition to 3D-RARE acquisitions to further improve B_1^+ -field uniformity up to a certain region.^{52,53} A subsequent *model-based* B_1 correction could be of value to increase the B_1 -corrected area.

To conclude, we demonstrated a workflow that allows ^{19}F signal quantification using a *model-based* B_1 correction method together with a single-tuned transceive surface RF probe and RARE. We also highlight several issues that should be considered when performing similar studies. This approach remarkably improved concentration errors from $> 100\%$ to $< 25\%$. B_1 correction methods will

be critical to ensure that the detected ^{19}F signal depends exclusively on ^{19}F spin density and not on distance to the RF probe surface, while utilizing the SNR benefit provided by ^{19}F -CRPs. These results are particularly promising for future clinical applications,^{54–57} in which the lower SNR achieved at clinical field strengths necessitates the use of transceive surface RF probes.

ACKNOWLEDGMENT

The authors thank Rui Pedro A. G. Teixeira (Perspectum, Oxford, United Kingdom), João S. Periquito (Max-Delbrück-Center for Molecular Medicine in the Helmholtz Association, Berlin, Germany and Charité Universitätsmedizin-Berlin), and Andreia C. de Freitas (Instituto Superior Técnico, Lisbon, Portugal) for the helpful discussions about EPG simulations and RARE imaging, and Matthias Weigel (University of Basel, Basel, Switzerland) for generously providing his EPG simulation code. Open access funding enabled and organized by ProjektDEAL.



CONFLICT OF INTEREST

Andre Kuehne, Alonso Vázquez and Helmar Waiczies are employees of MRI.TOOLS, Berlin, Germany. Thoralf Niendorf is founder and CEO of MRI.TOOLS. Andreas Pohlmann is currently an employee of Siemens Healthineers. All other authors declare no conflict of interest.

DATA AVAILABILITY STATEMENT

The code and data that support the findings of this study will be openly available in GitHub at https://github.com/pramosdelgado/B1correction_for_19F.

ORCID

Paula Ramos Delgado  <https://orcid.org/0000-0003-2009-3024>
 Andre Kuehne  <https://orcid.org/0000-0002-4133-5056>
 Mariya Aravina  <https://orcid.org/0000-0002-0970-6080>
 Jason M. Millward  <https://orcid.org/0000-0003-4484-2798>
 Alonso Vázquez  <https://orcid.org/0000-0002-0725-3698>
 Ludger Starke  <https://orcid.org/0000-0002-0359-0101>
 Helmar Waiczies  <https://orcid.org/0000-0001-6651-4790>
 Andreas Pohlmann  <https://orcid.org/0000-0002-8572-2568>
 Thoralf Niendorf  <https://orcid.org/0000-0001-7584-6527>
 Sonia Waiczies  <https://orcid.org/0000-0002-9916-9572>

TWITTER

Paula Ramos Delgado  @pramosdelgado

REFERENCES

1. Ruiz-Cabello J, Barnett B, Bottomley P, Bulte J. Fluorine (^{19}F) MRS and MRI in biomedicine. *NMR Biomed.* 2011;24:114–129.
2. Waiczies S, Ji Y, Niendorf T. Tracking methods for dendritic cells. In: Flögel U, Ahrens E, eds. *Fluorine Magnetic Resonance Imaging*. Pan Stanford Publishing; 2017:243–281.

3. Chen J, Lanza G, Wickline S. Quantitative magnetic resonance fluorine imaging: today and tomorrow. *Wiley Interdiscip Rev Nanomed Nanobiotechnol*. 2015;2:431-440.
4. Axel L, Hayes C. Surface coil magnetic resonance imaging. *Archives Internationales De Physiologie Et De Biochimie*. 1985;93:11-18.
5. Ratering D, Baltes C, Nordmeyer-Massner J, Marek D, Rudin M. Performance of a 200-MHz cryogenic RF probe designed for MRI and MRS of the murine brain. *Magn Reson Med*. 2008;59:1440-1447.
6. Baltes C, Radzwill N, Bosshard S, Marek D, Rudin M. Micro MRI of the mouse brain using a novel 400 MHz cryogenic quadrature RF probe. *NMR Biomed*. 2009;22:834-842.
7. Kovacs H, Moskau D, Spraul M. Cryogenically cooled probes—a leap in NMR technology. *Prog Nucl Magn Reson Spectrosc*. 2005;46:131-155.
8. Waiczies S, Millward JM, Starke L, et al. Enhanced fluorine-19 MRI sensitivity using a cryogenic radiofrequency probe: technical developments and ex vivo demonstration in a mouse model of neuroinflammation. *Sci Rep*. 2017;7:9808.
9. Sack M, Wetterling F, Sartorius A, Ende G, Weber-Fahr W. Signal-to-noise ratio of a mouse brain ¹³C CryoProbe™ system in comparison with room temperature coils: spectroscopic phantom and in vivo results. *NMR Biomed*. 2014;27:709-715.
10. Khalil AA, Mueller S, Foddis M, et al. Longitudinal ¹⁹F magnetic resonance imaging of brain oxygenation in a mouse model of vascular cognitive impairment using a cryogenic radiofrequency coil. *Magn Reson Mater Phys, Biol Med*. 2019;32:105-114.
11. Collins CM, Webb AC. Quadrature surface coils. In: Harris RK, Wasylshen RL, eds. *eMagRes*. Hoboken, NJ: John Wiley & Sons, Ltd; 2010. <https://doi.org/10.1002/9780470034590.emrstm1115>
12. Hoult D, Chen C, Sank V. Quadrature detection in the laboratory frame. *Magn Reson Med*. 1984;1:339-353.
13. Glover G, Hayes C, Pelc N, et al. Comparison of linear and circular polarization for magnetic resonance imaging. *J Magn Reson*. 1985;64:255-270.
14. Peshkovsky AS, Kennan RP, Fabry ME, Avdievich NI. Open half-volume quadrature transverse electromagnetic coil for high-field magnetic resonance imaging. *Magn Reson Med*. 2005;53:937-943.
15. Schnall M, Subramanian V, Leigh J, Chance B. A new double-tuned probe for concurrent ¹H and ³¹P NMR. *J Magn Reson*. 1985;65:122-129.
16. Meyerspeer M, Roig ES, Gruetter R, Magill AW. An improved trap design for decoupling multinuclear RF coils. *Magn Reson Med*. 2014;72:584-590.
17. Crowley M, Evelhoch J, Ackermann J. The surface-coil NMR receiver in the presence of homogeneous B₁ excitation. *J Magn Reson*. 1985;64:20-31.
18. Collewet G, Davenel A, Toussaint C, Akoka S. Correction of intensity nonuniformity in spin-echo T₁-weighted images. *Magn Reson Imaging*. 2002;20:365-373.
19. Vernikouskaya I, Pochert A, Lindén M, Rasche V. Quantitative ¹⁹F MRI of perfluoro-15-crown-5-ether using uniformity correction of the spin excitation and signal reception. *Magn Reson Mater Phys, Biol Med*. 2019;32:25-36.
20. Wang J, Qiu M, Constable R. In vivo method for correcting transmit/receive nonuniformities with phased array coils. *Magn Reson Med*. 2005;53:666-674.
21. Meara S, Barker G. Evolution of the longitudinal magnetization for pulse sequences using a fast spin-echo readout: application to fluid-attenuated inversion-recovery and double inversion-recovery sequences. *Magn Reson Med*. 2005;54:241-245.
22. Conturo T, Beth A, Arenstorf R, Price R. Simplified mathematical description of longitudinal recovery in multiple-echo sequences. *Magn Reson Med*. 1987;4:282-288.
23. Ramos Delgado P, Kuehne A, Periquito J, et al. B₁ inhomogeneity correction of RARE MRI with transceive surface radiofrequency probes. *Magn Reson Med*. 2020;84:2684-2701.
24. Constantinescu C, Farooqi N, O'Brien K, Gran B. Experimental autoimmune encephalomyelitis (EAE) as a model for multiple sclerosis (MS). *Br J Pharmacol*. 2011;164:1079-1106.
25. Robinson A, Harp C, Noronha A, Miller S. The experimental autoimmune encephalomyelitis (EAE) model of MS: utility for understanding disease pathophysiology and treatment. In: Goodin D, ed. *Handbook of Clinical Neurology*, vol. 122. Elsevier BV; 2014:173-189.
26. Waiczies H, Lepore S, Drechsler S, et al. Visualizing brain inflammation with a shingled-leg radio-frequency head probe for ¹⁹F/¹H MRI. *Sci Rep*. 2013;3:1280.
27. Waiczies S, Lepore S, Sydow K, et al. Anchoring dipalmitoyl phosphoethanolamine to nanoparticles boosts cellular uptake and fluorine-19 magnetic resonance signal. *Sci Rep*. 2015;5:8427.
28. Waiczies H, Lepore S, Janitzek N, et al. Perfluorocarbon particle size influences magnetic resonance signal and immunological properties of dendritic cells. *PLoS One*. 2011;6:e21981.
29. Starke L, Niendorf T, Waiczies S. Data preparation protocol for low signal-to-noise ratio fluorine-19 MRI. In: Pohlmann A, Niendorf T, eds. *Preliminary MRI of the Kidney: Methods and Protocols*. Springer US; 2021:711-722.
30. Henkelman R. Measurement of signal intensities in the presence of noise in MR images. *Med Phys*. 1985;12:232-233.
31. Weigel M. Extended phase graphs: dephasing, RF pulses, and echoes—pure and simple. *J Magn Reson Imaging*. 2015;41:266-295.
32. Hennig J. Echoes—how to generate, recognize, use or avoid them in MR-imaging sequences. Part I: fundamental and not so fundamental properties of spin echoes. *Concepts Magn Reson*. 1991;3:125-143.
33. Hennig J. Echoes—how to generate, recognize, use or avoid them in MR-imaging sequences. Part II: echoes in imaging sequences. *Concepts Magn Reson*. 1991;3:179-192.
34. Zhang J. Modern Monte Carlo methods for efficient uncertainty quantification and propagation: a survey. *Wiley Interdiscip Rev Comput Stat*. 2020;13:e1539.
35. Kroese D, Rubinstein R. Monte Carlo methods. *Wiley Interdiscip Rev Comput Stat*. 2012;4:48-58.
36. Price R, Axel L, Morgan T, et al. Quality assurance methods and phantoms for magnetic resonance imaging: report of AAPM nuclear magnetic resonance Task Group No. 1. *Med Phys*. 1989;17:287-295.
37. Jacoby C, Temme S, Mayenfels F, et al. Probing different perfluorocarbons for in vivo inflammation imaging by ¹⁹F MRI: image reconstruction, biological half-lives and sensitivity. *NMR Biomed*. 2013;27:261-271.
38. Prinz C, Ramos Delgado P, Eigentler T, Starke L, Niendorf T, Waiczies S. Toward ¹⁹F magnetic resonance thermometry: spin-lattice and spin-spin relaxation times and temperature dependence of fluorinated drugs at 9.4 T. *Magn Reson Mater Phys, Biol Med*. 2018;32:51-61.
39. *Nhist Function [computer program]*. Version 1.13.0.0. File Exchange: The MathWorks; 2015.

40. Holland G, Bottomley P, Hinshaw W. ^{19}F magnetic resonance imaging. *J Magn Reson*. 1977;28:133-136.
41. Ahrens E, Flores R, Xu H, Morel P. In vivo imaging platform for tracking immunotherapeutic cells. *Nat Biotechnol*. 2005;23:983-987.
42. Goette M, Lanza G, Caruthers S, Wickline S. Improved quantitative ^{19}F MR molecular imaging with flip angle calibration and B_1 -mapping compensation. *J Magn Reson Imaging*. 2015;42:488-494.
43. Constantinides C, Maguire M, McNeill E, et al. Fast, quantitative, murine cardiac ^{19}F MRI/MRS of PFCE-labeled progenitor stem cells and macrophages at 9.4T. *PLoS One*. 2018;13:e0190558.
44. Kadayakkara D, Damodaran K, Hitchens T, Bulte J, Ahrens E. ^{19}F spin-lattice relaxation of perfluoropolyethers: dependence on temperature and magnetic field strength (7.0–14.1 T). *J Magn Reson*. 2014;242:18-22.
45. Zhou X, Liang Z, Cofer G, Beaulieu C, Suddarth S, Johnson G. Reduction of ringing and blurring artifacts in fast spin-echo imaging. *J Magn Reson Imaging*. 1993;3:803-807.
46. Mulkern R, Wong S, Winalski C, Jolesz F. Contrast manipulation and artifact assessment of 2D and 3D RARE sequences. *Magn Reson Imaging*. 1990;8:557-566.
47. Schulte RF, Sacolick L, Deppe MH, et al. Transmit gain calibration for nonproton MR using the Bloch-Siegert shift. *NMR Biomed*. 2010;24:1068-1072.
48. Barkhof F. The clinico-radiological paradox in multiple sclerosis revisited. *Curr Opin Neurol*. 2002;15:239-245.
49. Wuerfel J, Tysiak E, Prozorovski T, et al. Mouse model mimics multiple sclerosis in the clinico-radiological paradox. *Eur J Neurosci*. 2007;26:190-198.
50. Zhong J, Mills P, Hitchens T, Ahrens E. Accelerated fluorine-19 MRI cell tracking using compressed sensing. *Magn Reson Med*. 2013;69:1683-1690.
51. Darçot E, Yerly J, Hilbert T, et al. Compressed sensing with signal averaging for improved sensitivity and motion artifact reduction in fluorine-19 MRI. *NMR Biomed*. 2021;34:e4418.
52. Zhou X. Adiabatic radiofrequency pulses. In: Bernstein M, King K, Zhou X, eds. *Handbook of MRI Pulse Sequences*. Elsevier Academic Press; 2004:177-212.
53. de Graaf R, Rothman D, Behar K. Adiabatic RARE imaging. *NMR Biomed*. 2003;16:29-35.
54. Ahrens E, Helfer B, O'Hanlon C, Schirda C. Clinical cell therapy imaging using a perfluorocarbon tracer and fluorine-19 MRI. *Magn Reson Med*. 2014;72:1696-1701.
55. Amiri H, Srinivas M, Veltien A, van Uden M, de Vries I, Heerschap A. Cell tracking using (^{19}F) magnetic resonance imaging: technical aspects and challenges towards clinical applications. *Eur Radiol*. 2015;25:726-735.
56. Chapelin F, Capitini C, Ahrens E. Fluorine-19 MRI for detection and quantification of immune cell therapy for cancer. *J Immunotherapy Cancer*. 2018;6:105.
57. Fox M, Gaudet J, Foster P. Fluorine-19 MRI contrast agents for cell tracking and lung imaging. *Magn Reson Insights*. 2016;22:53-67.

SUPPORTING INFORMATION

Additional supporting information may be found in the online version of the article at the publisher's website.

FIGURE S1 Exemplary spectra used for T_1 calculation for (A) reference cap containing 24mM ^{19}F -loaded NPs

(non-localized spectroscopy), (B) ex vivo CNS of an EAE mouse with administered ^{19}F -loaded NPs prior to perfusion (PRESS), and (C) in vivo mouse with active EAE and administered ^{19}F -loaded NPs (PRESS). Measurements were performed using a $^1\text{H}/^{19}\text{F}$ volume resonator. Selected TR = 10000 ms

FIGURE S2 Ex vivo phantom (score=2.0) in axial orientation for increasing scan times (15 minutes, 1 hour, 3 hours and 6 hours). Reference images (A) acquired with the $^1\text{H}/^{19}\text{F}$ volume resonator show less ^{19}F signal in the brain compared to ^{19}F -CRP images (B). The steep gradient in B_1 field of the ^{19}F -CRP prevents from detecting the prominent lymph node signals in contrast to the volume resonator. SNR maps for the CRP images are presented in (C). B_1 -corrected images show concentration values closer to the reference obtained with the volume resonator (D). Uncertainty maps (E) reveal the reliability of the B_1 -corrected concentration maps, with most pixels indicating green (uncertainty $\leq 10\%$) and orange ($10\% < \text{uncertainty} \leq 25\%$) values

FIGURE S3 In vivo EAE mouse 1 (score = 2.5) in axial orientation. Concentration maps of original images (A) show an initial overestimation of the ^{19}F concentration in regions close to the RF probe surface (e.g. meninges) which partly correspond with regions with high SNR (B). After performing the *model-based B_1 correction* (C), ^{19}F concentration maps are computed. Their reliability is presented by the uncertainty maps (D) which show green (uncertainty $\leq 10\%$) and orange ($10\% < \text{uncertainty} \leq 25\%$) values for most pixels

FIGURE S4 In vivo EAE mouse 2 (score = 1.5) in axial orientation. (A) Concentration maps of original images present signals in the meninges as well as in deeper regions of the brain, indicating increased inflammatory cell accumulation. (B) SNR maps show high SNR at pixels at the top of the mouse head and a reduced SNR in regions distant to the RF probe. After applying the *model-based B_1 correction* (C), concentration maps show an expected reduction in ^{19}F concentration in the meninges and an increase in pixels far from the CRP surface. Corresponding uncertainty maps (D) demonstrate the reliability of the B_1 -corrected concentration maps, with most pixels indicating green (uncertainty $\leq 10\%$) and orange ($10\% < \text{uncertainty} \leq 25\%$) values

How to cite this article: Ramos Delgado P, Kuehne A, Aravina M, et al. B_1 inhomogeneity correction of RARE MRI at low SNR: Quantitative in vivo ^{19}F MRI of mouse neuroinflammation with a cryogenically-cooled transceive surface radiofrequency probe. *Magn Reson Med*. 2021;00: 1–19. doi:10.1002/mrm.29094

Journal Data Filtered By: **Selected JCR Year: 2018** Selected Editions: SCIE,SSCI
 Selected Categories: **"MEDICINE, RESEARCH and EXPERIMENTAL"**
 Selected Category Scheme: WoS
Gesamtanzahl: 136 Journale

Rank	Full Journal Title	Total Cites	Journal Impact Factor	Eigenfactor Score
1	NATURE MEDICINE	79,243	30.641	0.162840
2	Science Translational Medicine	30,485	17.161	0.121980
3	JOURNAL OF CLINICAL INVESTIGATION	108,879	12.282	0.139970
4	TRENDS IN MOLECULAR MEDICINE	9,946	11.028	0.018900
5	JOURNAL OF EXPERIMENTAL MEDICINE	63,983	10.892	0.071790
6	EMBO Molecular Medicine	7,507	10.624	0.025980
7	Annual Review of Medicine	6,068	10.091	0.009030
8	MOLECULAR THERAPY	16,991	8.402	0.030050
9	MOLECULAR ASPECTS OF MEDICINE	5,568	8.313	0.009020
10	Theranostics	8,769	8.063	0.020270
11	EBioMedicine	5,401	6.680	0.022310
12	ALTEX-Alternatives to Animal Experimentation	1,361	6.183	0.001920
13	Wiley Interdisciplinary Reviews-Nanomedicine and Nanobiotechnology	2,345	6.140	0.004130
14	JCI Insight	4,351	6.014	0.020440
15	Molecular Therapy-Nucleic Acids	3,189	5.919	0.010410
16	Molecular Therapy-Oncolytics	486	5.710	0.001990
17	Nanomedicine-Nanotechnology Biology and Medicine	10,131	5.570	0.014480
18	Cold Spring Harbor Perspectives in Medicine	6,223	5.564	0.016730
19	CLINICAL SCIENCE	10,951	5.237	0.014190
20	JOURNAL OF BIOMEDICAL SCIENCE	4,083	5.203	0.006300

Millward JM, **Ramos Delgado P**, Smorodchenko A, Boehmert L, Periquito J, Reimann HM, Prinz C, Els A, Scheel M, Bellmann-Strobl J, Waiczies H, Wuerfel J, Infante-Duarte C, Chien C, Kuchling J, Pohlmann A, Zipp F, Paul F, Niendorf T, Waiczies S. *Transient Enlargement Of Brain Ventricles During Relapsing-Remitting Multiple Sclerosis And Experimental Autoimmune Encephalomyelitis*. JCI Insight, 2020; 5(21):e140040.

<https://doi.org/10.1172/jci.insight.140040>

Curriculum Vitae

My curriculum vitae does not appear in the electronic version of my work for reasons of data protection.

List of publications

Peer-reviewed publications

1. **Ramos Delgado P**, Kuehne A, Aravina M, Millward JM, Vazquez A, Starke L, Waiczies H, Pohlmann A, Niendorf T, Waiczies S. *B₁ Inhomogeneity Correction of RARE MRI at Low SNR: Quantitative In Vivo ¹⁹F-MRI of Mouse Neuroinflammation with a Cryogenically-cooled Transceive Surface Radiofrequency Probe*. *Magnetic Resonance in Medicine*, 2021; 87(4):1952-1970. DOI: 10.1002/mrm.29094. Impact factor: 3.858
2. **Ramos Delgado P**, Kuehne A, Periquito J, Millward JM, Pohlmann A, Waiczies S, Niendorf T. *B₁ Inhomogeneity Correction of RARE MRI with Transceive Surface Radiofrequency Probes*. *Magnetic Resonance in Medicine*, 2020; 84(5):2684-2701. Impact factor: 4.668
3. Millward JM, **Ramos Delgado P**, Smorodchenko A, Boehmert L, Periquito J, Reimann HM, Prinz C, Els A, Scheel M, Bellmann-Strobl J, Waiczies H, Wuerfel J, Infante-Duarte C, Chien C, Kuchling J, Pohlmann A, Zipp F, Paul F, Niendorf T, Waiczies S. *Transient Enlargement Of Brain Ventricles During Relapsing-Remitting Multiple Sclerosis And Experimental Autoimmune Encephalomyelitis*. *JCI Insight*, 2020; 5(21):e140040. Impact factor: 6.014
4. Prinz C, **Ramos Delgado P**, Eigentler TW, Starke L, Niendorf T, Waiczies S. *Toward ¹⁹F Magnetic Resonance Thermometry: Spin-Lattice and Spin-Spin Relaxation Times and Temperature Dependence of Fluorinated Drugs at 9.4T*. *Magnetic Resonance Materials in Physics, Biology and Medicine*, 2018; 32(1):51-61. Impact factor: 1.832
5. Waiczies S, Rosenberg JT, Kuehne A, Starke L, **Ramos Delgado P**, Millward JM, Prinz C, Periquito J, Pohlmann A, Waiczies H, Niendorf T. *Fluorine-19 MRI at 21.1T: Enhanced Spin-Lattice Relaxation of Perfluoro-15-crown-5-ether and Sensitivity as Demonstrated in Ex Vivo Murine Neuroinflammation*. *Magnetic Resonance Materials in Physics, Biology and Medicine*, 2018; 32(1):37-49. Impact factor: 1.832
6. Waiczies S, Millward JM, Starke L, **Ramos Delgado P**, Huelnhagen T, Prinz C, Marek D, Wecker D, Wissmann R, Koch S, Boehm-Sturm P, Waiczies H, Niendorf T, Pohlmann A. *Enhanced Fluorine-19 MRI Sensitivity using a Cryogenic Radiofrequency Probe Technical Developments and Ex Vivo Demonstration in a Mouse Model of Neuroinflammation*. *Scientific Reports*, 2017; 7(1):9808. Impact factor: 4.379
7. Prinz C, Starke L, Millward JM, Fillmer A, **Ramos Delgado P**, Waiczies H, Pohlmann A, Rothe M, Nazaré M, Paul F, Niendorf T, Waiczies S. *In Vivo Detection of Teriflunomide-derived Fluorine Signal During Neuroinflammation Using Fluorine MR Spectroscopy*. *Theranostics* 2021; 11(6):2490-2504. Impact factor: 8.579

8. Periquito JS*, Gladysz T*, Millward JM, **Ramos Delgado P**, Cantow K, Grosenick D, Hummel L, Anger A, Zhao K, Seeliger E, Pohlmann A, Waiczies S, Niendorf T. *Continuous Diffusion Spectrum Computation for Diffusion Weighted MRI of the Kidney Tubule System*. *Quantitative Imaging in Medicine and Surgery*, 2021; 11(7): 3098-3119. Impact factor: 3.226
9. Prinz C, Starke L, Prinz C, Starke L, Ramspoth TF, Kerkering J, Martos Riaño V, Paul J, Neuenschwander M, Oder A, Radetzki S, Adelhoefer S, **Ramos Delgado P**, Aravina M, Millward JM, Fillmer A, Paul F, Siffrin V, von Kries JP, Niendorf T, Nazaré M, Waiczies S. *Pentafluorosulfanyl (SF₅) as a superior ¹⁹F magnetic resonance reporter group: signal detection and biological activity of teriflunomide derivatives*. *ACS Sensors*, 2021; doi: 10.1021/acssensors.1c01024. Impact factor: 7.711

Book chapters

1. **Ramos Delgado P**, Küstermann E, Kuehne A, Niendorf T, Pohlmann A, Meier M. *Chapter 8: Hardware Considerations for Preclinical Magnetic Resonance of the Kidney*. *Preclinical MR Imaging of the Kidney – Methods and Protocols for Experiments and Analyses*. Springer, New York, 2020
2. Ku MC, Schreiber A, **Ramos Delgado P**, Kettritz R, Niendorf T, Pohlmann A, Waiczies S. *Chapter 30: Studying Renal Inflammation with Fluorine (¹⁹F) MRI: Experimental Protocol*. *Preclinical MR Imaging of the Kidney – Methods and Protocols for Experiments and Analyses*. Springer, New York, 2020
3. Millward JM, Periquito JS, **Ramos Delgado P**, Prinz C, Niendorf T, Waiczies S, Pohlmann A. *Chapter 5: Ex Vivo Rodent Phantom Protocol*. *Preclinical MR Imaging of the Kidney – Methods and Protocols for Experiments and Analyses*. Springer, New York, 2020
4. Waiczies S, Prinz C, Starke L, Millward JM, **Ramos Delgado P**, Rosenberg J, Nazaré M, Waiczies H, Pohlmann A, Niendorf T. *Chapter 17: Functional Imaging using Fluorine (¹⁹F) MR Methods: Basic Concept*. *Preclinical MR Imaging of the Kidney – Methods and Protocols for Experiments and Analyses*. Springer, New York, 2020

Peer-reviewed conference abstracts and presentations

2020:

1. **Talk: Ramos Delgado P**, Millward JM, Huelnhagen T, Reimann HM, Niendorf T, Pohlmann A, Waiczies S. *Quantitative Assessment of Gadolinium-Enhancing Lesion Burden in Experimental Neuroinflammatory Disease using T₁ mapping*. ESMRMB Online Annual Business Meeting, 2020

2. **Talk: Ramos Delgado P**, Kuehne A, Millward JM, Periquito JS, Pohlmann A, Waiczies S, Niendorf T. *Comparison of Three B_1 Correction Methods for RARE Imaging with Transceive Surface RF Coils*. ESMRMB Online Annual Business Meeting, 2020
3. **Power-pitch: Ramos Delgado P**, Prinz C, Millward JM, Waiczies H, Starke L, Periquito JS, Boehmert L, Niendorf T, Pohlmann A, Waiczies S. *First In Vivo ^{19}F -MRI Quantification of Mouse Brain Inflammation Using a Cryogenic Transceive Surface RF Probe and RARE MRI*. ESMRMB Online Annual Business Meeting, 2020
4. **Poster: Ramos Delgado P**, Prinz C, Millward JM, Waiczies H, Starke L, Periquito JS, Boehmert L, Niendorf T, Pohlmann A, Waiczies S. *Quantitative in vivo ^{19}F MRI of the Mouse Brain Inflammation Using a Cryogenic RF Surface Probe and RARE*. ISMRM Virtual Conference & Exhibition, 2020
5. **Poster: Ramos Delgado P**, Kuehne A, Millward JM, Periquito JS, Niendorf T, Waiczies S, Pohlmann A. *Comparison of Three B_1 Correction Methods for RARE Imaging with Transceive Surface RF Coils*. ISMRM Virtual Conference & Exhibition, 2020
6. **Poster: Ramos Delgado P**, Kuehne A, Millward JM, Periquito JS, Niendorf T, Waiczies S, Pohlmann A. *Implementation, Validation and Comparison of Three B_1 Correction Methods for RARE Imaging with Transceive Surface RF Coils*. 11th Annual Scientific Symposium: Ultrahigh Field Magnetic Resonance, 2020
7. **Poster: Ramos Delgado P**, Kuehne A, Millward JM, Periquito JS, Niendorf T, Waiczies S, Pohlmann A. *First In Vivo ^{19}F -MRI Quantification of Mouse Brain Inflammation Using a Cryogenic Transceive Surface RF Probe and RARE MRI*. 11th Annual Scientific Symposium: Ultrahigh Field Magnetic Resonance, 2020
8. **Short presentation:** Millward JM, **Ramos Delgado P**, Prinz C, Els A, Bellman-Strobl J, Waiczies H, Paul F, Niendorf T, Waiczies S. *Transient Enlargement of Brain Ventricles in Experimental Autoimmune Encephalomyelitis Meaningful to Multiple Sclerosis Pathology*. ESMRMB Online Annual Business Meeting, 2020
9. **Poster:** Prinz C, Sherazi F, Starke L, **Ramos Delgado P**, Kuehne A, Niendorf T, Waiczies S. *Fluorine-19 MR Characterization of Siponimod as a MR Theranostic Approach in MS Treatment*. ISMRM Virtual Conference & Exhibition, 2020
10. **Power-pitch:** Prinz C, Sherazi F, Starke L, **Ramos Delgado P**, Kuehne A, Niendorf T, Waiczies S. *Fluorine-19 MR Characterization of Siponimod as a MR Theranostic Approach in MS Treatment*. ESMRMB Online Annual Business Meeting, 2020
11. **Poster:** Sherazi F, Starke L, Prinz C, Millward JM, **Ramos Delgado P**, Aravina M, Niendorf T, Waiczies S. *Towards Non-invasive Imaging of MS*

Disease-modifying Drugs. 11th Annual Scientific Symposium: Ultrahigh Field Magnetic Resonance, 2020

12. **Poster:** Skenderi S, Millward JM, Starke L, **Ramos Delgado P**, Sherazi F, Prinz C, Periquito JS, Niendorf T, Waiczies S. *Characterization of Fluorinated Pesticides using Fluorine (¹⁹F) MR Methods*. 11th Annual Scientific Symposium: Ultrahigh Field Magnetic Resonance, 2020

2019:

13. **Power-pitch:** **Ramos Delgado P**, Kuehne A, Starke L, Millward JM, Periquito J, Niendorf T, Waiczies S, Pohlmann A. *Inhomogeneity Correction for the Transmission Field (B_1^+) and Sensitivity Profile (B_1^-) of Transceive Surface Radiofrequency Coils: a Retrospective Empirical Solution for RARE*. Ultrahigh Field Symposium, 2019
14. **Poster:** **Ramos Delgado P**, Kuehne A, Starke L, Millward JM, Periquito J, Niendorf T, Waiczies S, Pohlmann A. *Retrospective Transmission Field (B_1^+) and Sensitivity Profile (B_1^-) Correction for Transceive Surface RF Coils: an Empirical Solution for RARE*. ISMRM 27th Annual Meeting & Exhibition, 2019
15. **Poster:** Millward JM, Boehmert L, **Ramos Delgado P**, Reimann HM, Periquito JS, Els A, Smorodchenko A, Scheel M, Belmann-Strobl J, Infante-Duarte C, Paul F, Niendorf T, Pohlmann A, Waiczies S. *Transient Enlargement of Brain Ventricles during Multiple Sclerosis and Experimental Autoimmune Encephalomyelitis*. ISMRM 27th Annual Meeting & Exhibition, 2019
16. **Power-pitch:** Waiczies S, Rosenberg JT, **Ramos Delgado P**, Starke L, Periquito JS, Prinz C, Millward JM, Kuehne A, Waiczies H, Pohlmann A, Niendorf T. *Fluorine-19 MR at 21.1 Tesla for Enhanced Detection of Brain Inflammation*. ISMRM 27th Annual Meeting & Exhibition, 2019
17. **Poster:** Boehmert L, Waiczies H, Wenz D, Oezerdem C, Kuehne A, **Ramos Delgado P**, Seeliger E, Pohlmann A, Niendorf T. *Whole Body Sodium Quadrature Birdcage RF Coil for ²³Na MRI of Small Rodents at 9.4T and Its Application in Sodium Imaging of the Eye and Kidneys*. ISMRM 27th Annual Meeting & Exhibition, 2019
18. **Poster:** Prinz C, **Ramos Delgado P**, Eigentler T, Starke L, Niendorf T, Waiczies S. *Fluorine-19 Magnetic Resonance Thermometry: Temperature Dependence of Spin-Lattice and Spin-Spin Relaxation Times of Fluorinated Drugs at 9.4 T*. ISMRM 27th Annual Meeting & Exhibition, 2019
19. **Poster:** Prinz C, Millward JM, **Ramos Delgado P**, Starke L, Pohlmann A, Niendorf T, Waiczies S. *Investigating the Biodistribution of the Antiinflammatory Drug Teriflunomide In Vivo Using ¹⁹F MRI*. ISMRM 27th Annual Meeting & Exhibition, 2019

2018:

20. **Poster: Ramos Delgado P**, Millward JM, Prinz C, Starke L, Münchberg S, Pohlmann A, Niendorf T, Waiczies S. *¹⁹F Signal Distribution in Pre-Symptomatic Experimental Autoimmune Encephalomyelitis*. Joint Annual Meeting ISMRM-ESMRMB, 2018
21. **Poster:** Prinz C, Millward JM, Periquito J, Starke L, **Ramos Delgado P**, Muenchberg S, Pohlmann A, Niendorf T, Waiczies S. *¹⁹F MR Characterization of Teriflunomide, a Fluorinated Drug Indicated in Multiple Sclerosis*. Joint Annual Meeting ISMRM-ESMRMB, 2018

2017:

22. **Poster, presenting author:** Waiczies S, **Ramos Delgado P**, Millward JM, Starke L, Huelnhagen T, Prinz C, Marek D, Wecker D, Wissmann R, Koch SP, Boehm-Sturm P, Waiczies H, Niendorf T, Pohlmann A. *A Novel Fluorine-19 Cryogenic Radiofrequency Probe Shows Enhanced MRI Sensitivity in Neuroinflammation*. Ultrahigh Field Symposium, 2017
23. **Poster: Ramos Delgado P**, Waiczies S, Niendorf T, Pohlmann A. *Towards the quantification of local ¹⁹F marker concentration in small rodents*. PhD Retreat, 2017
24. **Poster: Ramos Delgado P**, Millward JM, Prinz C, Starke L, Münchberg S, Pohlmann A, Niendorf T, Waiczies S. *¹⁹F Signal Distribution in an EAE Mouse Model*. Red Hot MRI Symposium, 2017
25. **Poster, presenting author:** Pohlmann A, Millward JM, **Ramos Delgado P**, Marek D, Wecker D, Wissmann R, Waiczies H, Niendorf T, Waiczies S. *A Novel Cryogenic Radio-frequency Probe for High Spatial Resolution Fluorine-19 MRI of the Brain Inflammation*. ISMRM 26th Annual Meeting & Exhibition, 2017

Acknowledgements

First, I would like to thank my supervisors Prof. Dr. Thoralf Niendorf, Dr. Andreas Pohlmann and Dr. Sonia Waiczies for giving me the opportunity to work at the Berlin Ultrahigh Field Facility (B.U.F.F.) and for their constant guidance, support, and enthusiasm in the project.

I also want to thank each and every of my colleagues from B.U.F.F. (present and gone) for all the shared moments, the moral and technical support, and many laughs during all these years. Some people who made the difference during my PhD years (random order): Haopeng Han (our weekends at B.U.F.F. will always be legendary!), João Periquito, Henning Reimann, Eva Oberacker, Daniel Wenz, Till Huelnhagen, Kathleen Cantow, Jurjen Heij, Salina Skenderi, Jason Millward. You will be missed, guys!

Many thanks to my collaborators from MRI.TOOLS GmbH (André Kühne, Alonso Vázquez and Helmar Waiczies) for the helpful discussions and fruitful collaboration. Special mention to André, who has supported my work until the very end and offered an ear, a hand, and advice any time I needed. Thank you, it really meant a lot.

I also thank Bruker BioSpin for collaborating with us and building our fantastic cryoprobes, without which this thesis would not exist. In particular, I would like to thank Stefan Klahs for the (thousands of) times I had to call him during this arduous PhD to fix the MR electronics and the cryoprobes—which are very cool, but also prone to breaking and other disasters. He always got my back and went the extra mile to help me (even on the weekends!).

Finalmente, me gustaría dar las gracias a mi familia y amigos: Pilar Delgado, José Manuel Ramos, Javier Gómez, Nastia Roniak, Iryna Yosyk, Shiva Mohammadzadeh, Valentin Prevost, Anneke Meyer, Joana Pinto e Isabel Martínez por su apoyo moral constante, por sus consejos, sus charlas inspiradoras, por obligarme a descansar y recordarme la hora de comer, por comprender que tenía que darlo todo por este PhD (aunque eso significara que estos años no estuve todo lo presente que debería haber estado, ¡lo siento!) y, sobre todo, por no dejarme abandonar jamás. Tengo claro que no estaría hoy aquí sin vosotros.

Y, sobre todo, quiero agradecer y dedicar esta tesis a mis abuelos Ángel y Fructuosa. Esto es por vosotros, allá al otro lado del arcoíris. Ingeniosa, ingeniera y ahora también DOCTORA, abuelillo.

Now, Dobby is free.